POLITECNICO DI TORINO

Corso di Laurea Magistrale in Ingegneria Aerospaziale

Tesi di Laurea Magistrale

Study of post-process treatments applied on the Inconel 939 superalloy produced by laser powder bed fusion.

Relatori
Dott. Giulio Marchese
Prof.ssa Sara Biamino

Candidato
Martina Pippa

A Mamma, Papà e Ivano,
a voi ogni mio traguardo.

Chapter 1

Introduction

This thesis deals with the study of the Ni-based superalloys Inconel 939 (IN939) processed by Laser Powder Bed Fusion (LPBF). This is an Additive Manufacturing (AM) process which allows to obtain the final components by a layer-by-layer process, using a 3D model. This allows the possibility to obtain components with complex geometry in a single process, reducing costs, time, and obtain parts with a lower weight than traditional technologies.
IN939 is a Ni-based superalloys particularly suitable for applications at high temperatures and it can be a good candidate for aeronautical turbine blades. IN939 has excellent mechanical characteristics and resistance to corrosion and oxidation at high temperatures.
At the beginning, various combinations of process parameters like laser power, scanning speed, hatching distance were employed. The percent of defects were evaluated for the different conditions to determine the best set of process parameters. For all the conditions, the material showed cracks formation mainly along the grain boundaries.
Starting from a condition with low presence of defects, it was performed a Hot isostatic pressing (HIP) in order to close the cracks and porosity. It seems that HIP is effective in close the cracks and reduce the porosity under 0.1 %. Afterward, it was studied the microstructure and hardness of the samples subjected to solutioning and different ageing steps.
The solutioning was carried out at a temperature of 1160 °C for 4 hours. After that the carbides are solubilized in the gamma prime matrix.
The last treatments were two ageing, the first at 1000 °C for 6h and the second at 800 °C for 4h, followed by the hardened of the material thanks to the precipitation of the gamma prime phase.
Finally, the hardness test was performed on the samples at the end of each heat treatment. The hardness has an increasing trend starting from the value of 263.2 HB for the as-built condition, up to 376 HB at the end of the second ageing. It was also observed that the sample following the HIP was harder than the specimen following the solutioning and the first ageing treatments. This is due to the carbides precipitated on the grain boundary because of HIP, which, having large dimensions, make the material harder but certainly more fragile.

The structure of the thesis is therefore divided into five chapters:

- The first explains the state of the art of active manufacturing processes and superalloys, with particular attention to Inconel 939 produced through LPBF.
- The second describes the materials and methods used during the experimental work.
- The third and fourth summarizes and discusses the results obtained during the experimental phase.
- The fifth discusses the conclusions of the experimental work and possible future developments

Contents

List of Figures

List of Tables

Chapter 2

State of art

2.1 Additive manufacturing

The American Society for Testing and Materials International (ASTM) has defined additive manufacturing (AM) as “a process of joining materials to make objects from 3D model data, usually layer upon layer, as opposed to subtractive manufacturing methodologies. [. . .]” [1].
The idea of making three-dimensional pieces of any geometry by applying metal powder on a substrate and solidifying it thanks to an energy beam dates back to 1971 with Pierre Ciraud and, again, six years later with the inventor Ross Housholder who thought of a process of computer-controlled production, where the melted particles form the object layer by layer, a very innovative idea, but impossible to commercialize for the technologies of the time. The drawing of the projects are shown in Fig. 2.1
We have to get to 1987 when Michael Feygin patented and commercialized a technique for manufacturing laminated molds, dies and prototypes. ”The new technique is based powder metallurgy and also uses a scanning laser. One layer (0.002 inch to 0.020 inch) of the powdered metal is spread on a base and partially glued by sliding a heated roller on controlled pressure powder. The layer is then scanned by the laser in the model section of the desired cross section. This completes the sintering of the metal ”and, in the same years, Westinghouse Electric Corp., led by Frank Arcella, who in 1997 opened the company Aeromet, printed in the printing of titanium structures. [2]
But, precisely in those years, another company made its way, EOS, which in 1997 acquired the worldwide patent rights for the introduction of laser sintering technology and, to date, is a global leader in industrial 3D printing of metals and plastics [3]

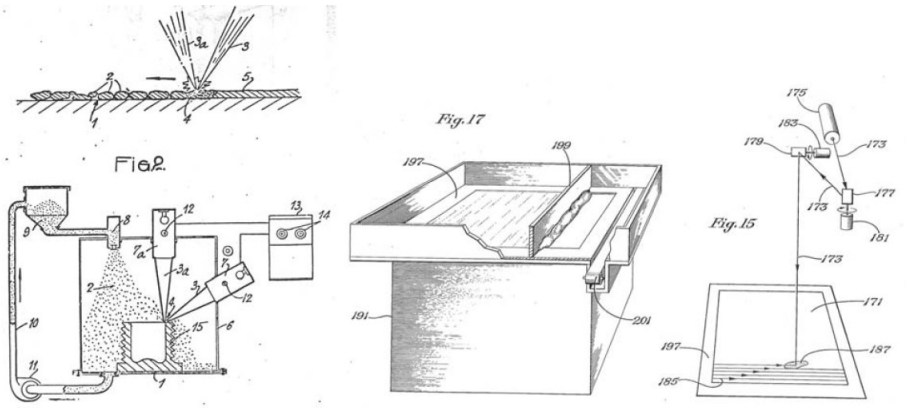

Figure 2.1: Inventions of Ciraud (left) and Housholder (right). [2]

2.1.1 Advantages of AM

The main advantages of Additive Manufacturing is, as is reported in Ref.[4, 5]:

- Print complex components with geometries that are not possibile or very complicated to produce with conventional casting and machining techniques. It is estimatedthat currently, about 60% of the pieces are modified in production. For these reasons, it is easy to understand the advantages of AM in terms of cost and time [4].
- Design and fabricate the same components with less weight.
- To improve the prevedibility and reliability of the products. The AM allows you to decide in advance how the characteristics of the component evolve over time and how it responds to a different temperature of use.
- Reduce the number of components: AM has very high free form fabrication, reducing the number of different parts to create a singular component.
- To eliminate the necessity to create ad hoc machinary for the realization of components.
- To reduce the cost and time for the transport, favoring the "home-production". The consumer is fast transforming into a producer-consumer[6].

This last point can be widely useful for printing components in remote places, thanks to simple data exchanges between the manufacturing company and the customer, avoiding stockage and transport.
From the current description, the main benefits of Additive Manufacturing can be summarized into five words: Cost, speed, quality, innovation, and impact, as shown in Figure 2.2.

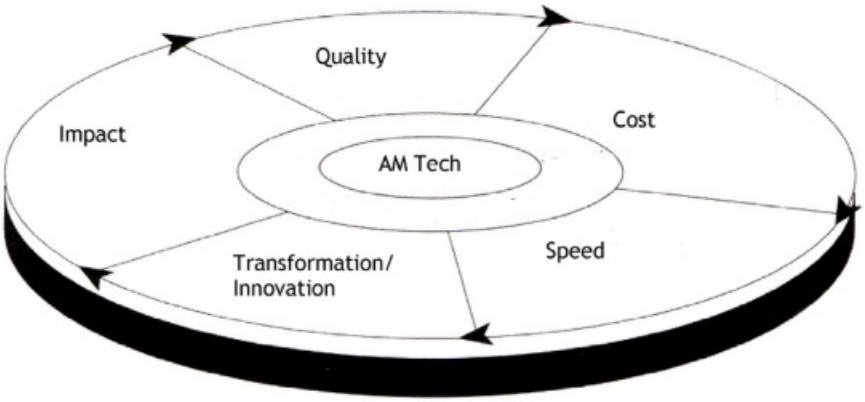

Figure 2.2: Benefits of AM technologies over traditional manufacturing [4].

However the Additive Manufacturing has some challenges that are not yet resolved [5]:

- Slower production time for components with simple shapes.
- Optimization of the process parameters to avoid too high residual stressesand delamination [7].
- A determine degree of Roughness needs post-production finishing operations.

Anyway, this technology is in continuous evolution and, year after year, it is growing and experts are gaining the proper knowledge to ensure it will be fully implemented in the industry. According to a Delphi study[8], by 2030 less critical parts will be print locally with AM technology, while more critical parts will be made with tradidional production and the possibility to print parts in multi-materials will be exploited more and more [9]. Multi-materials are solid components made up of several types of materials organized in a random or well-defined order. These structures have many applications in aeronautical, automobile and medical industries fields [10]. At that point, traditional production will be totally transformed: AM technology allows the customization of products by directly involving the customer in the design phase. With the implementation of high efficiency and high-fidelity simulation algorithms, it will be enough to specify the performance of the project to generate multimaterial objects. Thanks to AM, decentralized production will be favored, bringing important changes within the supply chain [9].
Another positive step for AM is certainly the development of multi-laser machines and the ever higher achievable laser power, that allow to increase production speed up to 10 times compared to machines with a single laser. This certainly translates into a lower cost both in the production of a single piece and in the production of several pieces simultaneously [11]. This will allow an increasingly efficient, fast and economical production, as is show in Fig.2.3 [4].

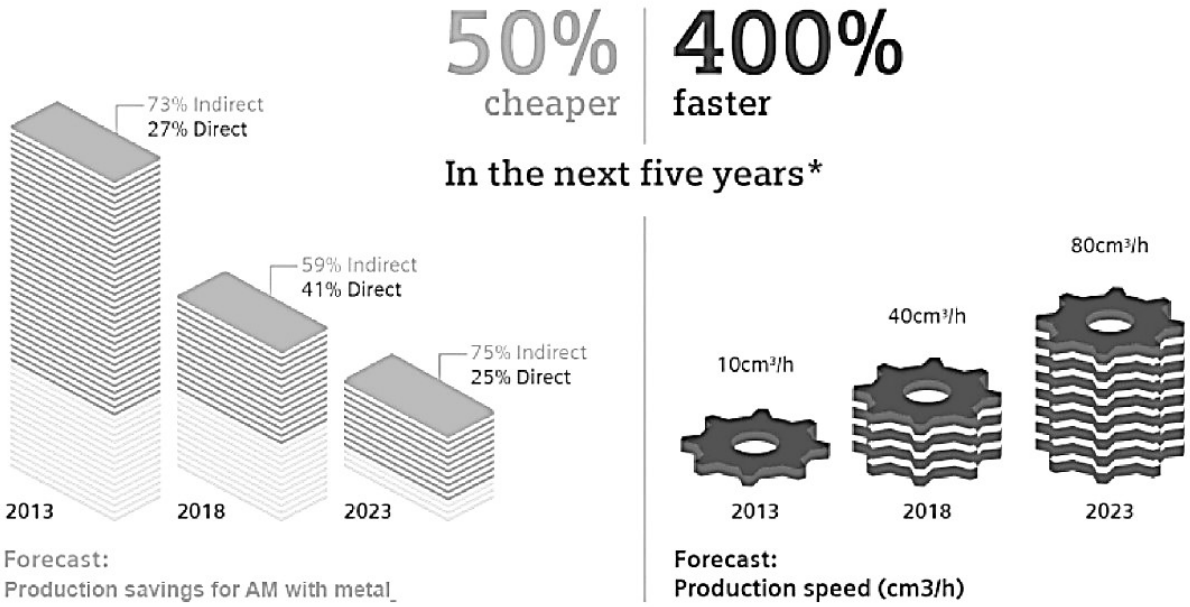

Figure 2.3: Cost and speed evolution in AM [4].

2.1.2 Additive Manufacturing in Aerospace

In terms of cost and time savings, the tangible advantages of Additive Manufacturing, in term of cost and time savings, immediately attracted various fields of industry, including aerospace, which represents 18.2% of AM revenues[12].

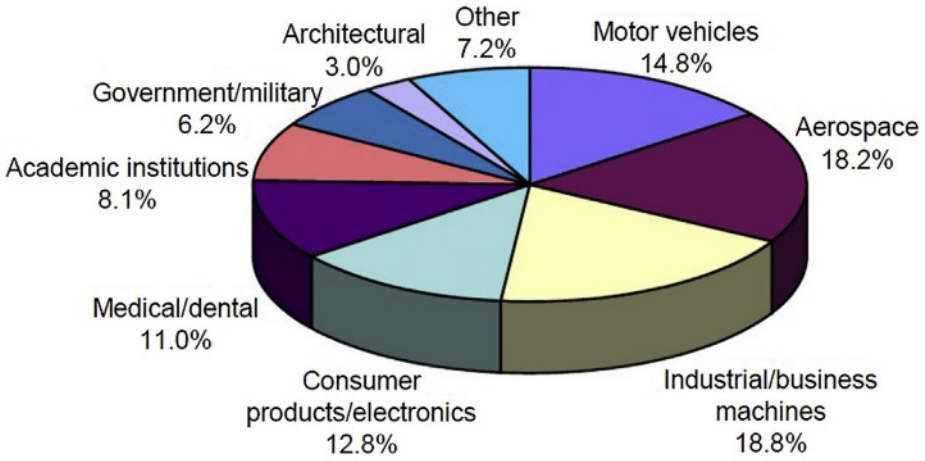

Figure 2.4: Additive Manufacturing market share by industry [12].

The possibility that Additive Manufacturing processes offer to print parts of almost any form, also reducing the weight of the part by redesign, has immediately attracted the attention of aerospace designers, which scope is to obtain light products with a hight strength-to-weight ratio. This has allowed better efficiency, a reduction of emissions, and greater reliability of the components.
For instance, 1 Kg of any material has an impact on the cost equal to 10.000 for a space launch and 1300 in fuel per year for a plane, so reducing weight reduces the overall cost of missi [4].
For example, GE Aviation has reduced 855 parts into a dozen using AM technologies, improved fuel efficiency up to 20%, and achieved 10% more power. More specifically, GE has redesigned bearing support and sump (part of the oil lubrification system) to consolidate 80 parts into one and 20-part nozzle into a single AM unit [12].
Another study on the aerospace industrypointed outthattheAMtechnologies allow reducing the lead-time by up to 30 - 70%, costs up to 45%, and production costs around 30 – 35% [13].
The main benefits that AM offers to Aerospace industry are listed into Table 2.1.

Table 2.1: Aerospace industries benefiting from additive manufacturing [4]

Applications	Benefits Gained
Prototyping Component manufacturing Reducing aircraft weight Engine components for the Airbus Flight-certified hardware	Produce very complex work pieces at low cost Allow product lifecycle leverage Objects manufactured in remote locations, as delivery of goods is no longer a restriction A reduction in lead-time would imply a reduction in inventory and a reduction in costs Manufacturing of satellite components On-demand manufacturing for astronauts Eliminate excess parts that cause greater aerodynamic drag Improve quality The performance of the materials can be equal or superior to the materials processed with traditional technologies

The starting material, such as powder with specific characteristics, can drastically increase the cost of the components. Additionally, the process parameter optimization and the study to minimize the residual stresses must be taken into account. Finally, producing large volumes with 3D printing can be very expensive, especially for processes that require an inert atmosphere [12]. This last limitation is especially evident for the powder bed fusion (PBF) additive manufacturing where the components are built into a chamber, and therefore, the

maximum dimensions are limited by the chamber.

Additive Manufacturing apllications in Aerospace are various, and some of these are showed into Table 2.2.

Table 2.2: Metal and nonmetal additive manufacturing technologies with select aerospace examples [12].

	AM technology	Aerospace examples
Metal	Direct Energy Deposition (DED)	Helicopter engine combustion chamber fabrication (DED)
	Powder Bed Fusion (PBF)	Blisk airfoil repair (DED)
	Cold Spray	Satellite antenna bracket (PBF)
	Binder jetting	Lap joint reinforcement (SPD)
Non Metal	StereoLithography Apparatus (SLA)	UAV wing design (PolyJet)
	Selective Laser Sintering (SLS)	Ratchet wrench printed by NASA on ISS (SLS)
	PolyJet	UAV wing design (polyJet)
	Fused Deposition Modelling (FDM)	Boeing 777-300ER door handle (FDM)
		Camera case prototyping (FDM)

The aerospace industry takes advantage of Additive Manufacturing techonologies 360-degree, for both metal and non-metal parts, but mostly to achieve complex metallic parts.
For example, The Welding Institute has built a combustion chamber of a helicopter in IN718 using a 5-axis LMD (fig 2.5),or Boeing which saved up to $ 3 million by printing parts for the 787 in Titanium with AM technology [12].

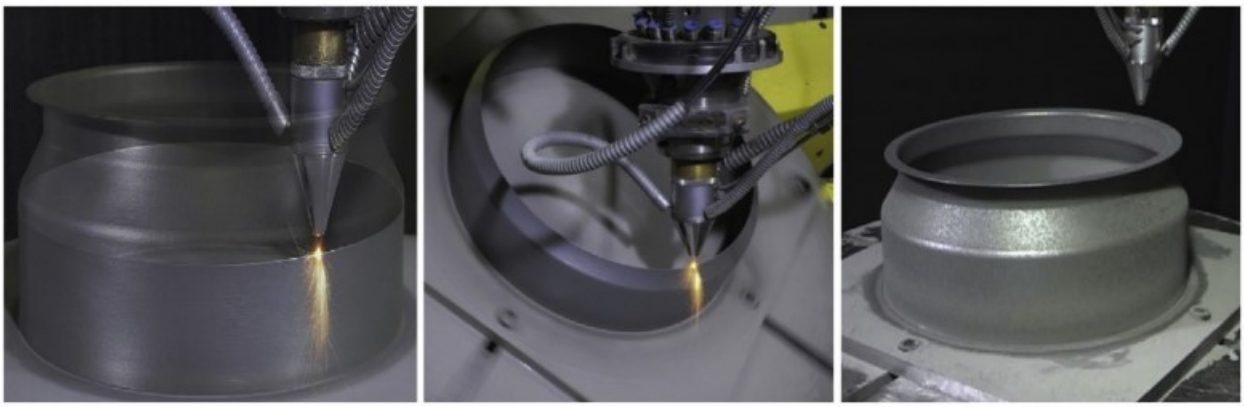

Figure 2.5: Printed helicopter engine combustion chamber [12].

In addition, AM allows to build quickly polymer prototypes for preliminary tests in wind tunnel, a economic way to to validate physical characteristics and computational fluid dynamics models. An example is Airbus which used this method by manufacturing a 90% polyamide powder prototype, thus saving time and being able to build a plane in just 8 weeks.
Another use of AM is for the repair damaged components. Repair with additive processes has been shown to be economically advantageous compared to traditional processes. Two categories of repair can be highlighted: restoration of geometry and restoration of structural integrity. The first aims to reconstruct missing parts due to wear, an example of which shown in fig.2.6 where the T700 disk was repaired through DED processes.

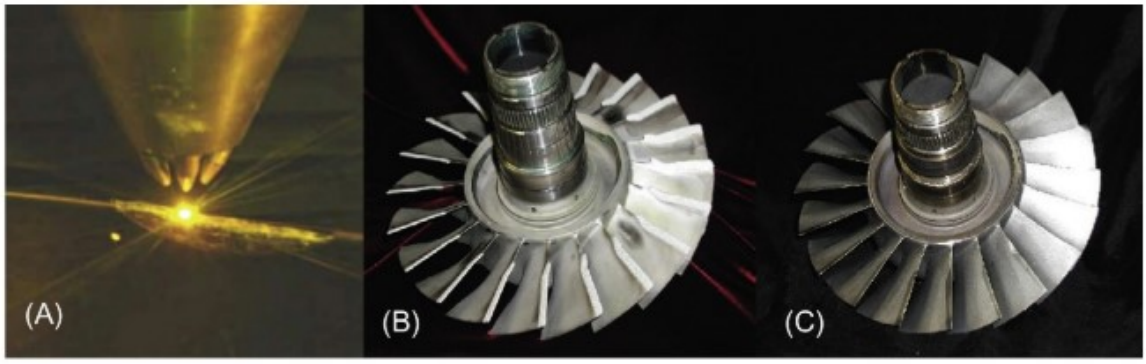

Figure 2.6: T700 blisk repair by DED.(A)In process repair,(B)Blisk after deposition,(C)Blisk after finishing. Suorce: Optomec [12].

2.2 Metal Additive Manufacturing processes

3D printing techniques for metallic materials can be divided into powder bed and powder spray technique, shown in Fig. 2.7
In Powder Bed Fusion techniques, the energy source selectively fuses the powder bed regions. This method allows to obtain high density parts, while in DED technologies the energy is focused to melt the material by melting while they are deposited, this technique is used little for the production of whole parts rather it is widely used in the field of repairs [14].

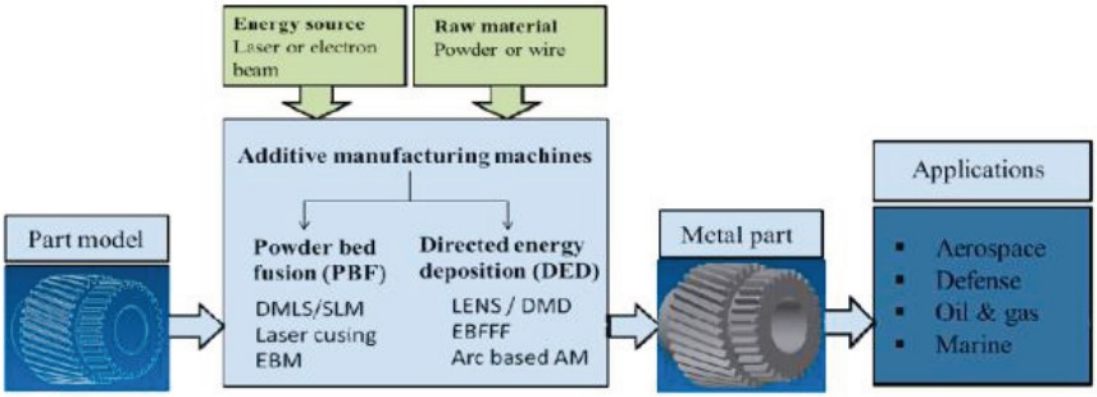

Figure 2.7: Common metal additive manufacturing process [14].

2.2.1 Direct Energy Deposition

The Directed Energy Deposition (DED)is a powder spray technique. This process sees a concentrated energy source that intersects at one point with the raw material. The DED process technique is shown in Fig.2.8. As can be seen in Figure, DED systems see a concentrated energy source (usually a laser beam) and raw material flow intersecting at a focal point. The powder is sent through a flow of protective inert gas, which will also serve to protect the melt pool created by the energy density that melts the material where it touches and around it. The DED process can be divided according to the type of energy it uses (Laser-Based, Electron Beam Based, Plasma or Electric arc based) or according to the material (Powder-based, Wire based). Although wire-based DED processes allow for larger structures, they present a lower resolution than powder-based ones, therefore the most commonly used DED technique is powder-based that uses a laser as an energy source [15, 16].

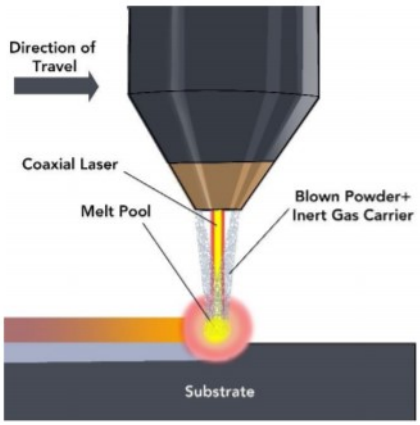

Figure 2.8: Example of DED process [17].The energy melts the material where it is directed and forms a fusion pool [16].

Although wire-based DED processes allow for larger structures, they present a lower resolution than powder-based ones, therefore the most commonly used DED technique is powder-based that uses a laser as an energy source. However, parts produced through DED may have some defects. Firstly, interlayer porosity can occur, caused by insufficient energy that fails to completely melt the material, or intralayer, due to the inert gas that remains trapped in the material. Fig.2.9 shows the two types of porosity, the first sees large and irregular pores, the second instead sees scattered spherical pores. The literature introduces the global energy density (GED) parameter, expressed as:

$$GED = \frac{P}{vd} \tag{2.1}$$

Where: P = laser power [W], v is the scan speed [mm/s], d is the laser spot size [mm] The GED is a parameter that enable to establish a relationship with porosity, as a set of the two porosities described above, this trend is shown in Fig. 2.10 Another phenomenon that can occur during the DED process is the vaporization of some alloying elements. This is due to the different boiling points of the individual elements and therefore causes the loss of binding elements, which can lead to anomalies in the expected mechanical characteristics [16].
The advantages of the DED process lie in the high construction speed, the possibility of obtaining high densities and resistances, the possibility of making parts in multimaterial, and the possibility of building large pieces not limited to the dimensions of the chamber like LPBF process. However, the process is expensive, and the construction resolution is inferior to the LPBF process [15]. In recent years, attention has turned to the repair of parts using the DED process, thanks to its characteristics (precision, tight fusion and heat-affected zones) that allow low distortions of the part. Fig.2.11 shows a titanium blisk repaired by DED [18].

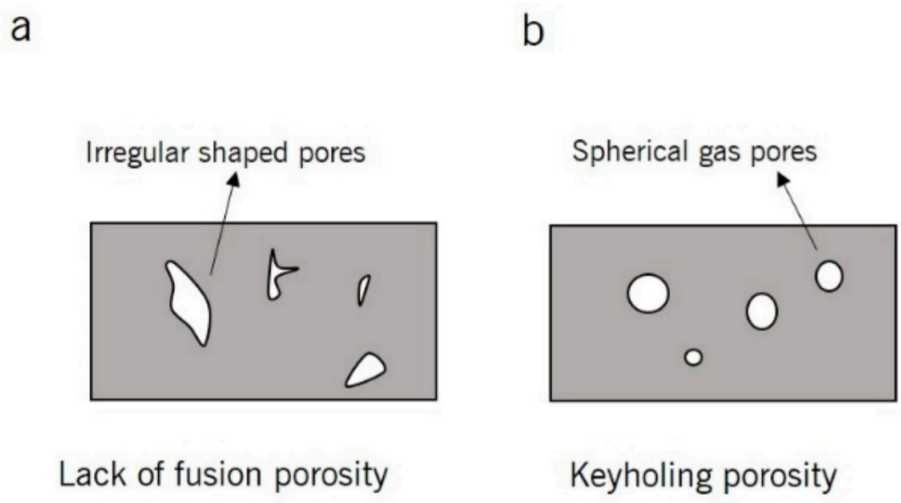

Figure 2.9: Two type of porosity in DED process. a)interlayer porosity, b) intralayer porosity [16].

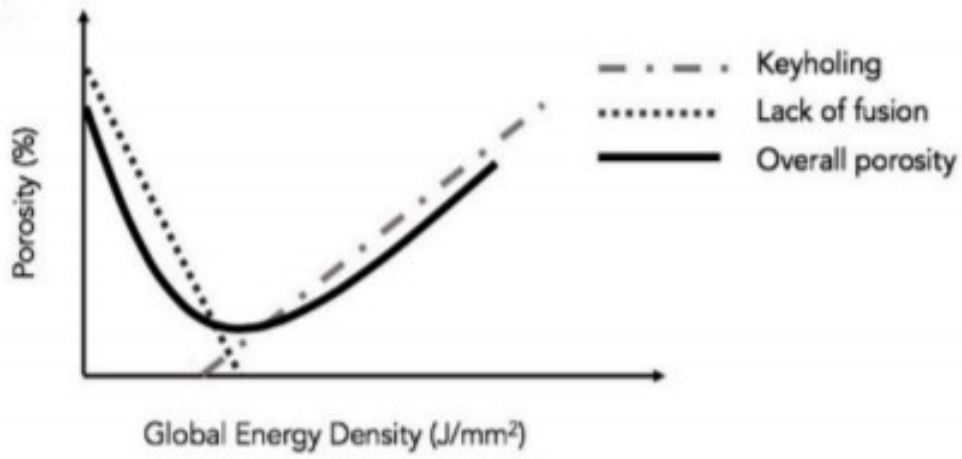

Figure 2.10: Trend GED- porosity [16].

Figure 2.11: Titanium Blisk repaired by DED. The repair allowed to obtain a dense part with a fine miscrostructure. The component, under high-cycle fatigue testing, demonstrated a higher strength than that of the reference material [18].

2.2.2 Powder Bed Fusion

In the Powder Bed Fusion (PBF) processes, the powder is melted by an energy source in specific points. Once the first layer is melted, the powder is deposited on the previous layer, and the process is repeated until the complete piece is obtained. For metal alloys, the typical layer thickness is 20–60 μm. The chamber is protected by a protective gas like argon (LPBF process) or under vacuum (EBM process).
A schematic illustration of the process is reported in Fig. 2.12. Depending on the type of energy source, the properties of the pieces, such as relative density, mechanical properties, and residual stress, can be influenced. For these reasons, it is essential to optimize the printing parameters and also the thermal post-processing [19, 20].

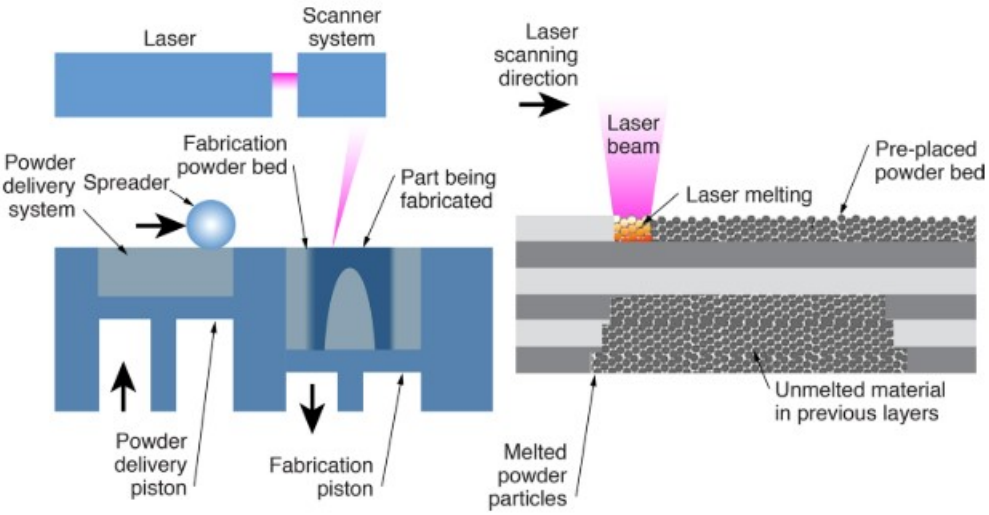

Figure 2.12: PBF technology. On the left the powder delivery system and on the right the energy delivery system. Laser in the case of LPBF and electron beam in the case of EBM machine.

PBF process can be divided into two categories, depending on the energy sources: Laser powder bed fusion (LPBF), and Electron Beam Melting (EBM).
The EBM uses an electron beam to melt the metal powder, and the process is carried out in a high vacuum. The powder is subjected to pre-heating that can reach very high temperatures, and this reduces the residual stresses during the process [20].
EBM is used with various metals and alloys such as steels, titanium alloys and nickel based super alloys. However, all materials that have a low melting point are excluded, such as aluminum magnesium and their alloys, as low melting materials end to evaporate under vacuum conditions [21]. Some materials processed by EBM, and the corresponding properties are shown in Tab.2.3[22].
The electron beam's high energy enable the use of larger layer thicknesses from 50 to 200 μm with respect to the LPBF. However, parts obtained by EBM see greater surface roughness [20]. The main differences between LPBF and EBM are shown in table 2.4.

Table 2.3: Properties of some materials processed by EBM [22].
Note: hpc= hexagonal closest packed; fcc= face-centered cubic; bcc= body-centered cubic.

Metal	Metling T[°C]	Structure	Young's modulus[GPa]
Ti-6Al-4V	1630	hcp	110
Co-Cr	1430	fcc	210
IN 625	1330	fcc	205
IN 718	1300	fcc	205
Rene 142	1375	fcc	212

Table 2.4: Main differences between LPBF and EBM processes [23]

Features	LPBF	EBM
Heat source	Laser beam (up to 1 kW)	Electron beam (60 kW)
Scan speed	Limited by galvanometer inertia	Fast, magnetically driven
Powder size	10–45 μm	45–106 μm
Minimum beam size	50 mm	140 mm
Beam/melt pool dimension	0.5–1.5 μm	2–3 μm
Layer thickness	20–100 μm	50–200 μm
Chamber atmosphere	Argon or Nitrogen	Vacuum (+helium)
Environment temperature	Typical build platform at 100–200°C	Chamber at 400–1000 °C
Powder pre-heating	Using infrared or resistive heaters	Using electron beam
Surface finish	Excellent to moderate (20 μm)	Moderate to poor (35 μm)
Residual stresses	Yes	No

Figure 2.13: An example of EBM. The Rolls-Royce company has made, through the EBM process, a Ti-6Al-4V housing of the front bearing of the Trent XWB-97 engine. This, with a diameter of 1.5m and a thickness of 0.5m, houses 48 airfoils [24].

2.3 Laser powder bed fusion (LBPF)

This process is one of the powder bed fusion additive manufacturing (AM) processes where a laser beam melts powder. Usually, layer thickness ranging from 20 to 100 μm. There are other names to define the LPBF such as Direct Metal Laser Sintering (DMLS) and Selective laser melting (SLM). The different names are trademarker given by the different companies. In this process, the parameters to regulate and optimize are: laser power, scanning speed, hatching distance and layer thickness, schematically provided in Fig.2.14. These parameters can be combined to generate the VED (volume energy density), as reported in the following equation:

$$VED = \frac{P}{vth_d} \tag{2.2}$$

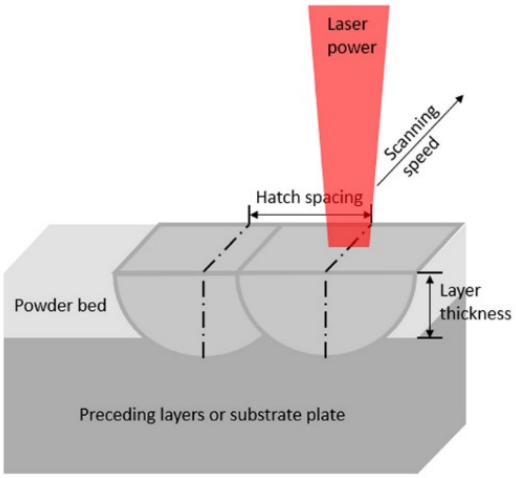

Figure 2.14: Selective laser melting process parameters [25]

These parametrers affect significantly the final product. This influence has been summarized in the following diagrams. The application of low laser power, high scanning speed and large layer thickness reduce the total energy delivered to the material, increasing the degree of balling formation (Fig.2.15). The bailling is a phenomenon in which metals form spheroidal balls, leading rough surfaces (Fig. 2.16). High laser and low scanning speed may result in extensive material evaporation and the keyhole effect (Fig. 2.17). With keyhole effect we observe protrusion at the bottom of the melt pool, the sudden increase of the melt pool cross section, as well as the qualitative change of the cross sectional shape (Fig. 2.18). Large hatch distance often results in regular porosity in built parts, as adjacent melt lines do not fuse together completely (Fig. 2.19). The subsequent increase in porosity with increasing the hatch spacing is shown in Fig. 2.20 [25].

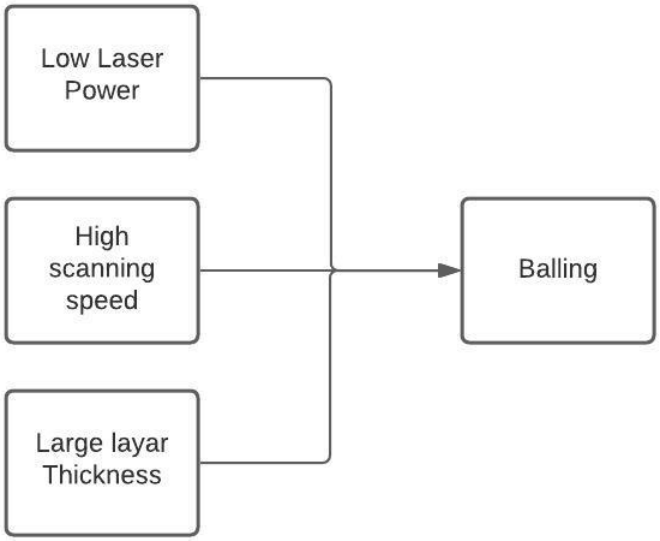

Figure 2.15: The influence of process parameters(I) [25].

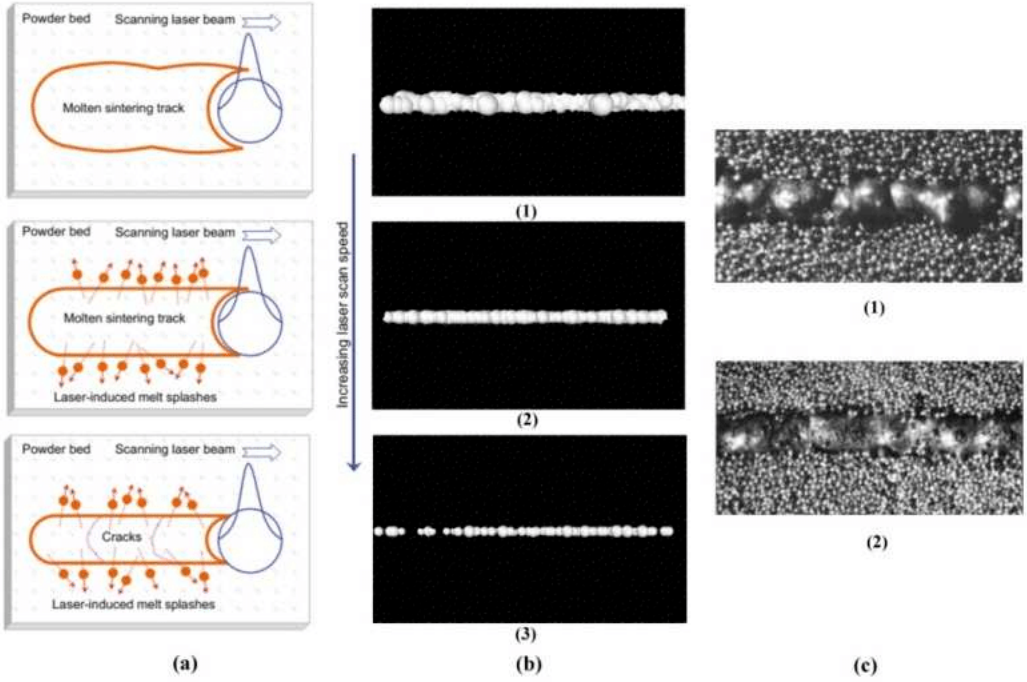

Figure 2.16: The effect of scanning speed on the balling phenomenon [26].

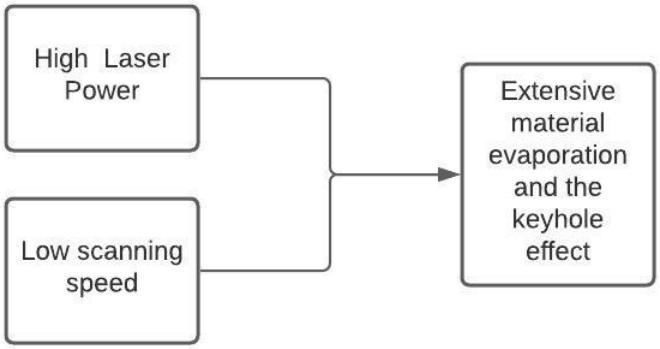

Figure 2.17: The influence of process parameters(II) [25].

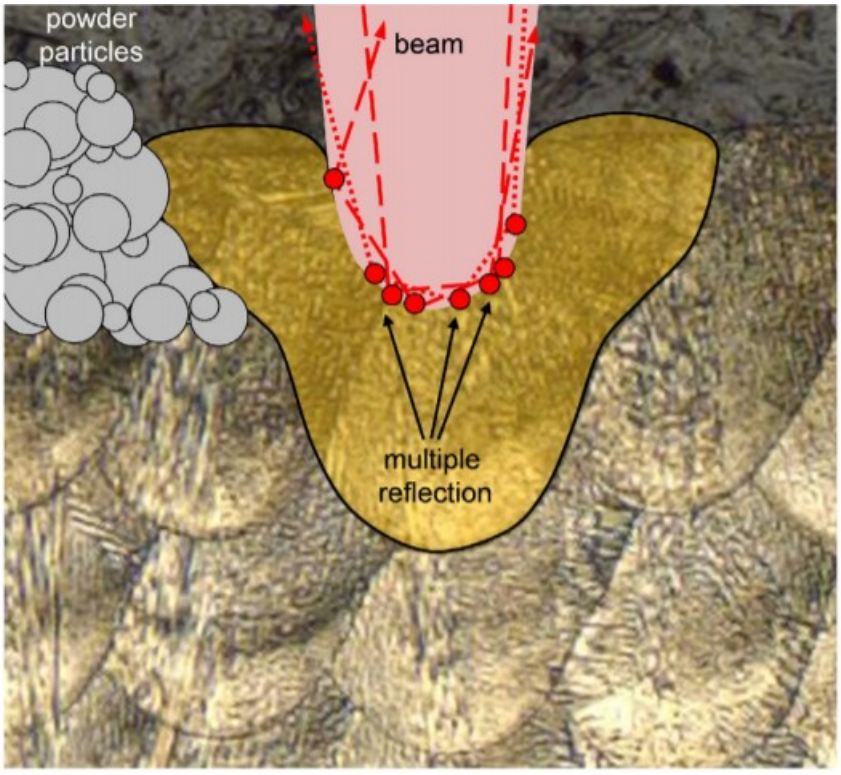

Figure 2.18: The keyhole effect [27].

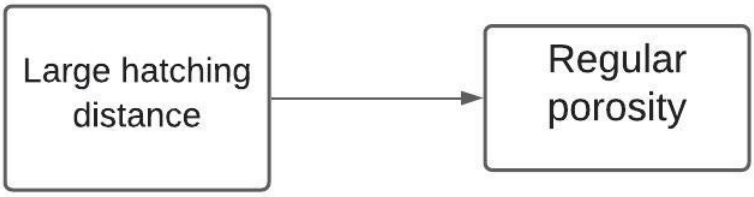

Figure 2.19: The influence of process parameters(III) [25].

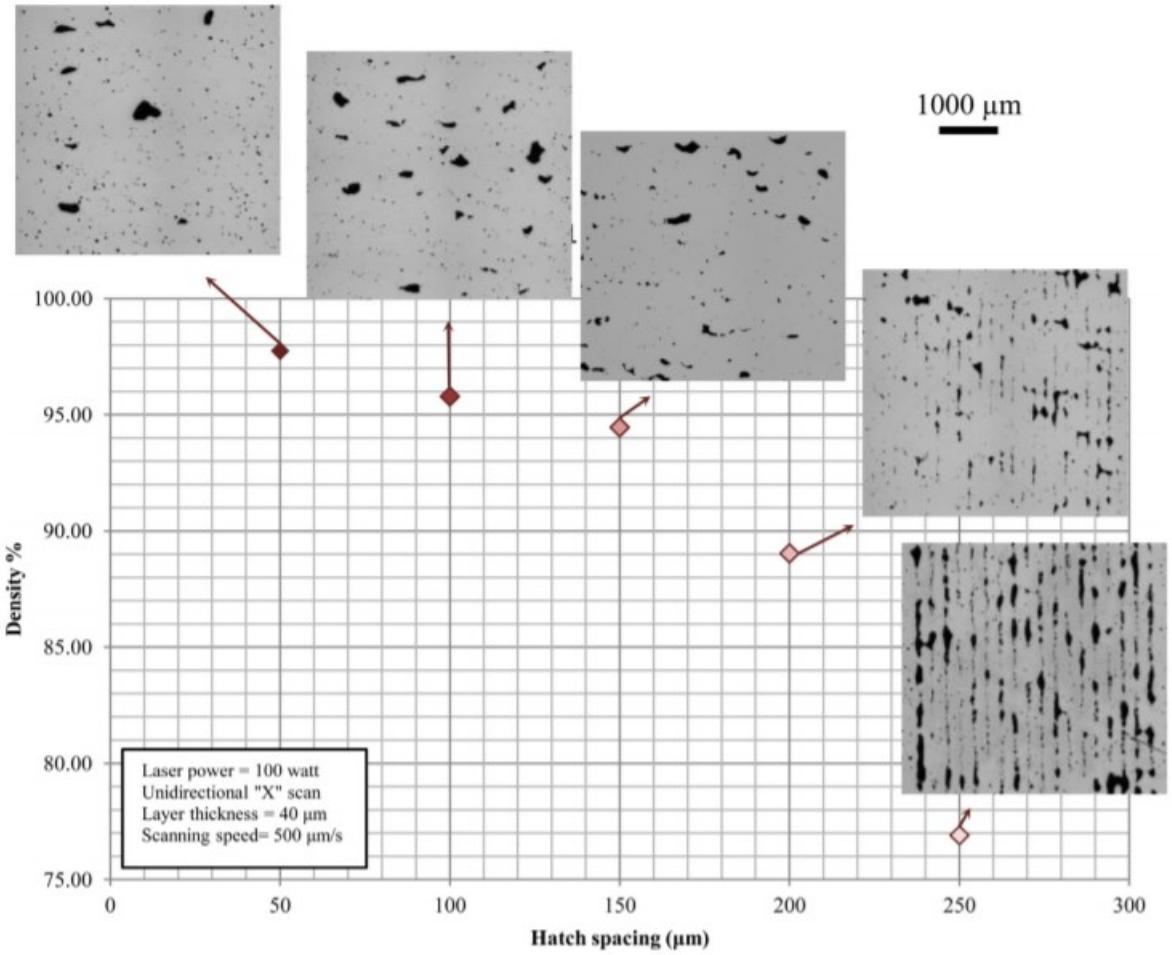

Figure 2.20: Effect of changing the hatch spacing on the relative density/porosity. Material: AlSi10Mg [28].

2.3.1 Scan strategy of LPBF process

One of the objectives of the LPBF is certainly to completely dissolve the powder in order to obtain high density products. One solution to avoid them is to adjust the scanning strategy. Consider, therefore, four scanning strategies the four scanning strategies shown in Fig. 2.21.

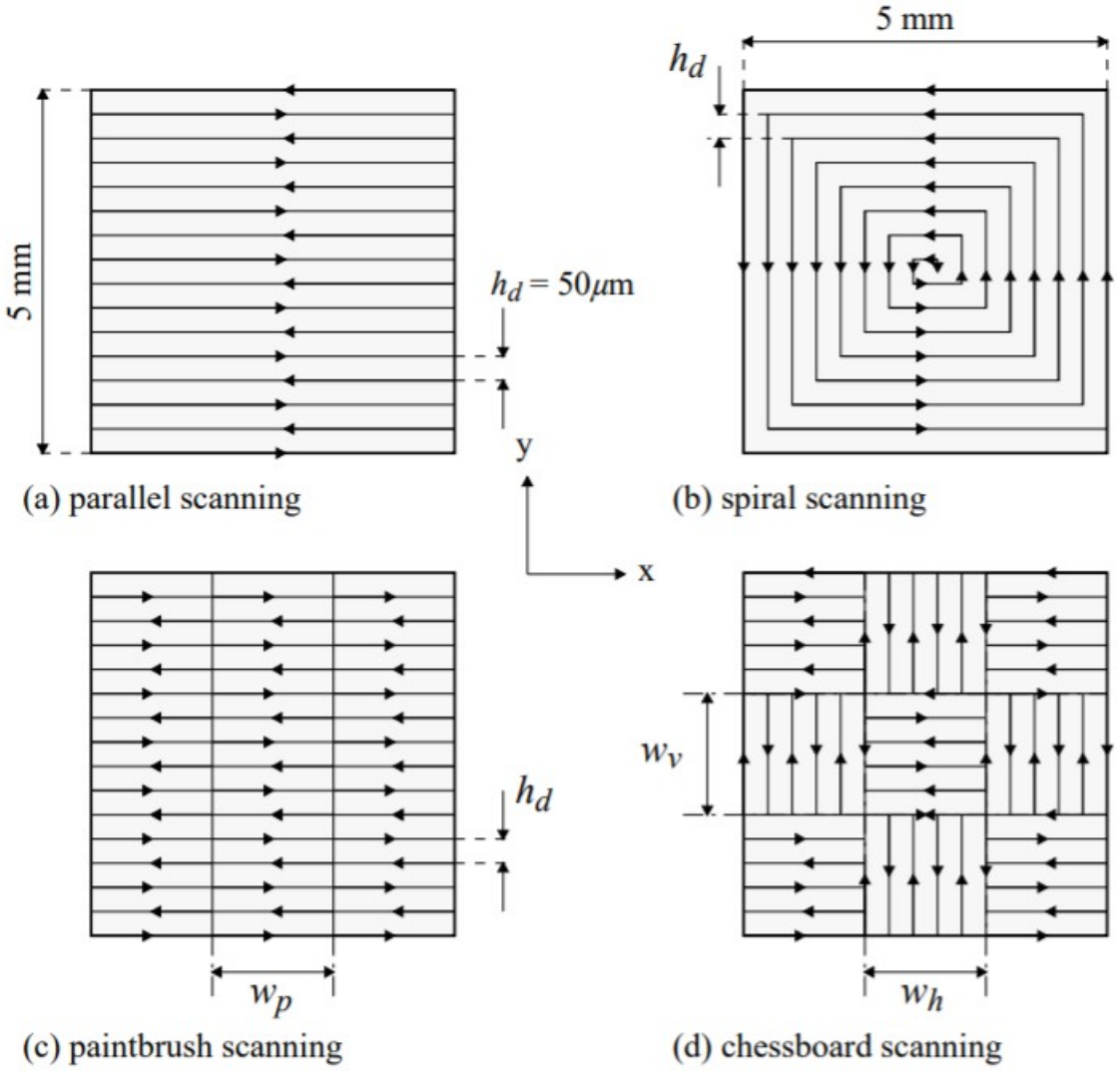

Figure 2.21: Four example of LPBF scan strategy [29].

The parallel scanning strategy (Fig. 2.21a) is the simplest to produce a component from a CAD design. From the studies, that will be presented in this section, we will see that for this particular scanning strategy, it is verified that it is convenient to have high scanning speeds

and, consequently, the laser power must be increased accordingly which, however, is limited by the limits of the laser itself. One possible solution is the multiple scan strategy: the laser beam passes through the scan path n-times. [29]. The inequality in the two directions is solved in the spiral scanning strategy (Fig. 2.21b). At high speeds this strategy is much better than the parallel one. If the starting powder is highly conductive, the multiple spiral strategy leads to very strong bonds between the layers, however, precisely the excellent heat transfer can lead to the melting of parts not hit by the laser, losing the geometric accuracy of the final piece as well as the overheating of the central area of the piece where an extremely rough surface area full of pores will result (Fig. 2.22). In the case of low conduction powder, this scanning strategy leads cracks and balling on the entire surface [29].

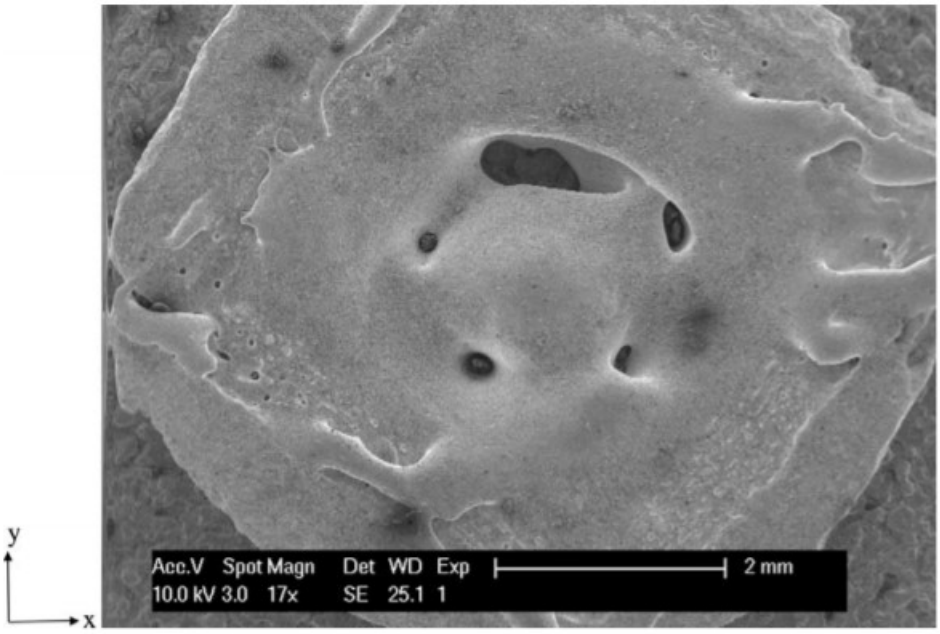

Figure 2.22: Example of result of spiral scanning strategy[29].

The third scanning strategy, paintbrush strategy (Fig. 2.21c), is a valid alternative to the parallel strategy, since it has a much smaller scan width and therefore can limit overheating of the areas and temperature gradients. This strategy, however, does not lead to a solid bond between the layers and therefore the effect of delamination is very frequent (Fig. 2.23).

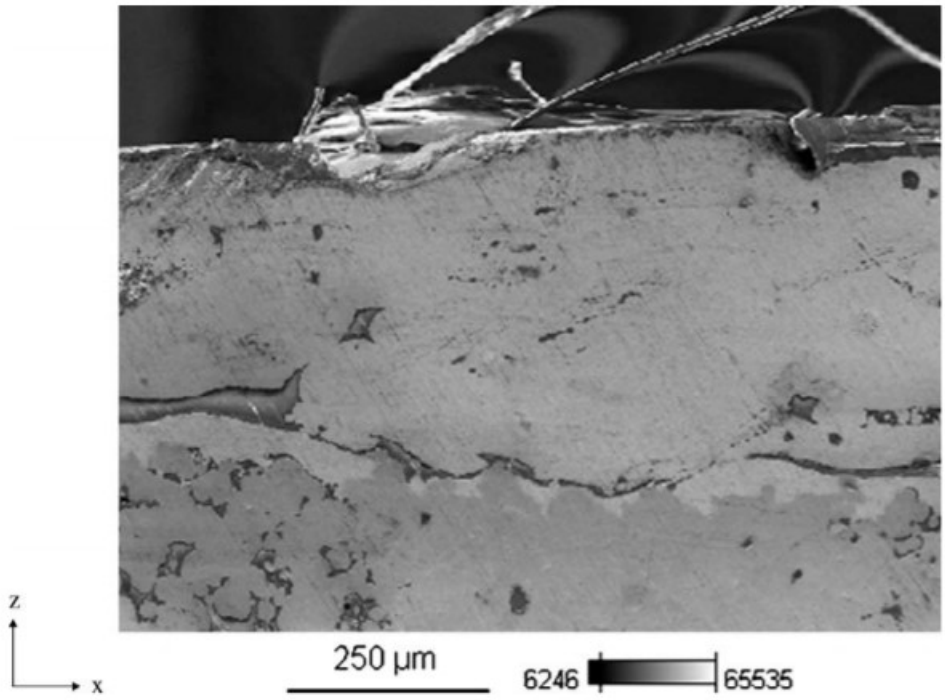

Figure 2.23: Delamination on a component made with spiral scanning strategy[29].

The last scanning strategy taken into consideration is the checkerboard strategy (Fig. 2.21d), in which the scanning area is divided into small cells by carrying out a parallel scan in alternating directions. It is shown that this strategy limits the inhomogeneity of temperature if, however, small cells are fused in random order [29].

2.3.2 Characteristics of LPBF part

The main characteristics of parts produced by LPBF are summarized below:

- Density.
  The development of the LPBF process has led to the birth of many studies that aim to explain how the optimization of process parameters leads to improving the characteristics of the product. In particular, we want to achieve a density [%] of the final product as high as possible. It has been shown how it can be related to the energy density (E_d) [J/mm^2], equal to:

$$E_d = \frac{P}{v h_d} \tag{2.3}$$

  Where: P is Laser Power [W], v is scanning speed [mm/s] and h_d is hatching distance [mm]. The density-energy density correlation is shown in Fig.2.24. Two areas can be

distinguished, one with the presence of large voids (High Area), while the other with the absence of voids (Low Area), ie where the process is able to dissolve and densify the powder. It can be seen that the two areas have a clear gap, which is common to all Nickel alloys. This can reasonably be associated with the fact that, regardless of the properties of the nickel-based alloy under consideration, the powders have a very similar specific absorption [30].

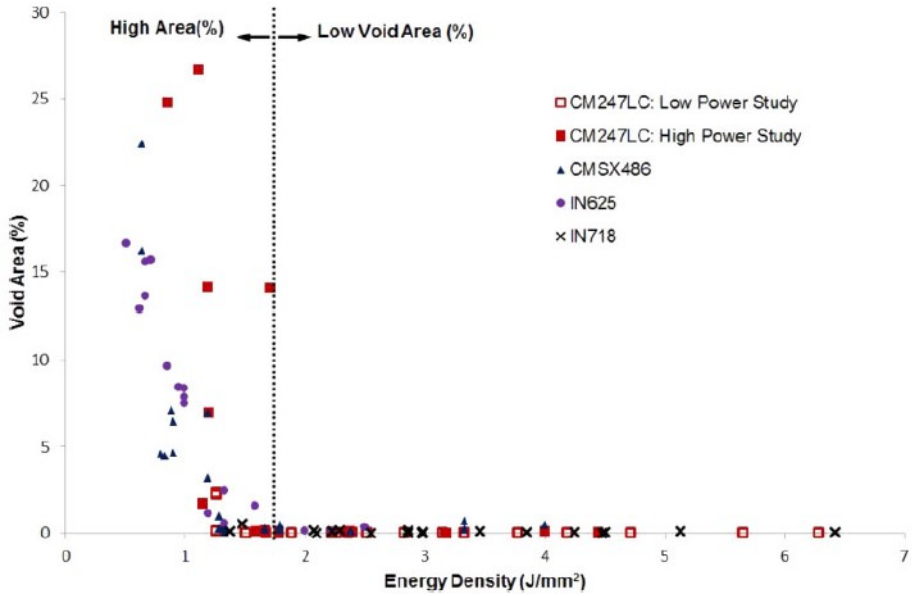

Figure 2.24: Energy density-density of Nickel- based superalloy by LPBF [30].

- Surface Quality.
  The surface quality of parts produced using LPBF is one of the big drawbacks that this process has. The market offers various solutions, especially traditional processes. Re-melting could also greatly improve the surface quality (fig. 2.25), However, crests of material could be created due to the metal being pushed to the edges during re-melting [31].

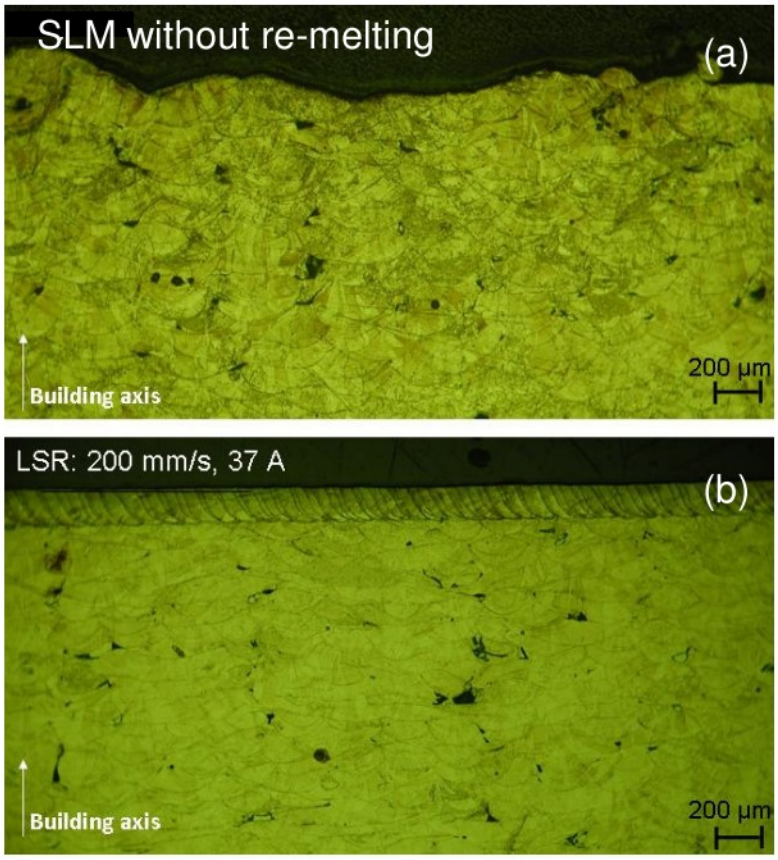

Figure 2.25: Effect of re-melting on surface quality. (a) LPBF without re-melting, (b) LPBF with re-melting.

- Mechanical Properties.
  Mechanical properties of LPBF parts depend on material composition, on the microstructures obtained and the presence of defects in the final product that are determined by the process parameters and manufacturing strategy [31]. The mechanical properties that are obtained from the LPBF process of various metals will be discussed later.

- Microstructure.
  The microstructure determines the characteristics of the final component. It is strongly influenced by the process parameters described above, of which we can see some effects in the figures below [31].

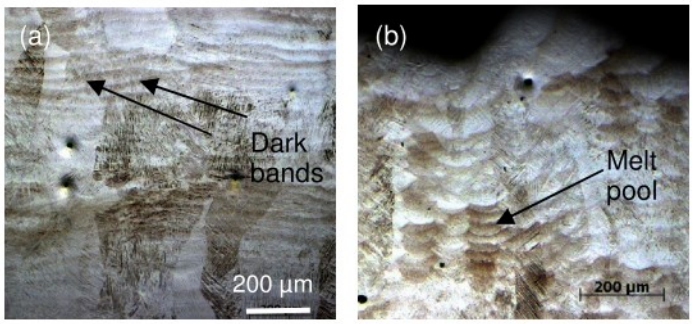

Figure 2.26: Effect of scanning speed on microstructures. A low scanning speed results in the formation of coarser grains aligned with the construction direction and, in the case shown in the figure a) and b), in an elongated and irregular melt pool [31].

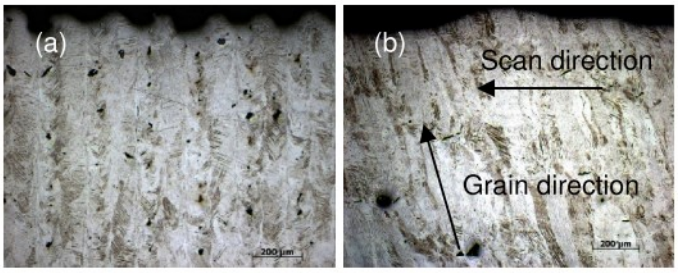

Figure 2.27: Effect of scanning spacing and speed on microstructures. High scan spacing can cause insufficient overlap between adjacent scan tracks and, as a result, the formation of aligned pores. The left figure suggests that the inclination of the pore alignment is influenced by the scanning spacing and the scanning strategy. (a) Spacing equal to the melt width, pores aligned vertically. (b) One-way scanning from right to left with optimized scan spacing. We note how the inclination of the grains depends on the direction of construction. [31].

- Residual Stresses.

  Residual stresses can be a big problem for the component. In fact, they can cause cracks, and cause distortions, which may lead failure by cracking or layer delamination [32]. Due to the localized heating during the LPBF process and to the expansion and contraction of the solidified layers, thermal stresses and phase transformations arise. Residual stresses can cause distortion of the molded component. One technique used to measure residual stresses is the bridge curvature method. A bridge-shaped piece is produced and at the end of the process it is detached from the plate, it will bend by an angle α which will be the measure of the residual stresses (fig2.28). You can change

the process parameters as long as the value of α is not acceptable. In the figures 2.29 and 2.30. It is possible to see the α trend as the scan vectors [mm] and island rotation vary [β] [31].

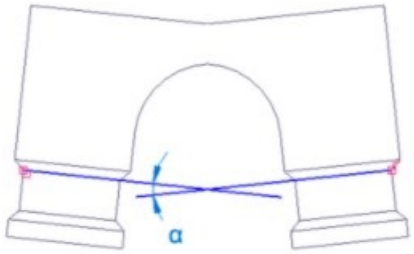

Figure 2.28: Bridge curvature method. This method is based on the production of a bridge-shaped piece that is printed directly on the support, at the end of the process the structure is cut and the angle of deflection between the pillars is measured, which can be associated with residual stresses. This method, however, can only be evaluated in the x direction [33]

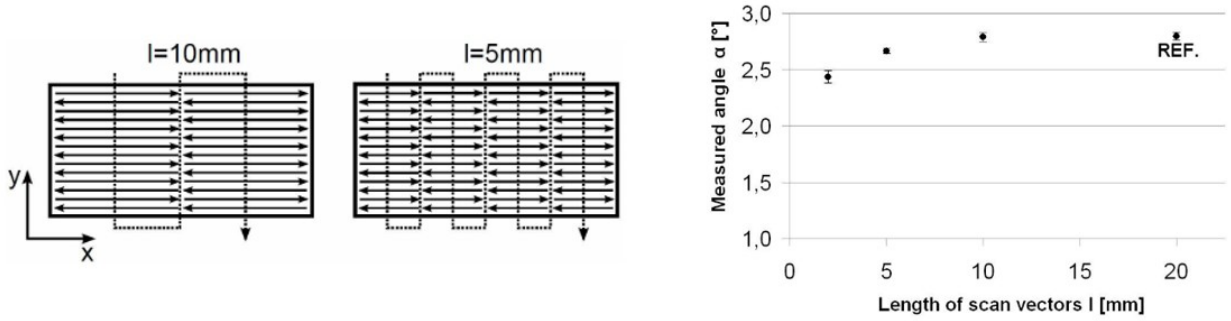

Figure 2.29: Scan vector and its influence on α value [31].

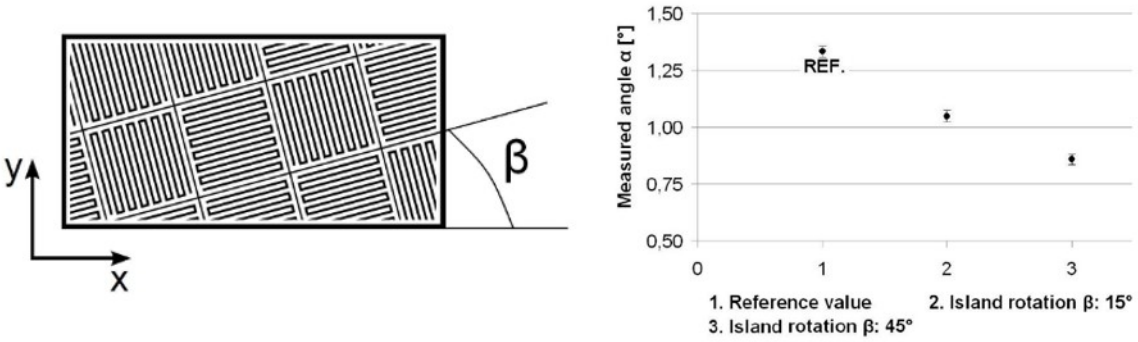

Figure 2.30: Island rotation and its influence on α value [31].

2.3.3 Metals and their applications

The most used metal alloys processed by LPBF are: Aluminium, Titanium, stainless steel and Nickel based superalloys.

Aluminium alloys

Aluminum-based alloys are widely used in various industrial fields due to low density, high specific strength, easy processing, good corrosion resistance, and excellent electrical and thermal conductivity. Fig. 2.31 shows some aluminum alloys and Fig. 2.5 their properties. To date, the aluminum alloys produced through LPBF are mainly Al-Si alloys, but also Al-Mg, Al-Cu-Mg, Al-Si-Mg alloys, aluminum alloys modified with zirconium and other alloys of machined aluminum. About the latter there is little information regarding the properties, but they are the subject of many studies given their excellent potential, for example it is known that Al-Mg-Zn-Cu alloys would be very suitable in the aerospace field, given their high toughness and resistance, obtainable thanks to the precipitation of the Mg-Zn_2 phase.
Al-Si alloys produced through LPBF, thanks to the reinforcement of solid solutions, have a higher yield strength (YS) and a higher breaking strength (UTS) than those machined with traditional processes, but reduced plasticity (Fig. 2.6). Certainly, the mechanical properties changes accordingly to the process parameters.
However, to date aluminum alloys for LPBF technology are very few and little studied. This is due to the formation of pores, cracks and residual stresses during this process, which can certainly be improved by finding the best process parameters, which are not yet optimized [34, 35].

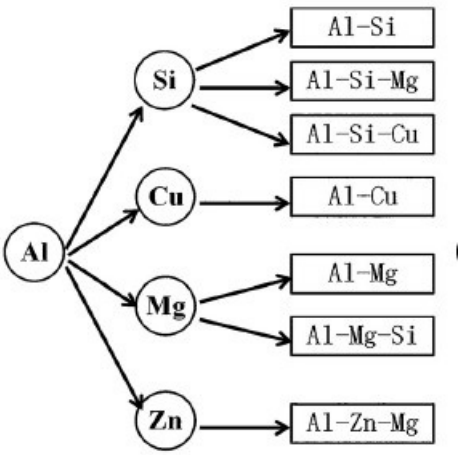

Figure 2.31: Aluminium alloys [35].

Table 2.5: Properties of aluminium series alloys[35].

Elements	Performance
Pure Al(>99%)	Low strength, good corrosion resistance and conductivity, easy processing
Al-Mn	Low strength, cold-working-hardening, good plasticity and weldability
Al-Si	High silicon, low melting point, good weldability, good heat and wear resistance
Al-Mg	High magnesium, good corrosion resistance and weldability
Al-Mg-Si	Medium strength, good formability, weldability and machinability
Al-Zn-Mg	Very high strength, cannot be welded, poor corrosion resistance
Al-Cu Al-Cu-Mg	High strength, good heat resistance, poor corrosion resistance

Table 2.6: Mechanical properties of AlSi12, processed by LPBF and casting for differents scanning strategy. AS= unidirectional scanning strategy, HS= unidirectional scanning and subsequent heat treatment (300°C,6h), CS= checkerboard scanning strategy, CC=circular plastic zone [35].

Test condition	YS [MPa]	UTS [MPa]	ϵ_f [%]
AS$\parallel$	270.1±10	325±20	4.4±0.7
AS$\perp$	274.8±8	296.1±20	2.2±0.3
HS$\parallel$	153.4±5	228±13	5.3±0.7
HS$\perp$	150.3±17	210.1±20	4.2±0.3
CS$\parallel$	262.4±17	330.7±15	3.9±0.6
CS$\perp$	276.6±15	302.7±15	2.3±0.3
CC	104.2±11	192.3±15	9±0.5

Titanium

Titanium and its alloys have excellent mechanical properties, good corrosion resistance and excellent biocompatibility, which is why they are particularly suitable for use in the biomedical field. Currently, the use of titanium alloys in LPBF technology is limited to CP-Ti, Ti-6Al-4V and Ti-6Al-7Nb alloys. These are divided into α-Type (Cp-Ti), $\alpha + \beta$-Type (Ti–6Al–4V and Ti–6Al–7Nb) and β-Type (Ti–24Nb–4Zr–8Sn). Tab. 2.7 shows the characteristics of these alloys processed through LPBF compared with traditional technologies. As for the α-Type alloys, the table shows how, through LPBF technology, it is possible to obtain a yield strength ($\sigma_($0.2)) and a breaking strength ($\sigma_(UTS)$) higher than the same material sheet forming and full annealed. Furthermore, the Vickers micro-hardness is higher than that of the cast alloy and equal to 55% of the cold rolled Cp-Ti. The $\alpha + \beta$ alloys, in particular the Ti-6Al-4V alloy, produced by LPBF, allows to obtain micro-hardness, and in general the properties of the material, clearly superior to that produced by casting, as shown in Tab. 2.7. The β -Type alloys are of particular interest since they have characteristics very similar to those of human bone, however it remains a poorly studied material. However, it should be specified that the final characteristics of the material produced through LPBF are strongly influenced by the process parameters. Figs. 2.32 and 2.33, show the trend of the porosity of Cp-Ti as the laser power varies and the trend of porosity and Vickers micro-hardness with the scanning speed of the Ti-24Nb-4Zr-8Sn, respectively [34, 36].

Table 2.7: Comparison of Vickers hardness and tensile mechanical properties of different types of titanium alloys processed by LPBF and traditional methods [36].

Processing method	Hv	E [GPa]	$\sigma_0.2$ [MPa]	$\sigma_U TS$[MPa]	ϵ_f[%]
CP-Ti					
LPBF	261±13	106±3	555	757	19.5
LPBF	-	-	500	650	17
Sheet forming	-	-	280	345	20
Full annealed	-	-	4.32	561	14.7
Ti-6Al-4V					
LPBF	409	109	1110	126.7	7.28
Casting	346	110	847	976	5.1
Ti-24Nb-4Zr-8Sn					
LPBF	220±6	53±1	563±38	665±18	13.8±4.1
Hot rolling	-	46	700	830	15.0
Hot forging	-	55	570	755	13.0

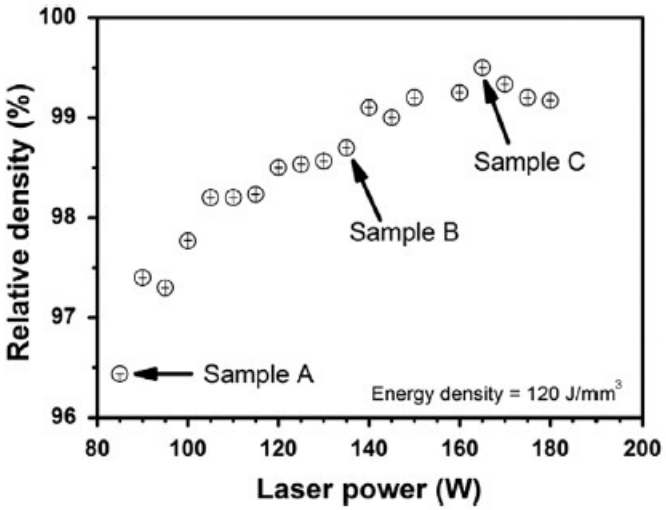

Figure 2.32: Trend of the porosity of Cp-Ti as the laser power varies [36].

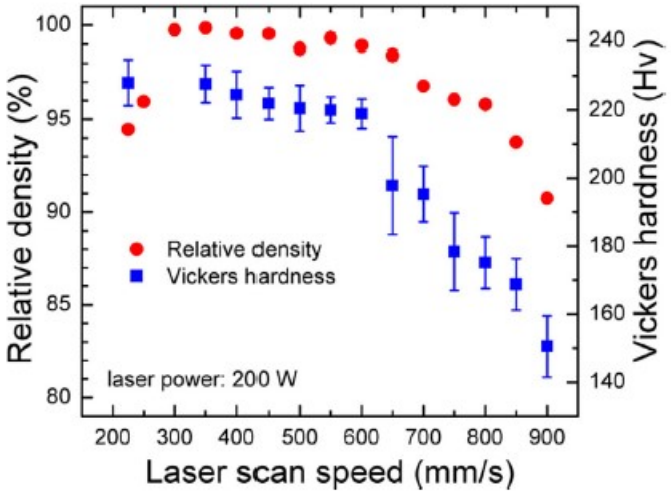

Figure 2.33: Vickers micro-hardness with the scanning speed of the Ti-24Nb-4Zr-8Sn [36].

Stainless Steel alloys

Depending on the thermal history and composition, stainless steels can occur in different crystallographic and microstructural forms. Tthey can be ferritic BCC (α-δ), austenitic FCC (γ), and martensitic BCC or BCT (α'). Austenitic steels have a high resistance to corrosion and ductility, but low mechanical strength, on the contrary, ferritic steels have high strength and hardness while low toughness and ductility, martensitic steels instead do not see good corrosion resistance, due to the very low chromium content. Tab. 2.8 shows characteristics of two stainless steel alloys: 304L and 316L. The most common is the 316L austenitic stainless steel, that has high resistance to oxidation and corrosion, therefore it is widely used in the marine, oil, gas and biomedical industries. Thanks to the LPBF it is possible to obtain, compared to the forging or cast process, a 316L stainless steel much more resistant to traction (UTS of 450-555 MPa for conventional technology), with higher yield strength (YS of 160-365 MPa for conventional technology) that keeps a good flexibility. This is certainly due to the presence of numerous nano-inclusions that hinder dislocation movements, and a large density of low angle grain boundaries.[33, 34, 37, 38].

Table 2.8: Characteristics of 304L and 316L processed by LPBF [25]

Material	UTS [MPa]	YS [MPa]	Elongation [%]	HV
304L	717	570	42.8	217
316L	760	650	30	279

Steel and Iron-Based Superalloys

The main advantage in the manufacturing of steel parts lies in the possibility of exploiting the toughness of the material and having a huge saving in weight. By exploiting a high laser power and a low scanning speed, densities up to 99.9% can be obtained. The obtainabed characteristics by LPBF are show in in tables 2.9, 2.10, 2.11 and 2.12 [25].

Table 2.9: Highest relative density of LPBF iron and steel-based alloys [25]

Material	Highest relative density [%]
Fe	99
Fe+0.8% C	93
Fe-Al intermetallics	98
Fe3Al	99.5
Fe-Ni	98
Fe-Ni-Cr	99.5
Fe-Ni-Cu-P	97.5
316L stainless steel (laser re-melting)	99.95
M2 high speed steel	97
AISI Marage 300 steel	99.99
Ultra high carbon steel	92

Table 2.10: Tensile strengths of LPBF steel and iron-based alloys [25]

Material	UTS [MPa]	YS[MPa]	Elongation [%]
Fe	411.5	305.3	
Fe-Ni	600		
Fe-Ni-Cr	1100		
Fe-Ni-Cu-P	505	425	
Marging steel	1290	1214	13.3

Table 2.11: Surface roughness of LPBF steel and iron-based alloys [25]

Material	Surface roughness, Ra [μm)]
Fe-Ni	10
Fe-Ni-Cr	10
Ultra high carbon steel	18
Fe-Ni-Cu-P	505

Table 2.12: Micro-hardness of SLM steel and iron-based alloys [25]

Material	Micro-hardness [HV]
Fe-Al intermetallic	800
Fe3Al	353
Fe-Ni	232
Fe-Ni-Cr	450
Fe-Ni-Cu-P	230
H20 tool steel	336
M2 high speed steel	900
Maraging steel	412
X110CrMoVAl 8-2 tool steel	493
Ultra high carbon steel	475

Depending on its properties, steel is used in different fields. The ability to develop parts with complex geometries thanks to the additive makes this material suitable for cooling channels and light structures in both the aerospace and automotive fields [25].

Nickel

The nickel superalloy that can be studied and used is certainly Inconel, particularly suitable for high temperature and low fatigue applications. These super alloys combine the best physical and mechanical characteristics, they are particularly appreciated in the aerospace field. The main characteristics are summarized into tables 2.13, 2.14 and 2.15, but they will be discussed in depth later [25, 20].

Table 2.13: Highest relative density of nickel-based alloys [25]

Material	Highest relative density [%]
Inconel 625	95
Inconel 718	99.98
Chomel	88
Hastelloy X	99.7
Inconel 738 [39]	99.93
Inconel 939[40]	>99.5

Table 2.14: Tensile strengths of LPBF Inconel and nickel-based alloys [25]

Material	UTS [MPa]	YS [MPa]	Elongation[%]
Inconel 625	1030	800	100
Inconel 718	1148	907	25.9
Chomel	1184	933	8.40
Hastelloy X	930.5	814	35
Nimionic	1085	818	34
Inconel 939 [41]	1252	897	20
Inconel 738 [42]	1076.5±28.9	804.0±49.5	16.85±0.07

Table 2.15: Micro-hardness of LPBF Inconel and nickel-based alloys [25]

Material	Micro-hardness [HV]
Inconel 625	163
Inconel 718	365
Chomel	740
Nimionic	370
Inconel 939 [41]	318
Inconel 738 [39]	382±6

The excellent characteristics of the nickel superalloy components produced through LPBF have made it particularly suitable for high temperature applications. It is then used for making gas turbine blades and turbochargers, as well as for repair patches [25].

Figure 2.34: Turbine blades in high-performing polycrystalline nickel superalloy molded using LPBF, prouced by Siemens. These blades are tested under engine conditions, maximum load, at 1250°C and 13000 rpm [43].

2.4 Superalloys

The need to have materials available for high-temperature applications is born with the Second World War, when the gas turbine started to make it way. If previously titanium was used for components at high temperatures, its limits in terms of strength were no longer acceptable. With the term superalloys, it is possible to indicate the nickel-, iron-nickel- and cobalt-based superalloy. These alloys are commonly employed for applications above 540°C. In Fig. 2.35 is shown the trend of the temperature and pressure in a turbofan engine, starting from the last stages of the compressor the temperature becomes too high for the use of titanium, the use of superalloys is ideal, which, to date, represent about 40-50% of the total weight of the engine.
Superalloys exhibit high fatigue strength, good toughness, good corrosion resistance, both at low and high temperatures. Fig. 2.36 shows the trend of the Stress-rupture strengths as a function of the temperature. The figure shows how superalloys owe their strength from solid solution hardeners, that is substituted atoms interfere with deformation, and precipitated phases, that are gamma prime γ' (Ni_3 $AlNi_3$(Al, Ti)) and gamma double prime γ'' (Ni_3 Nb) present in Fe-Ni- and Ni- based superalloys. These two phases, as shown in the figure, are able to significantly strengthen the two classes of superalloys. The figure shows another type of strengthening, i.e. for carbides, which reinforces directly, if we are talking about dispersion, or indirectly, if we are talking about stabilizing grain boundaries against excessive shear, however, a reinforcement limited to superalloys. Carbides are considered to be advantageous when precipitated at grain boundaries, increasing the rupture strength at

elevated temperatures, instead too large a number of carbides, placed at the grain boundary, have negative effects on ductility a because of their inherent fragility. In addition to elements that promote the formation of carbides and gamma prime phase or produce hardening by solid solution, superalloys, in particular based on nickel and nickel-iron, see other elements (Boron, zirconium, Hafnium) that improve their properties mechanical and chemical. [44, 45].

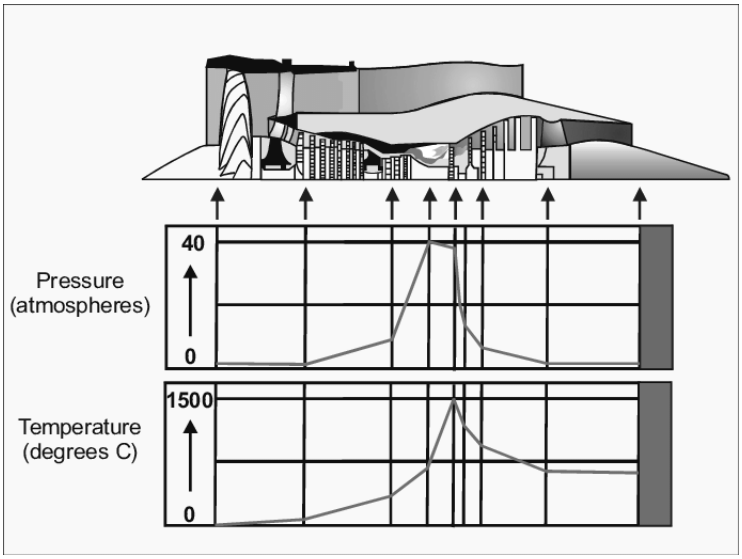

Figure 2.35: Distribution of Temperature and Pressure in a turbofan engine. From the combustor chamber the temperature is too high for titanium alloy, since its specific resistance decreases at lower temperatures than those reached [45, 46].

Tab.2.16 shows the percentage by weight of the three classes of superalloys mentioned above. Even though the cobalt-based alloys have good mechanical properties and resistance to wear and high temperatures, the absence of the γ' phase does not allow this alloy to have characteristics on a par with Nickel superalloys. Another difference between superalloys is density, a characteristic that is fundamental in the choice of material for aeronautical turbines as higher density can lead to an increase in coupling stresses. Cobalt-based superalloys have densities ranging from 8.3 to 9.4 g/cm^3, significantly higher than nickel-based (7.8-8.9 g/cm^3) and iron-nickel-based (7.9- 8.3 g/cm^3). Cobalt-based superalloys are clearly inferior in terms of creep resistance at high temperatures than those based on nickel-iron and nickel, the former particularly suitable up to about 650°C and the latter for even higher temperatures [44].

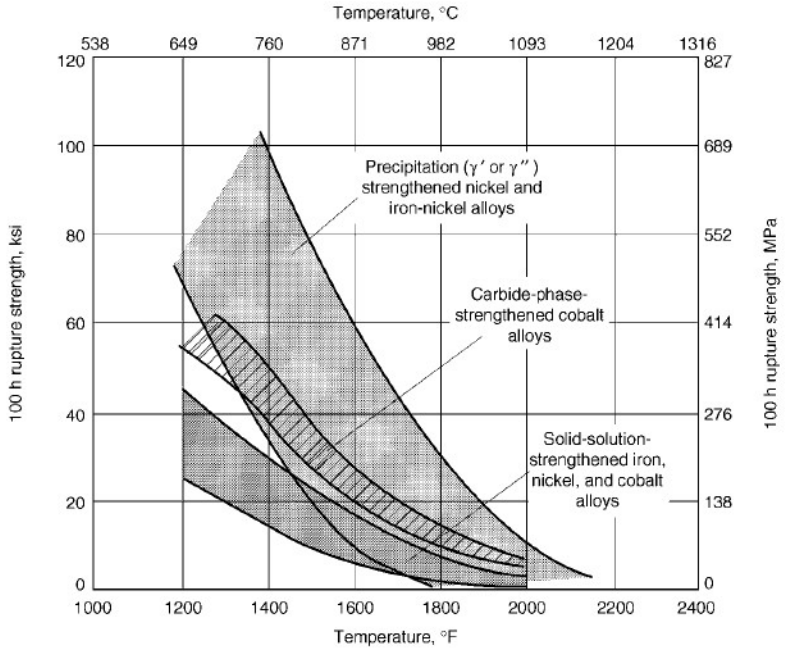

Figure 2.36: Stress-rupture strengths of alloys. The figure shows the trend of rupture strenghts with temperature of nickel-, iron-nickel- and cobalt- based alloys reinforced by different phases [44].

Table 2.16: Weight per cent of Ni-, Fe-Ni-, Co- based alloys [47].

Element	Ni	Fe	Cr	Ti	Al	Mo	Nb	Co	W	C
Fe-Ni-based Weight[%]	9-44	29-67	0-25	0-3	0.3-1	0-3	0-5	0-20	0-2.5	<0.35
Co-based Weight[%]	0-35	0-21	19-30	0-3	0-0.2	0-10	0-4	40-62	0-15	0-1
Ni-based Weight[%]	37-79.5		5-22	0-5	0-6	0-28	0-5.1		0-15	<0.3

2.4.1 Nickel-based alloys

Nickel-based alloys consist of up to 40% weight of nickel and combinations of other five or ten elements. They have an FCC structure which gives the alloy a high number of sliding systems and, consequently, good ductility.
As previously mentioned,the superalloys, and so Nickel-based, can be divided into solid-solution strengthened and precipitation strengthened. The first family, solid-solution strength-

ened, has a good corrosion resistance. In particualr, Ni-Cu alloys are excellent for welding, but have porosity problems, while Ni-Fe alloys have crack problems. The other alloys reinforced with solid solution have different characteristics according to the elements present. The alloys reinforced by precipitation contain elements such as titanium, aluminum and niobium which, following a heat treatment, form a precipitate which reinforces the material. The most common precipitates are gamma prime γ' (Ni_3Al, Ni_3Ti and Ni_3(Ti, Al)) and gamma double prime γ'' (Ni_3Nb), which form the so-called "superalloys", for example nickel-based alloys with properties of resistance to high stress and corrosion at both low and high temperatures. The latest family of nickel-based alloys, specialty alloys, has excellent resistance to creep at high temperatures obtained by hardening by precipitation and by dispersion of stable particles at high temperatures (such as Yttria). The strenght point of these superalloys is the maintenance of optimal physical and mechanical characteristics (hight temperature strenght, toughness and resistance to corrosion) at high temperatures that can reach, even up to 90% of the melting temperature [45, 48, 49].

2.4.2 Nickel alloys reinforced by gamma prime

The gamma prime γ' phase is formed by the elements of the III, IV and V groups, with the addition of essential solutes, Al and Ti. This phase has FCC structure, shown in Fig. 2.37. The γ' phase is precipitated in the FCC matrix of the form A_3B, usually Ni_3(Ti, Al). The γ' precipitates strengthen the matrix because they hinder the movement of the dislocations. The effects of this step on superalloy strengthening is far more effective than solid solution and carbide strengthening. Fig. 2.38 shows how as the content of Al and Ti increases, the alloy sees an increase in strength. It has been shown, for the nickel alloy MAR-M-200, that the percentage of γ' also positively influences the creep-rupture life, as shown in Fig. 2.39 where we appreciate the increasing trend of the creep-rupture life as the percentage of the phase in the alloy increases.
Given the improvements that the phase gives to superalloys, the development of nickel-based superalloys has moved towards a high volume of γ', going from 25% up to 60% in recent alloys. Another advantage to take into consideration is that the effect of strengthening the resistances increases the tolerance of the material to processing defects only for a precise temperature range which, if exceeded, leads to thermal softening of the material and therefore to processing defect major. A high-volume fraction of γ' allows you to expand this temperature range [44, 50, 45, 51].

2.4.3 Inconel 939

Inconel 939 is a nickel-based superalloy with excellent mechanical properties and a very high resistance to corrosion and to oxidation at high temperatures, allowing this superalloy to work up to 850°C. Its high corrosion and oxidation resistances derive from the high percentages of chromium, which favors the formation of the protective layer of Cr2O3 oxide. This is

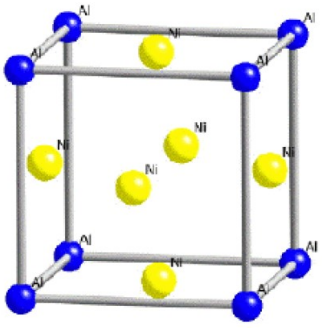

Figure 2.37: FCC gamma prime structure [50]

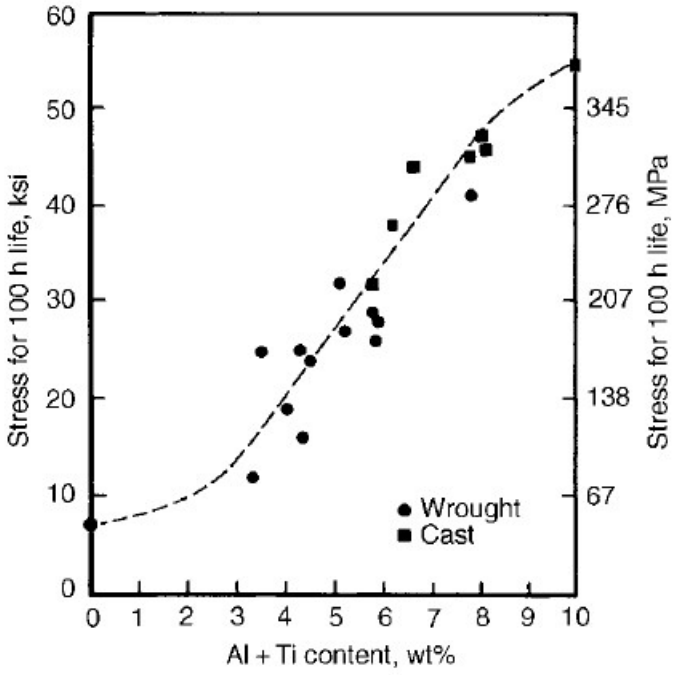

Figure 2.38: Effect of Al+Ti content on the stress-rupture strength of wrought and cast nickel-base superalloys [44]

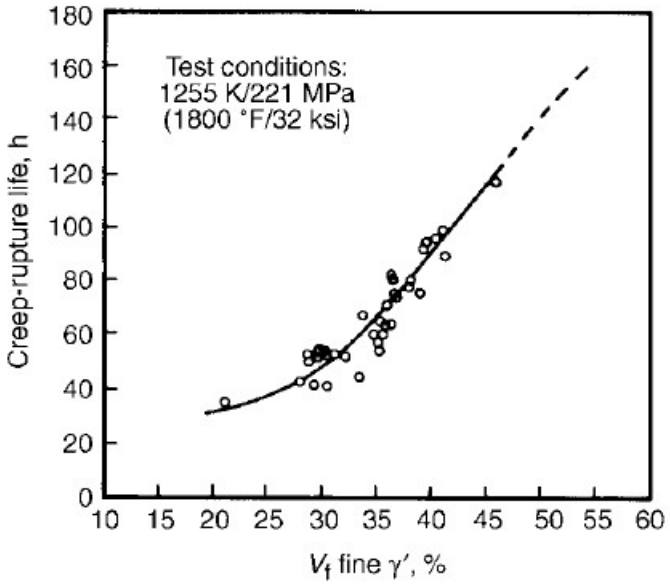

Figure 2.39: Effect of gamma prime on creep-rupture life[44]

extremely useful for the construction of turbines, especially for industrial gas turbines where the hot corrosion induced by the gas is a major regulation in the choice of materials. The table 2.17 reports the chemical composition in %wt, while the table2.18 explains the effect of each element on the alloy [44, 52].

Table 2.17: Chemical Composition of IN939 [41].

Ni	Cr	Co	Ti	W	Al	Ta	Nb	Mn	Si	C	Zr
balance	22	18	3	1	1	1	0.5	-	-	-	-
	23	20	4.5	3	3	1.8	1.5	0.5	0.5	0.15	0.1

2.4.4 Inconel 939 for aerospace application

An interesting study evaluted the possibility to obtain a complex geometry from a single casting for large aircraft engine components [54]. In Ref.[54] It is considered the component shown in Fig. 2.40. and mechanical properties at different temperatures are taken into account for cast material, welded material, and sprayformed material, whose data are shown in Tab. 2.41. First of all, it is possible to note how the fluidity of IN 939 enabled to realize the model with traditional technology casting in one piece, making all of the elements designed down to 2 mm thickness. Secondly, it was analyzed the weldability with both TIG and EB technologies. Finally, it was evaluated the component realized by spray formed. Mechanical properties are shown in Fig.2.42.

Table 2.18: Effects of each element on IN939 alloy [52, 53].

Elements	Effects
Cr	- promote formation of the protective Cr_2O_3 oxide layer - solid- solution strengthener - appears in the form of carbides
Co	- prevent formation of η phase during heat treatments (stiffening and embrittlement) - raises solvus temperature of γ' elements - promotes the precipitation of reinforcing intermetallics - gives the alloy a good long-term mechanical strenght
Ni Ti Al	intermetallic $Ni_3(Ti,Al) \rightarrow \gamma'$ precipitate $\rightarrow$ increased resistence at hight temperature
Ti Nb Ta	increased fatigue life

Figure 2.40: CAD model for the evaluation of IN939 [54].

Conventionally cast Material	
Test	**Test condition**
Tensile	RT, 500, 600, 700, 800 °C
LCF	650 °C, R = 0, smooth
Creep rupture	700 and 800°C
LCF	650 °C, R = -1, notched KT=2.2
LCF	650 °C, R = 0, notched KT=2.2
FCGR	RT and 650 C, duplicates
Notched stress rupture	650 °C, 689 MPa per ASTM E292
Welded Material	
Test	**Test condition**
Tensile	RT ,500,600,700,800 °C
Creep rupture	700 and 800°C
Hardness	RT
LCF	650 °C, R = 0, smooth
Sprayformed Material	
Test	**Test condition**
Tensile	RT , 500, 600, 700, 800 °C
Creep rupture	700 and 800 °C
LCF	650 °C, R = -1, notched KT = 2.2
LCF	650 °C, R = 0, notched KT = 2.2
LCF	650 °C, R = 0, smooth
FCGR	RT and 650 C, duplicates, R = 0.05
Notched stress rupture	650 °C, 689 MPa per ASTM E292

Figure 2.41: Data for IN939 test [54].

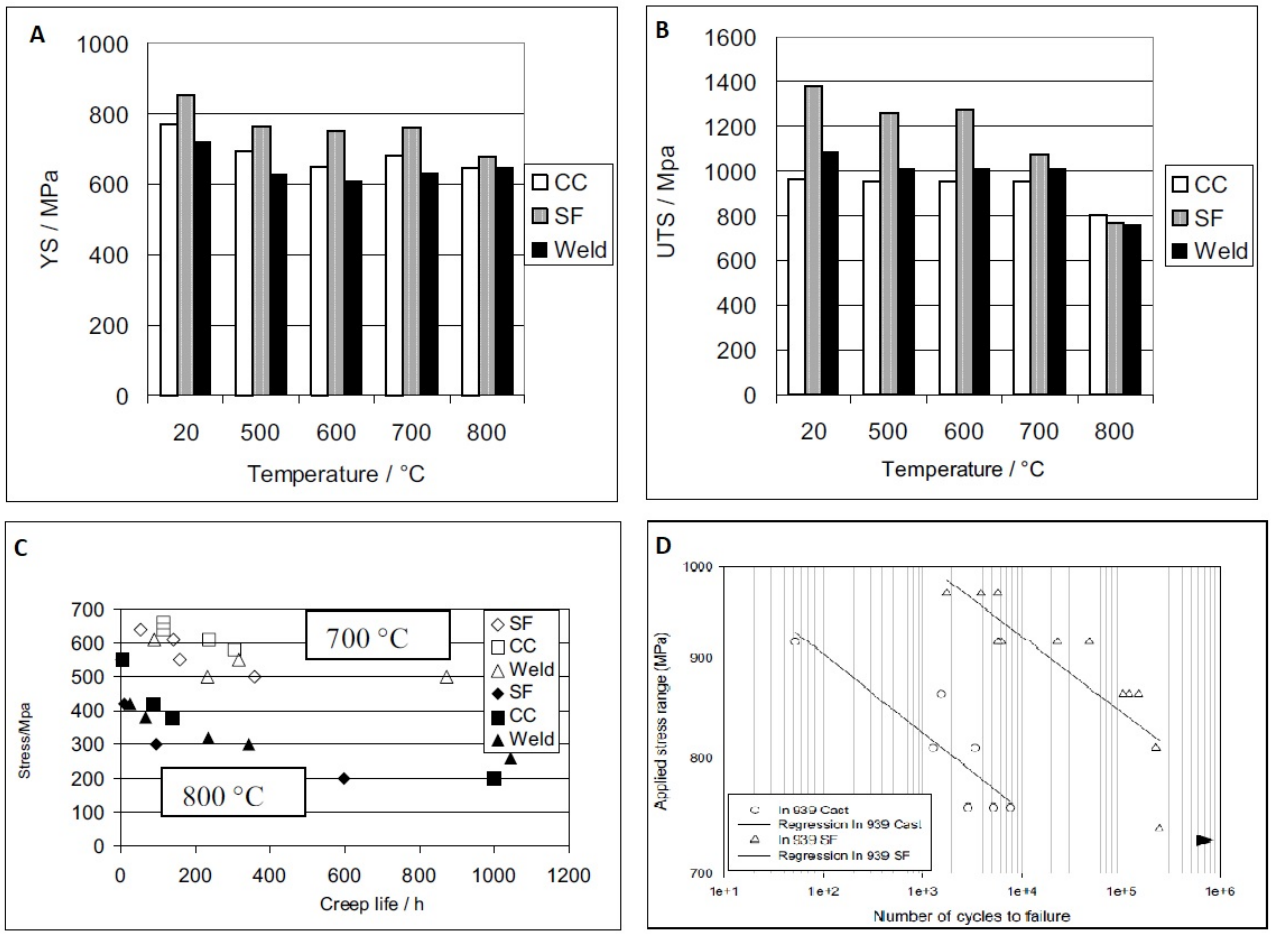

Figure 2.42: Mechanical properties calculated in the IN939 test.
A and B show tensile properties, while C shows creep and stress rupture properties and D fatigue properties [54].

2.4.5 Inconel 939 processed by Laser powder bed fusion

The excellent properties of IN939 make it a superalloy highly suitable for the aerospace and energy sectors. The LPFB can help to obtain complex shape parts made of Inconel 939. However, the characteristics will certainly be different compared to the material obtained through traditional processing, depending, above all, on the processing parameters and post-processing heat treatments. As shown in Fig.2.44 of the two "dog bone" samples, one made with traditional cast and the second with LPBF technology (Fig.2.43), the second shows clearly better results in terms of ductility, elongation factor doubles, with the same yield point already in the as-built condition. The aging treatment involves a reduction of the ductility and an increment of the yield strength39, due to the formation of precipitates

(mainly gamma prime).
The heat-treated Inconel 939 processed by LPBF presented lower ductility than heat-treated as-cast Inconel 939 due to faster precipitation under 750 °C. The tab.2.19 summarize the fatigue properties. The fatigue life is greater in the case of the LPBF samples, this difference can be explained by the corresponding yield values, which were observed in the previous tests. Another interst observation that can be made is the influence of the manufacturing direction on the mechanical properties, analysed thanks to two orientation of speciemen, shown in Fig. graficocastSLM. It is clear that the perpendicular direction (Fig. 2.43b) has significantly better mechanical properties than parallel direction (Fig. 2.43a) ([55].

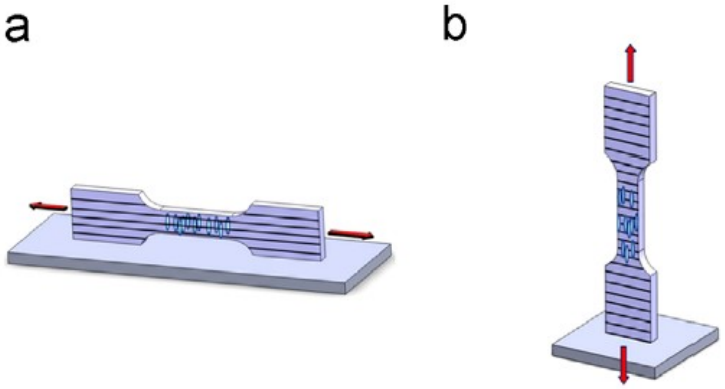

Figure 2.43: Scheme of the "dog bone" specimens, oriented either perpendicualar (a) or parallel (b) to the building platform [55].

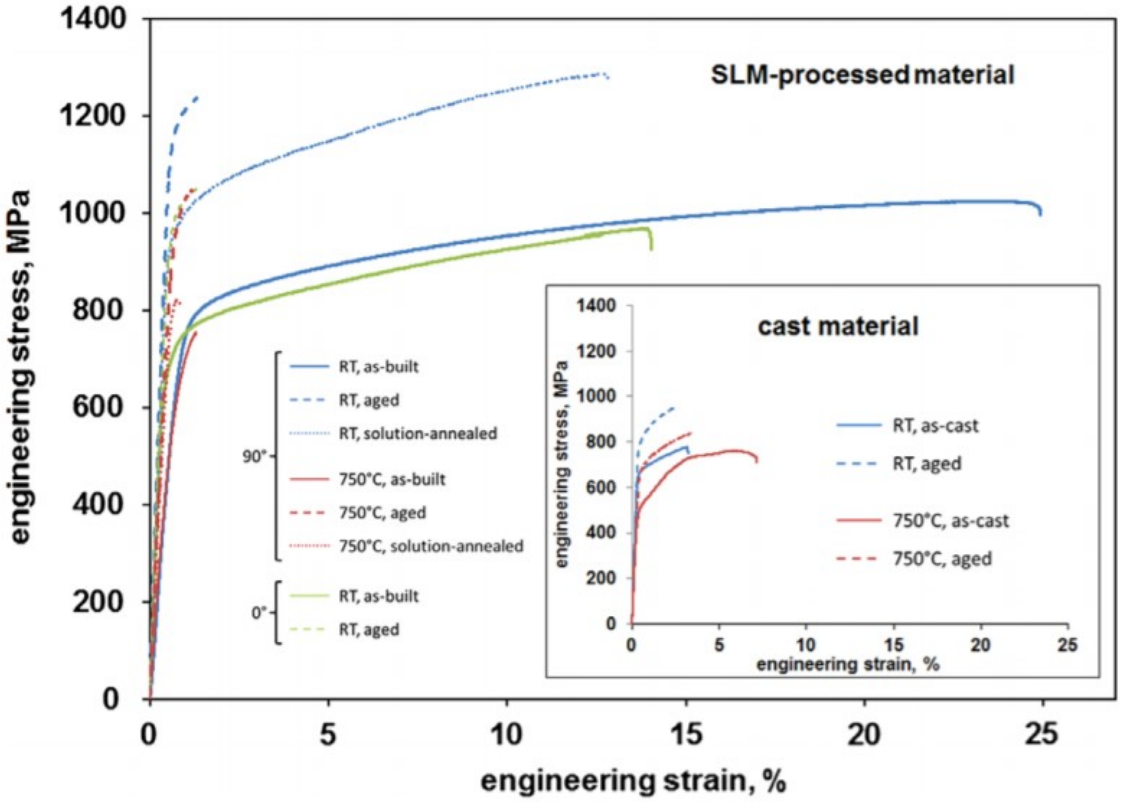

Figure 2.44: Stress strain curves for Inconel 939[55].

Table 2.19: Table of fatigue life [55]

Condition	LPBF-processed as-built	LPBF-processed aged	Cast as-cast	Cast aged
N_f RT	4702	1598	313	2677
N_f 750°C	209	73	230	272

This study compared the mechanical properties of the LPBF and traditional Inconel 939 alloy. However, it is also important to investigate the impact of different process parameters on the material. This alloy presents a reduced process parameter window with respect to other Ni-based superalloys such as Inconel 625 and Inconel 718. Therefore, it is important to define the correct process parameters to minimize the presence of defects in the material. The process parameters influence the characteristics of the material. In Figs.2.45 and 2.46 it is shown in particular how the scanning speed and hatching distance influence the crack

density and the residual porosity. It can be observed that for a specific hatching distance there is an optimal scanning speed value, corresponding to a crack density and residual porosity inferior to 0.5% [56].

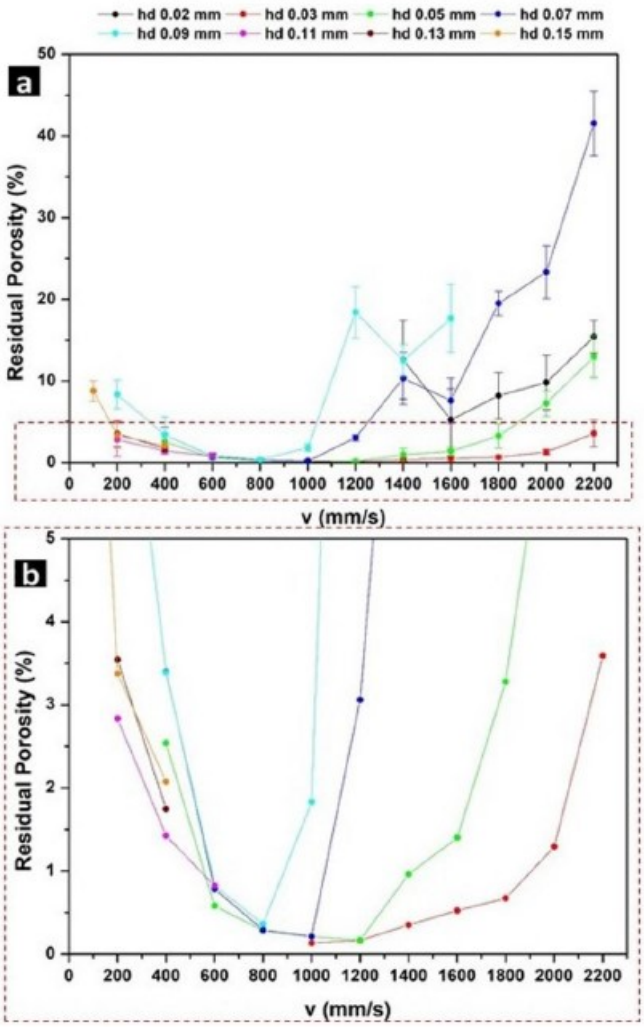

Figure 2.45: Porosity-scanning speed. This figure shows the trend of porosity with scanning speed for IN939 sample built with different values of scanning speed and hatching distance, but constant value of laser power and layer thickness. It is possible to note that for each hatching distance, there is a value of scanning speed that ensures the lowest porosity. The range of scanning speed that allows low porosity (<0.5%) is from 800 to 1000 mm/s [56].

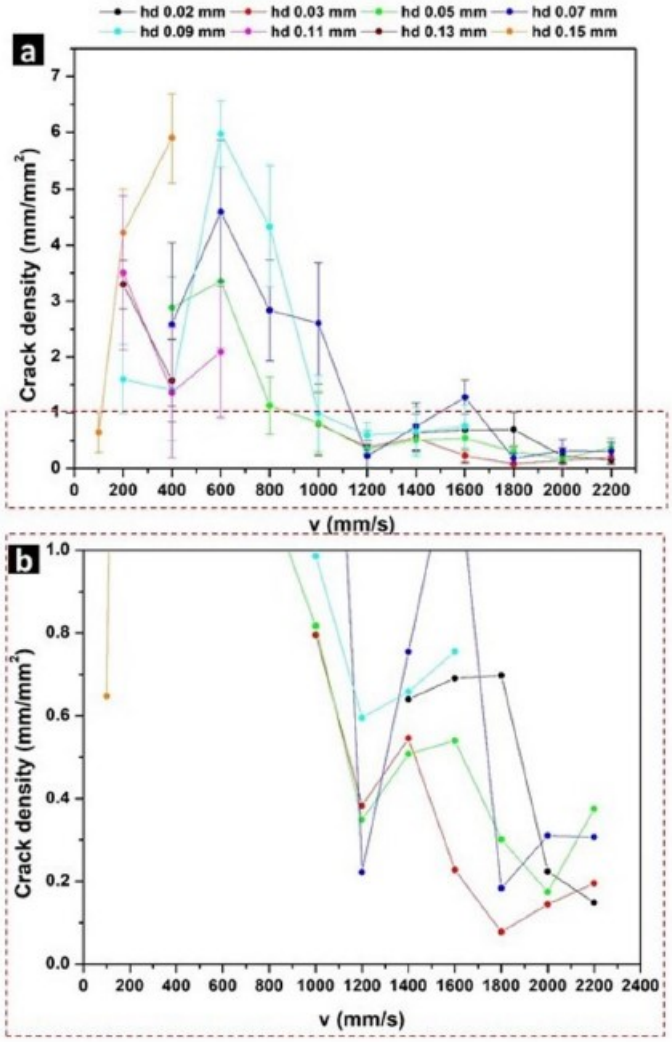

Figure 2.46: Crack density-scanning speed [56].

Another parameter that must certainly be considered is the VED, which represents the combination of the various process parameters:

$$VED = \frac{P}{vth_d} \tag{2.4}$$

From Fig.2.47 a) three different areas can be distinguished. For a VED <50 J/mm^3 there are large pores and irregular lack of fusion, in the 50-160 J/mm^3 range there are spherical pores up to 20 micrometers, between 100 and 160 J/mm^3 there is a high residual porosity , in the VED range >160 J/mm^3 high energy led to instability in the melt pool causing pores up to 100 micrometers. In Fig.2.47 e), on the other hand, there is no particular trend, it can

be observed that for a VED <50 and >300 there is a reduced amount of cracks, due to the presence of large defects that release internal tensions eliminating the formation of cracks.

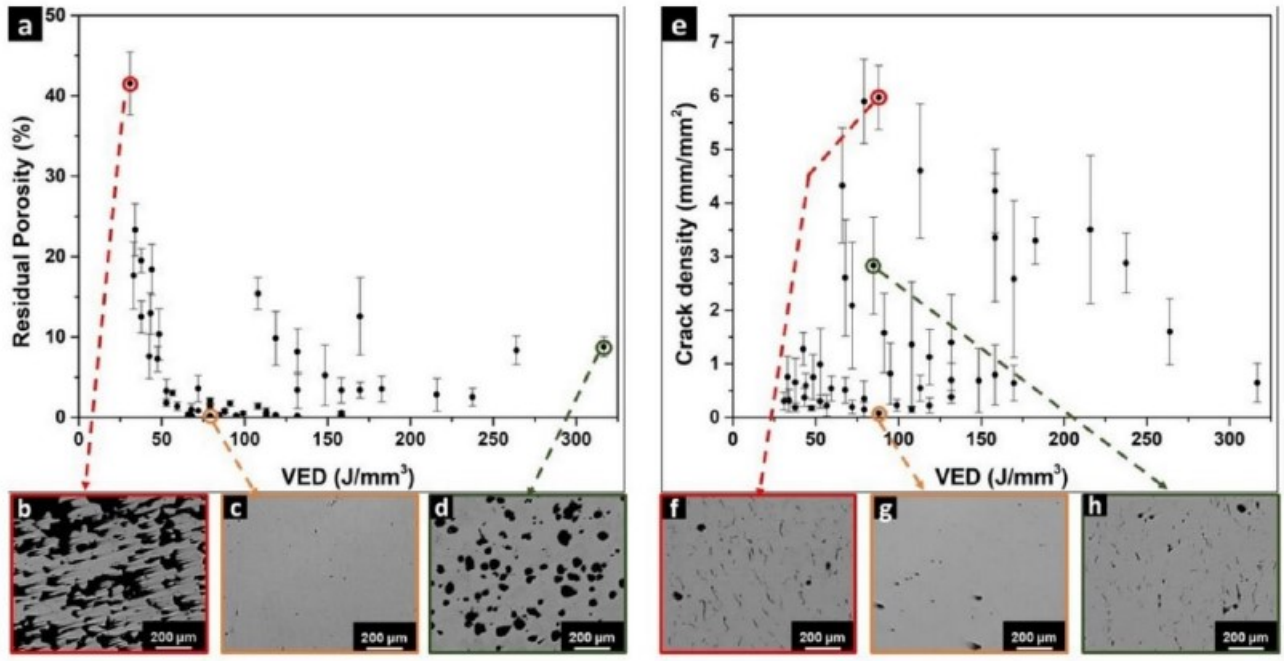

Figure 2.47: The influence of VED with residual stress and crack density [56].

2.5 Heat treatments

All Nickel superalloys generally require one or more heat treatments, both for enabling subsequent treatments, but above all to obtain the optimal properties required. Strictly speaking, heat treatment refers to maintaining at a certain temperature and for a certain time which allows one of the following results to be obtained [44]:

- Reduce stress
- Promotes grain growth
- Promotes the new formation of recrystallized grains
- Dissolve the phases
- Produce new phases, due to precipitation from the solid solution

2.5.1 Type and scope of heat treatments

The thermal processes applied to superalloys are generally the following:

- Stress relieving
- Annealing
- Solutioning
- Ageing

Stress relieving

As the word itself suggests, stress relieving is used to reduce the residual stresses in the component that can lead to geometric distortions in the components and and a possible failure at a stress value lower than expected. This thermal process is performed at a lower temperature than the solubilization temperature of the material. Fig. 2.48 shows the relationship between residual stress and the temperature of stress relieving, it is evident that this thermal process is able to reduce residual stresses by up to 70%, in this case for an optimal temperature of 600°C [44, 57, 58, 59].

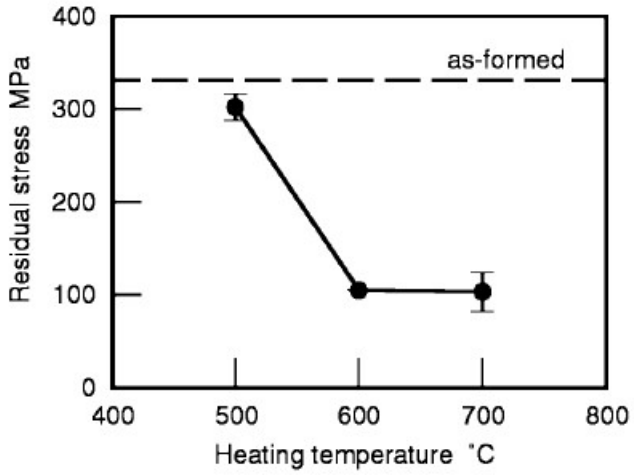

Figure 2.48: Residual stress-temperature of stress relieving treatment [58].

Annealing

The annealing treatment makes it possible to increase the ductility of the material, relieve post-welding stresses, improve the homogeneity of the microstructure thanks to static recrystallization. Annealing, as well as stress relieving, has specific parameters for each alloy,

Table 2.20 shows some parameters for stress relieving and annealing of some nickel-based superalloys [44].
It is possible to understand how each material has its own optimal annealing parameters. An example is shown in Fig. 2.49, where samples of Nimonic 263 produced by LPBF were subjected to the annealing process for 8h with a temperature ranging from 400°C to 1000°C. The figure shows the hardness trend which reaches its peak for 700 ° C and then has a decreasing trend. From this temperature onwards, in fact, the γ' phases increase in size and distance, not blocking the dislocations [60].

Table 2.20: Typical stress relieving and annealing cycles of Nickel-based alloys. *= Full annealing is recommended, because intermediate temperatures cause aging. [44].

	Stress relieving		Annealing	
	T[°C]	h	T[°C]	h
Astroloy	*	-	1135	4
Hastelloy X	*	-	1175	1
Incoloy800	870	1.5	980	1/4
Incoloy800H	-	-	1175	-
Incoloy825	-	-	980	-
Incoloy 901	*	-	1095	2
IN600	900	1	1010	1/4
IN601	-	-	980	1
IN625	870	1	1040	1/2
IN718	-	-	955	1
IN X-750	*	-	1035	1/2
Nimonic 80A	880	-	1080	2
Nimonic 90	*	-	1080	2
Rene 41	*	-	1080	2
Udimet 500	*	-	1080	4
Udimet 700	*	-	1135	4
Waspaloy	*	-	1010	4

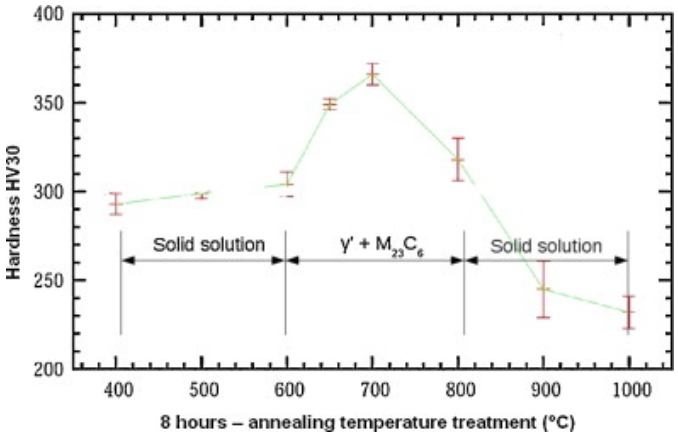

Figure 2.49: Hardess of Nimonic 263, processed by LPBF, versus temperature of annealing [60].

Solutioning

The pourpose of solutioning heat treatment is to to dissolve the degraded precipitation into the γ' matrix and to homogenize the superalloys. Solubilization consists of heating the alloy and a precise temperature, maintaining it for a period sufficient to cause the transformation of one or more constituents into a solid solution and then cooling it rapidly to keep those constituents in the solution. A temperature between 1800 and 2450°F (982-1343°C) is typically achieved, followed by rapid cooling to room temperature. The thermal solubilization process enables the γ' phase to dissolve and secondary carbides. Fig. 2.50 shows the percentage by volume of γ' with the solubilization time at various temperatures for the GTD-111 alloy. It is clear that higher temperatures and longer solubilization times favor the dissolution of γ' . An example of how the solubilization influence the mechanical properties is shown in Tab.2.51. The study conducted on Inconel 713C shows how, compared to the starting sample, the solubilization reduces the dimension of the γ' phase and decreases the creep-life (due to the small dimensions of the γ' crystallite phase and the long distance between γ' particles). However, the rupture lifetime increses [61, 62, 63].

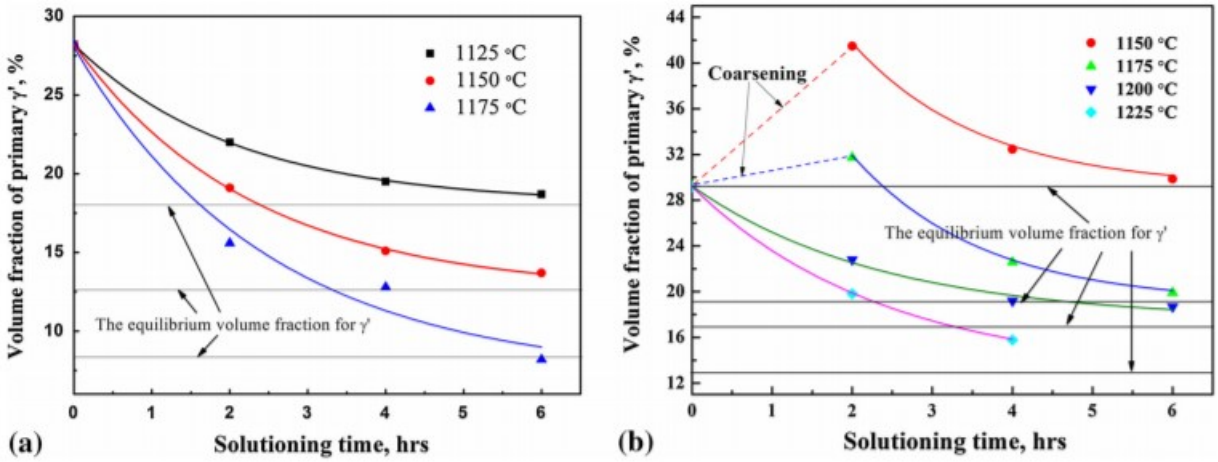

Figure 2.50: Evolution of the volume fraction of γ' with solutioning time (a)Dendrite core and (b)Interdendritics [61].

Samples	As-cast	Solutionized
Rupture time (s)	3576	63
Fracture strain	0.10	0.34
Creep rate in the second stage (min^{-1})	0.0007	–
Mean γ′ crystallite size (nm)	8.5	6.8
Mean length of crept carbides (μm)	50±10	60±10

Figure 2.51: Creep measurements for as-cast and solutioned specimens [63].

Ageing

The thermal ageing process is typically carried out at temperatures between 1000 and 2080°F (537-1137°C)in an inert atmosphere or air for waiting times ranging from 2 hours to over 40 hours depending on the material and microstructure. This process allows the material to be reinforced thanks to the precipitation of one or more phases (γ' and γ'' phases) from the supersaturated matrix that is developed by the treatment of the solution. The temperature at which ageing takes place will affect both the type and the size of the precipitates. Usually this process is performed in several steps, the number, time, and temperature of which depends

on the number and type of available phases, on the service temperature at which the material will have to work, on the combination of ductility and desired strength. Tab. 2.21 shows some examples of solubilization + aging of some Nickel-based alloys [44, 62].

Alloy	Heat treatment
IN100	1080°C/4h/AC + 870°C/12h/AC
IN718	1095°C/1h/AC + 955°C/1h/AC + 720°C/8h/FC + 620°C/8h/AC
IN718 with HIP	1150°C/4h/FC + 1190°C/4h/15ksi + 870°C/10h/AC + 955°C/1h/AC+ 730°C/8h/FC + 665°C/8h/AC
IN738	1120°C/2h/AC + 845°C/24h/AC
IN792	1120°C/4h/RAC + 1080°C/4h/AC + 845°C/24h/AC
IN939	1160°C/4h/RAC + 1000°C/6h/RAC + 900°C/24h/AC + 700°C/16h/AC

Table 2.21: Examples of sol+ageing of Nickel alloys, Inconel serie. AC= air cooling. FC= furnace cooling. RAC= rapid air cooling [44].

An example of the effects of ageing is shown in Figs. 2.52 and 2.53. Fig.2.52 shows how for aging at lower temperatures and longer aging times the hardness is higher and that it decreases with increasing temperature until it reaches a lower hardness than the non-aged sample, when the % of hardnes change becomes negative. The hardness is attributed to the precipitation of carbides during the heat treatment. Again, in Fig. 2.52 it is shown how the micro hardness at the grain boundaries increases due to the presence of carbides. Fig. 2.53 shows that ageing, both at 500 and at 550°C, has improved the yield strength [50].

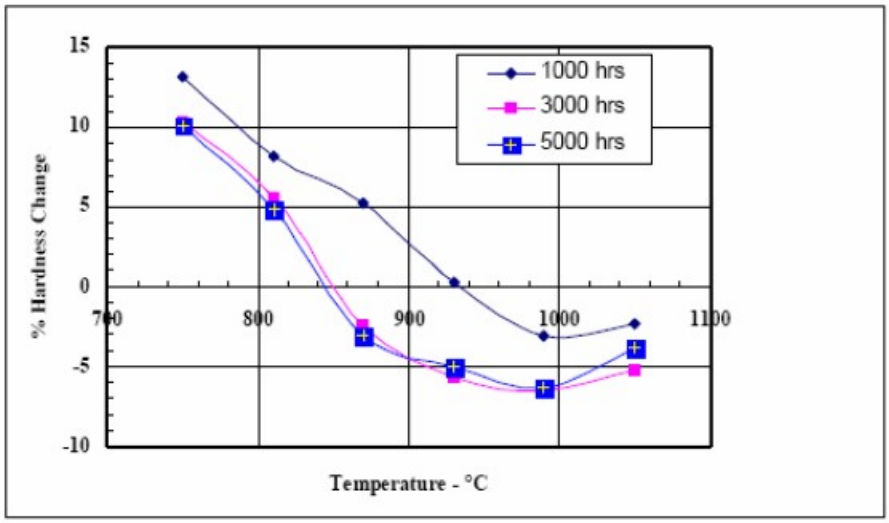

Figure 2.52: Hardness Changing for different ageing [50].

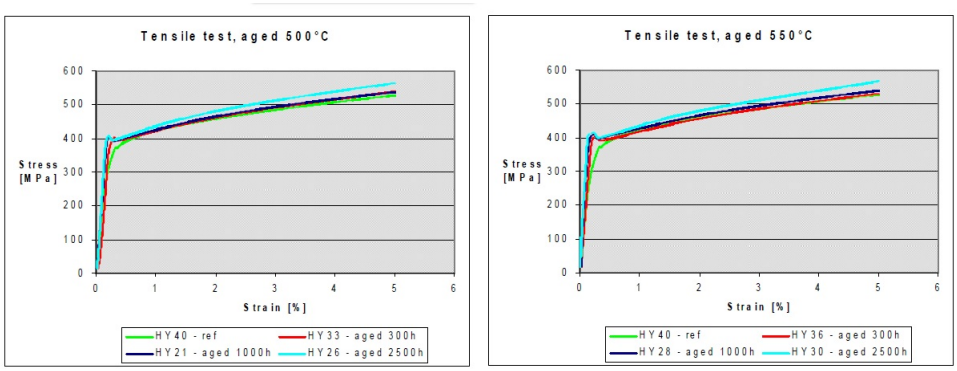

Figure 2.53: Tensile stress for ageing at 500°C (left) and 550°C (right) [50].

2.5.2 Hot isostatic pressing

Hot Isostatic Pressing (HIP) is a heat treatment that allows the material to be densified. The process consists in the simultaneous application of a pressure gradient, by means of inert gas, and of temperature, obtaining the reduction of the pores and cracks inside the material [64]. Numerous studies on the effects of HIP on Nickel-based superalloys have been carried out. Tab.2.22 summarizes different studies on the characteristics of most common Nickel superalloys following the treatment of HIP. The table shows that, for precise temperature and pressure values, the mechanical characteristics improve considerably, the porosity and cracks decrease, making the material more homogeneous.

Table 2.22: Examples of effects of HIP on Nickel-based alloys (traditional technoloy and AM technology)

	T [°C]/ P[MPa]	[h]	Ref.	Effect
IN718 (LPBF)	1160°C/ 100MPa	4	[65]	The area fraction of equiaxed grains increased from 20% to 100% through nucleation and grain growth. The post-processing treatments also provided the drivingforce for the $\gamma'' \rightarrow \delta$ phase transformation and enhanced the nucleation and growth of MC-type carbides. The observed needle-like morphology of the δ-phase is an evidence that it is a grain boundary-type precipitate.
IN718 (LPBF)	1150°C/ 100MPa	4	[66]	After HIP processing, the grains are larger than in the as-built state. The preferential orientation of the grains in the building direction is lost after post-densification. Hence, it can be concluded that the samples show better isotropic material characteristics in this condition. Yield strength is reduced and the tensile elongation and the fracture stress increase.
IN625	1200°C/ 100MPa	4	[67]	The HIP is preceded by a HT (1040°C/1h). The two heat treatments results in an improvement of ductility and homogeneity, but at the expense of lower strength characteristics.
GTD-11	1230°C/ 120MPa	2/4	[68]	The HIP reduces the porosity.
CM247LC	1180°C/ 175 MPa	3	[69]	The HIP is used to repair the cracks following a laser weld repair.
CM247LC	1220°C/ 175 MPa	4	[70]	The fine carbides are uniformly precipitated in the matrix and grain boundaries, thus improving the tensile tests.
IN718	1179.85 °C/ 175 MPa	4	[71]	The HIP treatment showed an increase in hardness to HRC 43.7 and a decrease of about 85.9% in porosity.
IN718	1200°C/ 120 MPa	3	[72]	Increase of YS and UTS and deacrease of ductility.

2.5.3 Heat treatments of IN939

As previously explained, the superalloy IN939, thanks to its excellent properties at high temperatures, is particularly suitable for the construction of the turbine.
To achieve good sliding and tensile properties, a series of heat treatment steps are required, summarized in the Tab. 2.23. The table shows how a four-stage heat treatment varies the microstructure of the superalloy. It should be noted, that the entire heat treatment takes up to 50 hours. However, it was shown that a two-stage treatment (4h 1160°C + 16h 760°C with cooling at 500°C/min) shows similar stress test results to the 4-stage treatment and with an equally good ductility, reducing the hours required for heat treatment from 50 to 20 (Fig. 2.54). Even the high cycle fatigue tests (Fig. 2.55) have shown that the two-stage heat treatment obtains similar results compared to the 4-stage one. The figure also shows how for cycles $> 10^6$ the HIP allows to have the best material for fatigue resistance [73].
Another study analyzes, for IN939, 2, 3 and 4-stage heat treatments [74]. From Fig. 2.56 it can be observed that the creep properties at high temperatures do not depend on the type of heat treatment. On the contrary, at room temperature it is shown how the optimized three-stage treatment (4h at 1160°C + 6h at 1000°C + 4h at 800°C), is the best, ranging from 50h to 14h total (Tab. 2.24) [74].

Table 2.23: Four-stages of heat treatments of IN939 [73].

Heat treatments	Microstructure
as-cast	Cored dendritic (dendrite core Co-Cr-W-rich, Ti-Ta-Nb interdendritic) Primary MC 8 Plates of η clusters in interdendri tic regions γ'/γ eutectic islands, some primary γ' formed on cooling Shrinkage pores (up to 0.3%)
1 stage: solutioning 4h/1160°C/fast air cooled	Homogenisation of γ matrix Dissolution of γ' η rounded or dissolved Primary MC unchanged, secondary MC formed on cooling Fine γ' formed on cooling (20nm)
2 stage 6h/1000°C/fast air cooled	Precipitation of primary γ' (70-150nm) precipitation of MC at grain boundaries
3 stage 24h/900°C	Growth of primary γ' Precipitation of M23C6 on grain boundaries in form of strings of discrete particles
4 stage 16h/700°C	Precipitation of fine γ' to result in bimodal particle size distribution (150nm+20nm) Slight increase in amount of M23C6

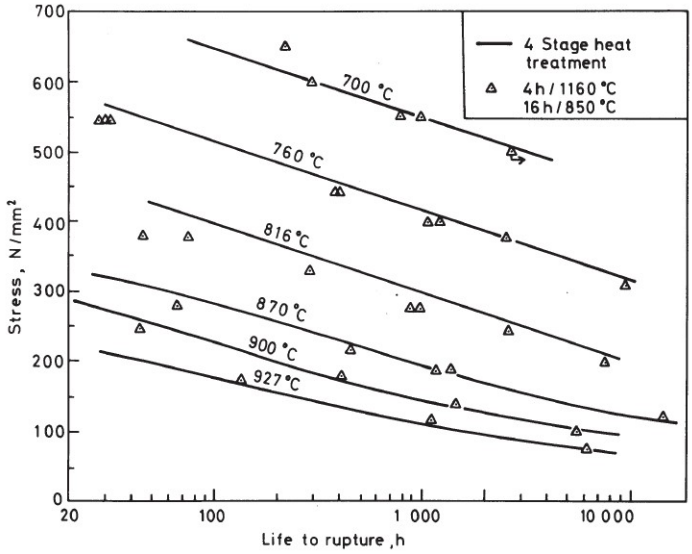

Figure 2.54: IN939 rupture propierties for two and four-stages heat treatments [73].

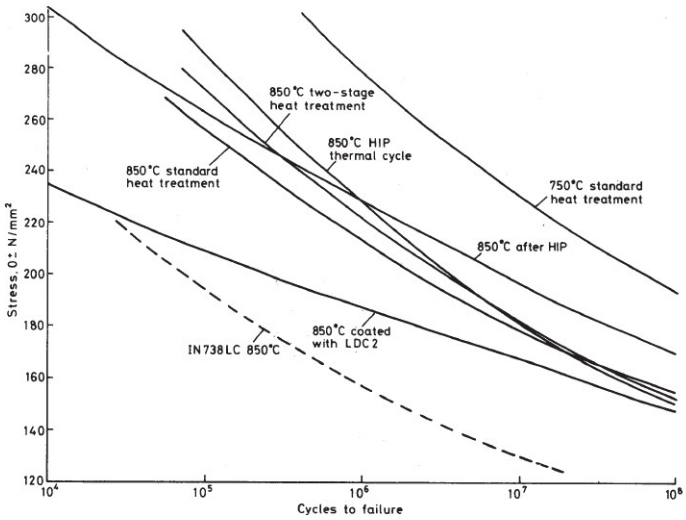

Figure 2.55: High cycle fatigue tests for differents heat treatments [73].

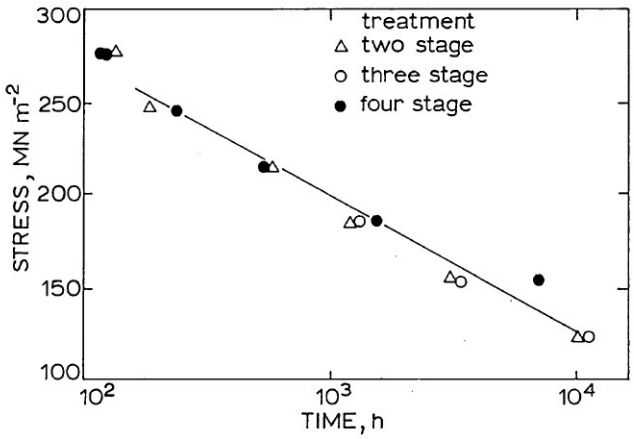

Figure 2.56: Creep propierties of IN939 at high temperatures for 2,3 and 4-stages heat treatments [74].

Table 2.24: Room temperatures tensile propierties of IN939 for differents heat treatments [74].

Treatment	0.2%PS	UTS	Elongation [%]	Reduction in area [%]
4 stages				
4h/1150°C+6h/1000°C +24h/900°C+16h/700°C	786	958	3.4	9
2 stages				
4h/1150°C+6h/850°C	823	861	2	0.6
4h/1150°C+6h/1000°C	651	974	9.2	13.5
3 stages				
4h/1150°C+6h/1000°C+24h/900°C	683	1007	7.1	8.5
4h/1150°C+6h/1000°C+16h/700°C	785	978	3.6	7
4h/1150°C+24h/900°C+16h/700°C	877	1027	1.5	5
4h/1160°C+6h/1000°C+16h/700°C	787	980	3.7	6
4h/1160°C+6h/1000°C+16h/800°C	815	986	3.3	6
4h/1160°C+6h/1000°C+16h/845°C	737	956	5.1	8
4h/1160°C+6h/1000°C+16h/850°C	687	1001	4.9	7
4h/1160°C+6h/1000°C+8h/800°C	813	1000	5.7	8.5
4h/1160°C+6h/1000°C+4h/800°C	826	1004	5.1	8.8
4h/1160°C+6h/1000°C+2h/800°C	799	979	5.1	7.7
4h/1160°C+6h/1000°C+1h/800°C	794	943	5.2	7.8
4h/1160°C+6h/1000°C+30min/800°C	755	934	6.3	15.6

Chapter 3

Materials and Methods

3.1 Printing of the specimens

the machine used for the realization of the specimens is the Print Sharp 250 from Prima Additive, shown in Fig.3.1, a medium volume machine suitable both for Additive Manufacturing services and for prototyping purposes. The technical specifications of the machine are summarized in Tab.3.1 [75].

Figure 3.1: Print Sharp 250 [75].

Table 3.1: Technical specifications of Print Sharp 250

Specification	Value
Volume [mm^3]	250x250x300
Max scanning speed [mm/s]	0.1
Laser power [W]	200-500

With this machine, the 28 specimens were made, each of them with specific process parameters, shown in Tab.3.2. The laser power and the layer thickness were kept constant, respectively at 395 W and 0.04 mm, while the scanning speed, the hatching distance and, consequently, the VED were varied.

Table 3.2: Proccess parameters of 28 specimens. The scanning speed has been made to vary from 1000 mm/s to 1600 mm/s, the hatching distance from 0.05 mm to 0.11 mm, constant the laser pwer and the thickness of the layer . Consequently, the VED ranges from 58 J/mm^3 to 198 J/mm^3.

n.	P [W]	t [mm]	v [mm/s]	h_d [mm]	VED [J/mm^3]
1	395	0,04	1000	0,05	198
2	395	0,04	1200	0,05	165
3	395	0,04	1400	0,05	141
4	395	0,04	1600	0,05	123
5	395	0,04	1000	0,06	165
6	395	0,04	1200	0,06	137
7	395	0,04	1400	0,06	118
8	395	0,04	1600	0,06	103
9	395	0,04	1000	0,07	141
10	395	0,04	1200	0,07	118
11	395	0,04	1400	0,07	101
12	395	0,04	1600	0,07	88
13	395	0,04	1000	0,08	123
14	395	0,04	1200	0,08	103
15	395	0,04	1400	0,08	88
16	395	0,04	1600	0,08	77
17	395	0,04	1000	0,09	110
18	395	0,04	1200	0,09	91
19	395	0,04	1400	0,09	78
20	395	0,04	1600	0,09	69
21	395	0,04	1000	0,1	99
22	395	0,04	1200	0,1	82
23	395	0,04	1400	0,1	71
24	395	0,04	1600	0,1	62
25	395	0,04	1000	0,11	90
26	395	0,04	1200	0,11	75
27	395	0,04	1400	0,11	64
28	395	0,04	1600	0,11	56

3.2 Metallographic preparation

One that the speciemens are printed, we proceed by cutting the specimens on the xz plane and xy plane, incorporating and polishing them (when it was necessary), and then performing the metallographic analyzes. The cutting machine Mecatome T210 (Fig. 3.2)is used for

the truncation of the samples. The polisher that was used for polishing is MECATECH 234 (Fig. 3.3). This operation is used to obtain, through the use of abrasive papers and then cloths, surfaces with a surface finish equal to 1 μm in order to obtain microscope images without incisions caused by the passage of the blade during truncation.
Before proceeding with the analysis, however, it was necessary to etch the specimens chemically with the Kalling's N.2 solution (hydrochloric acid + cupric chloride + 95% ethyl alcohol + distilled water), as polishing alone does not allow to visualize the shape and orientation of the grains, precipitates, and melt pools. This etching creates contrasts thanks to the reaction between the crystals and the solution: the light will reflect at different angles based on how the crystals have reacted, bringing to light the elements of our interest [76].

Figure 3.2: Cutting machine. Mecatome T210 [77].

Figure 3.3: Polisher MECATECH 234 [77].

3.3 Analysis on specimens

3.3.1 Optical microscope

The optical microscope used for metallographic analyzes is Leica DMI5000 M (Fig. 3.4). It is an inverted research microscope, which allowed us to obtain images of the samples at 100x, 200x and 500x magnifications and to acquire images using Leica LAS software.

Figure 3.4: Optical microscope Leica DMI5000 M [78].

3.3.2 Scanning Electon Microscopy (SEM)

The scanning electron microscope (SEM) allows to obtain images by means of the signals generated by the electron-sample iterations. The electrons, in fact, are accelerated by transporting kinetic energy which is transformed into signals when the incident electrons decelerate on the sample. Through this microscope it is possible to obtain data of different species of the sample, such as the chemical composition and the crystalline structure. A schematic of the SEM structure is shown in Fig. 3.5 [79].

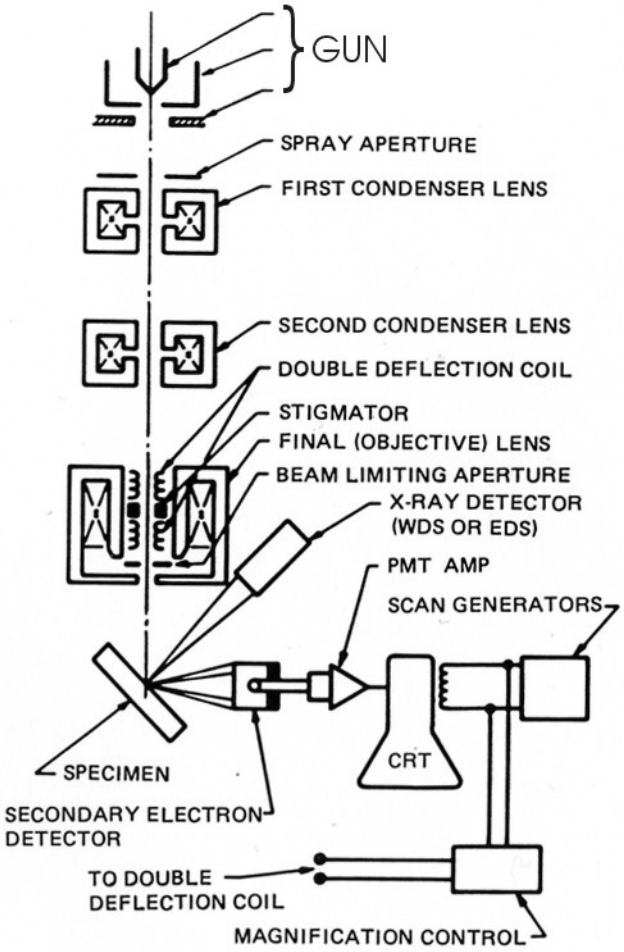

Figure 1.11. Schematic drawing of the electron and x-ray optics of a combined SEM–EPMA.

Figure 3.5: A Scheme of SEM [79].

3.4 Graphical analyis: ImageJ

ImageJ is an open source software, based on the Java language, image processing program designed for scientific multidimensional images [80].
For the study of porosity and defects of specimens, ten images at 100x magnification were then taken by the optical microscope for each sample, and post-processed and analyzed using ImageJ software. Contrast images are obtained from the optical microscope, where the black areas are those with no material, while the gray ones are the solid areas. The software, exploiting this contrast, calculates the porosity fraction of each image: the estimated porosity will be the average of the ten porosities calculated for each sample. The Fig. 3.6 shows the steps to process and analyze the images and, consequently, calculate the porosity of the specimen.

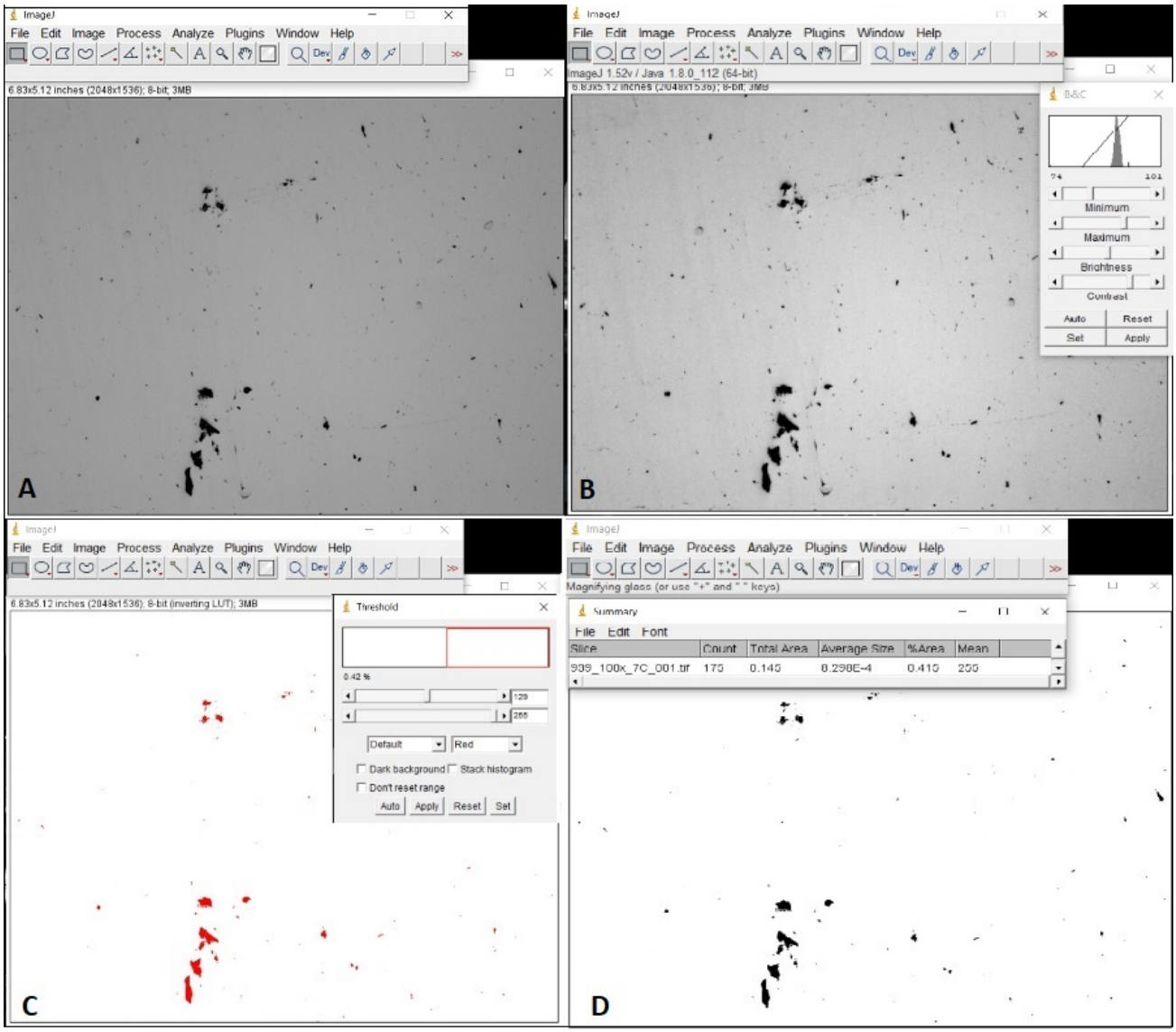

Figure 3.6: Steps to calculate the porosity with ImageJ. A)The image obtained under the optical miscroscope is inserted into the program, B)The contrast of the image is changed, C)The function Treshold is used, D)ImageJ calculates the porosity thanks to the contrast between empty (black) and full (white) zones.

3.5 Porosity with Archimedes Principle

Once that the speciemens are printed, a first calculation of porosity is made with Archimedes principle, to analyze the trend with the process parameters. The calculation of porosity with Archimedes, unlike others methods, takes into account the entire volume of the speciemen,

therefore it should provide results more reliable and global [81].
The Archimedes method calculates the porosity through the difference in bouyancy of the speciemen, weighed in the air and in the water. It is a fast, non-destructive and cheap method, as it provides the use of an analytical scale, shown in Fig.3.7,and a becker for distilled water. We performed six measurements for each speciemens, three in the air and three in the water, and, through excel sheet, it is was calculated the percentage of porosity of each speciemens. The matematical model behind the spreadsheets, the Archimedes principle, is explained below [82]:

$$\phi = 100 - \rho_{rel}, \tag{3.1}$$

$$\rho_{rel} = \frac{\rho_{Arch}}{\rho_{the} * 100}, \tag{3.2}$$

$$\rho_{Arch} = \frac{\rho_{H2O} * W_d}{W_d - W_w}, \tag{3.3}$$

where ϕ is density, ρ_{rel} is relative density, ρ_{Arch} is Archimedes density, ρ_{the} is theoretical density of the specieme (for IN 939 is equal to 8.15 g/cm^3), ρ_{H2O} is water density (equal to 0.9975 g/cm^3 at 25°C), W_d is weigh of speciemens in air, and W_w is weigh of speciemens in water.

Figure 3.7: Analytical scale used for calculating porosity of the speciemens.

3.6 Heat treatments

As previously explained, the IN939 alloy foresees 4 steps of thermal processes, for a total of 50h [73]. As you can guess, such a high total of hours requires very high time and costs.

It was then decided to subject the specimens to HIP, then solubilization, and, finally, two aging, for a total of 18 hours, all of heat treatments,except HIP treatment, are done into tubolar furnace. The conditions of the thermal processes are described in Tab. 3.3.
Through the images taken by the SEM and the optical microscope it was possible to analyze the microstructure of the specimens in each step of heat treatments. The specimens were then subjected to hardness test and x-ray diffraction analysis. The chapter ends with the comparison of different HIP conditions applied to specimens made with the same process parameters.

Table 3.3: Heat treatments condition

Heat treatment	Conditions
HIP	1210°C/160 MPa/4h + natual cooling
SOL	1160°C/4h
AG1	1000°C/6h
AG2	800°C/4h

3.7 Brinell Hardness test

The hardness of a material can be defined as its resistance to deformation under a constant pressure load. This shape change can be caused by indentation, scratches, wear, or bending. A specific type of test is the macro-indentation test, which measure the resistance of the material to penetration by means of a non-deformable spherical, conical or pyramidal indenter. The macro-indentation test can be of several types: Brinell, Meyer, Vickers, Rockwell, Shore Durometer, and the International Rubber Hardness Degree. It was decided to carry out the Brinell hardness test for the Inconel 939 specimens in each step of the thermal process. This test consists in indenting the material using a spherical-shaped indenter, with diameter D and load L, as shown in Fig. 3.9. The indenter will leave an imprint on the material with diameter d, visible with an optical microscope, through which it is possible to calculate the Brinell BHN hardness (or more commonly HB), with the following relationship [83]:

$$BHN = \frac{L}{A_c} = \frac{2L}{\pi D(D - \sqrt[2]{D^2 - d^2}} \tag{3.4}$$

Where: A_c is the area of the curved surface of the impression, L is the load, D is indenter's diameter and d is imprint's diameter.
When the footprint is not perfectly round, the value of d is calculated as the average of the two extreme diameters (the smallest and the largest), as follows:

$$d = \frac{d_1 + d_2}{2} \tag{3.5}$$

The parameters used for the test are shown in the Tab. 3.4.
Preliminarily, a force-diameter index is defined, which is calculated as:

$$B = \frac{0.102L}{D^2} \tag{3.6}$$

This index, obtainable through pre-filled tables, allows to keep the average diameter of the indentation between 0.24D and 0.6D and that hardness tests with different load and sphere diameter are directly comparable. The most common indices are 1, 2.5, 5, 10 and 30 [84]. Five sample measurements were carried out, four in the corners and one in the central area, the final hardness is calculated as the average of the five measurements.

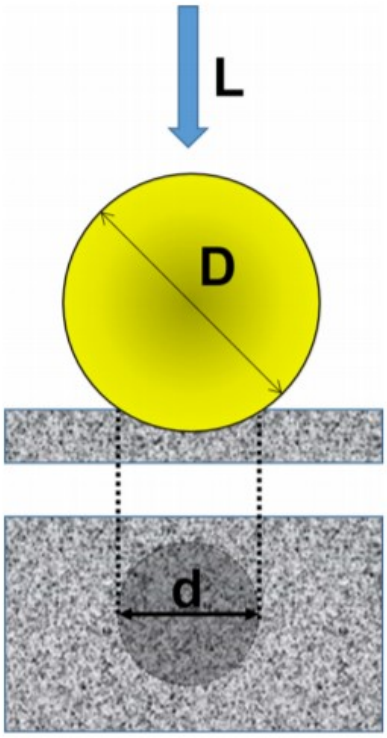

Figure 3.8: Brinell Test scheme [83].

Figure 3.9: Picture of Brinell Test. It is possible to see the indenter that impresses the load on the surface of the tested specimen.

Table 3.4: Parameters used for Brinell Hardness Test

Test Parameters	
Indenter Diameter [mm]	2.5
Load [Kg]	62.5
Force- diameter index	HB10

3.8 X-ray diffraction (XRD)

X-ray diffraction is a non-destructive (XRD) analytical technique used to identify and quantify phases in a material thanks the diffraction pattern that crystalline phase produces. Depending on the distortion of the diffraction peak, the XRD technique allows us to evaluate not only the phases present but also the residual stresses and the size of the grains. The residual compressive or tensile stresses, in fact, produce a displacement of the diffraction peak, while the small grains produce a widening of the peak. However, the widening of the diffraction peak can also be caused by defects in the material [85].
An example of the different phases and the corresponding XRD analyzes is shown in Fig. 3.10.

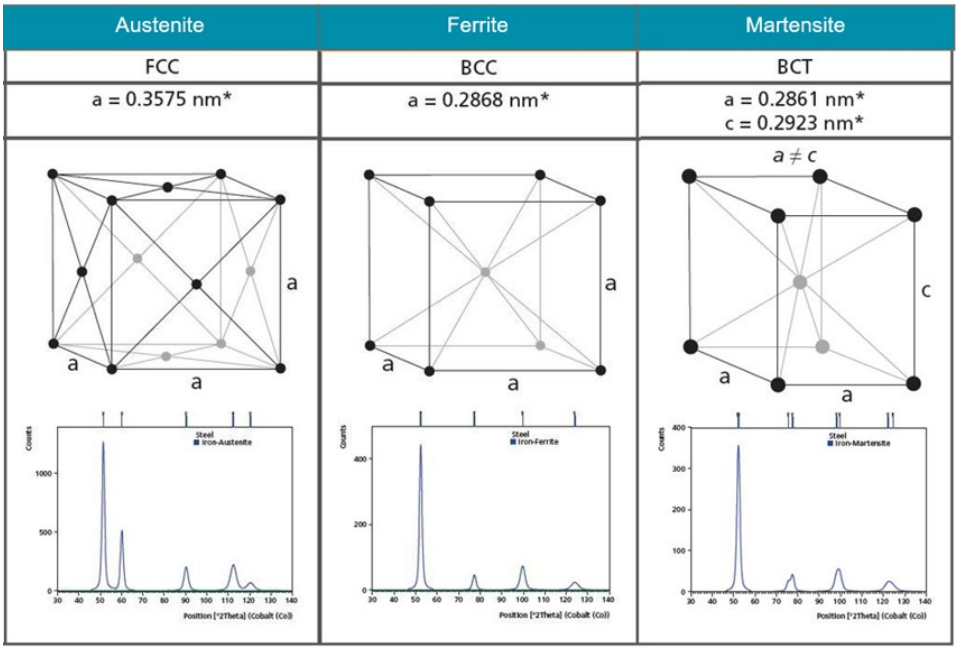

Figure 3.10: Austenite, Ferrite, and Martensite phases and the corresponding XRD [85].

Chapter 4

Optimization of process parameters

Tables 4.1 and 4.2 report the process parameters and the residual porosity of IN939 samples produced with a different combination of parameters, together with the volumetric energy density [J/mm^3] (VED)
From the literature, it is expected that as the VED increases the porosity will decrease up to a certain value. The main explanation is that a high VED promotes larger melting avoiding the presence of non melted areas [86, 56, 81].
However, if the VED is too high, it can create melt pool instability along with the formation of porosity as well as the formation of cracks.

Table 4.1: Results obtained with the Archimedes principle, compared with process parameters (laser power and layer thickness are constant).

n.	Porosity [%]	Dev.std	v [mm/s]	hd [mm]	VED [J/mm^3]
1	0,71	0,06	1000	0,05	198
2	0,29	0,10	1200	0,05	165
3	1,3	0,06	1400	0,05	141
4	0,63	0,08	1600	0,05	123
5	0,58	0,03	1000	0,06	165
6	0,87	0,02	1200	0,06	137
7	1,3	0,05	1400	0,06	118
8	1,88	0,04	1600	0,06	103
9	1,67	0,05	1000	0,07	141
10	2,03	0,05	1200	0,07	118
11	2,02	0,01	1400	0,07	101
12	2,12	0,01	1600	0,07	88
13	1,62	0,02	1000	0,08	123
14	1,01	0,01	1200	0,08	103
15	1	0,01	1400	0,08	88
16	1,18	0,01	1600	0,08	77
17	1,54	0,01	1000	0,09	110
18	1,85	0,01	1200	0,09	91
19	1,08	0,18	1400	0,09	78
20	1,03	0,01	1600	0,09	69
21	0,97	0,10	1000	0,1	99
22	0,85	0,02	1200	0,1	82
23	0,9	0,07	1400	0,1	71
24	1,78	0,01	1600	0,1	62
25	1,43	0,03	1000	0,11	90
26	0,99	0,03	1200	0,11	75
27	1,31	0,14	1400	0,11	64
28	2,79	0,01	1600	0,11	56

Table 4.2: Porosity obtained by image analysis (laser power and layer thickness are constant)

n.	Porosity [%]	Dev.std	v [mm/s]	hd [mm]	VED [J/mm^3]
1	0,2583	0,317298	1000	0,05	198
2	0,223	0,232038	1200	0,05	165
3	0,305	0,102758	1400	0,05	141
4	0,103	0,043249	1600	0,05	123
5	0,5155	0,501633	1000	0,06	165
6	0,2648	0,398446	1200	0,06	137
7	0,7132	0,331502	1400	0,06	118
8	0,5214	0,140487	1600	0,06	103
9	0,3522	0,094304	1000	0,07	141
10	0,1995	0,11136	1200	0,07	118
11	0,6572	0,644649	1400	0,07	101
12	0,3874	0,233574	1600	0,07	88
13	0,6718	0,650285	1000	0,08	123
14	0,3074	0,224004	1200	0,08	103
15	0,3162	0,216012	1400	0,08	88
16	0,7271	0,37554	1600	0,08	77
17	0,8606	0,427551	1000	0,09	110
18	0,7538	0,411306	1200	0,09	91
19	1,0707	0,546499	1400	0,09	78
20	0,1786	0,117062	1600	0,09	69
21	0,2666	0,078605	1000	0,1	99
22	0,3172	0,130265	1200	0,1	82
23	0,5025	0,181328	1400	0,1	71
24	0,5522	0,325399	1600	0,1	62
25	0,8787	0,524676	1000	0,11	90
26	0,2761	0,125073	1200	0,11	75
27	0,2443	0,190341	1400	0,11	64
28	1,1968	2,093608	1600	0,11	56

Figure 4.1 shows the porosity trend versus VED values.
In both graphs, as the VED increases, the density value increases. Starting from a value of 75 J/mm^3 the density of the material increases and it is possible to appreciate specimens that have porosity below 1%, and in particular, for ImageJ analysis, less than 0.5%. The two graphs in Fig. 4.1 give similar results, while for those obtained with the Archimedes principle, lower standard deviation as it considers the entire volume of the specimen, while for ImageJ higher error as it considers sections of the specimen where, especially for low VED, there are areas with very high density and others with irregular defects of large dimensions. However, the porosity calculation with ImageJ is more accurate also provides an overview of the shape,

size and number of pores.
It is possible to have the same VED for different process parameters, resulting in a different level of porosity. Therefore, the evaluation of porosity as a function of the VED is only an approximative optimization.
In fact, the same VED value can be obtained for different hatching distances and scanning speeds, which change the thermal history of the melting and the shape of the melt pools. For shorter hatching distances, in fact, the melt pools becomes narrower and deeper [87].
For this reason, the porosity trend with variable scanning speed and hatching distance was investigated, the results of which are shown in Fig. 4.2.
Below the porosity trend is presented for each hatching distance as the scanning speed varies:

- $h_d = 0.11$ mm. Porosity exhibits a very high value for low scanning speed, then tends to improve for intermediate speed values, and then rises again for high speeds.
- $h_d = 0.10$ mm. Porosity increases almost constantly with scanning speed.
- $h_d = 0.09$ mm. This trend exhibits the worst porosity values, probably because there is not enough overlap between one scan and another, for very high speeds the porosity sees a strong decrease, probably because the low-energy material is less subject to formation of defects.
- $h_d = 0.08$ mm. At low speed, the specimens have a fair amount of porosity, which, however, increases with increasing scanning speed.
- $h_d = 0.07$ mm. The trend is very similar to the case of hd = 0.08 mm, as low porosity values can be appreciated, which however worsens at high speed.
- $h_d = 0.06$ mm. At low speed the porosity remains contained, then sees a notable increase as the speed increases.
- $h_d = 0.05$ mm. The porosity is kept low and constant with the speed, to have a slight decrease at high speeds.

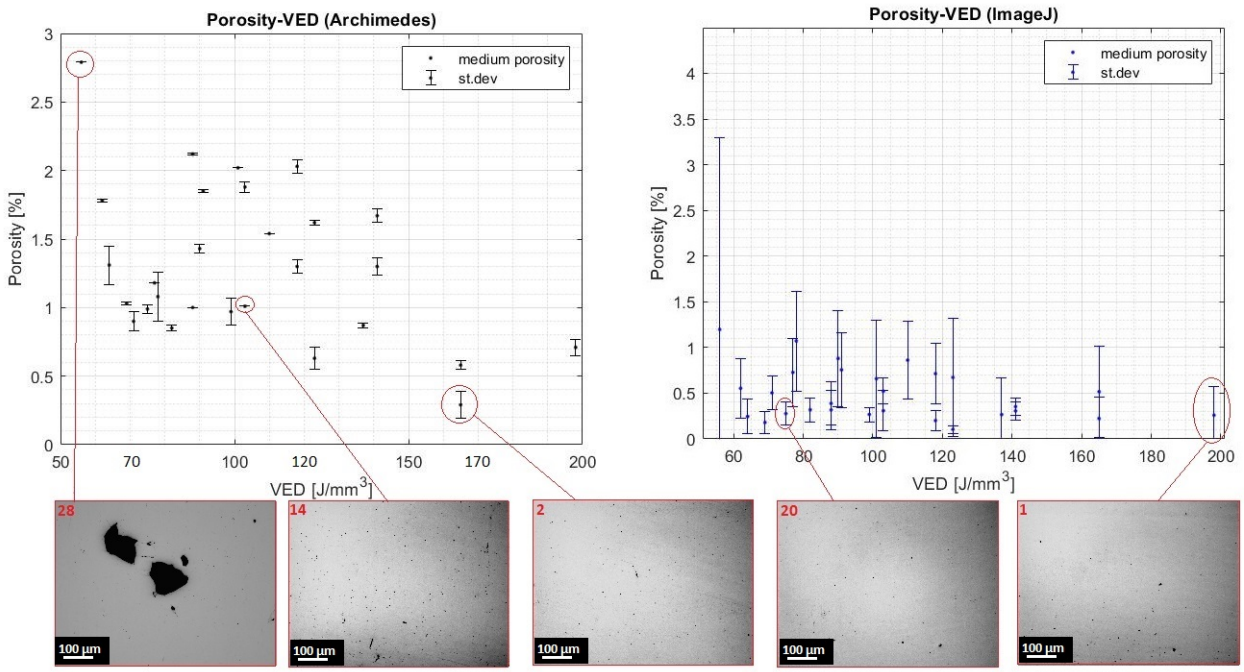

Figure 4.1: Trend porosity-VED, Archimedes method (left) and graphical analysis (right).

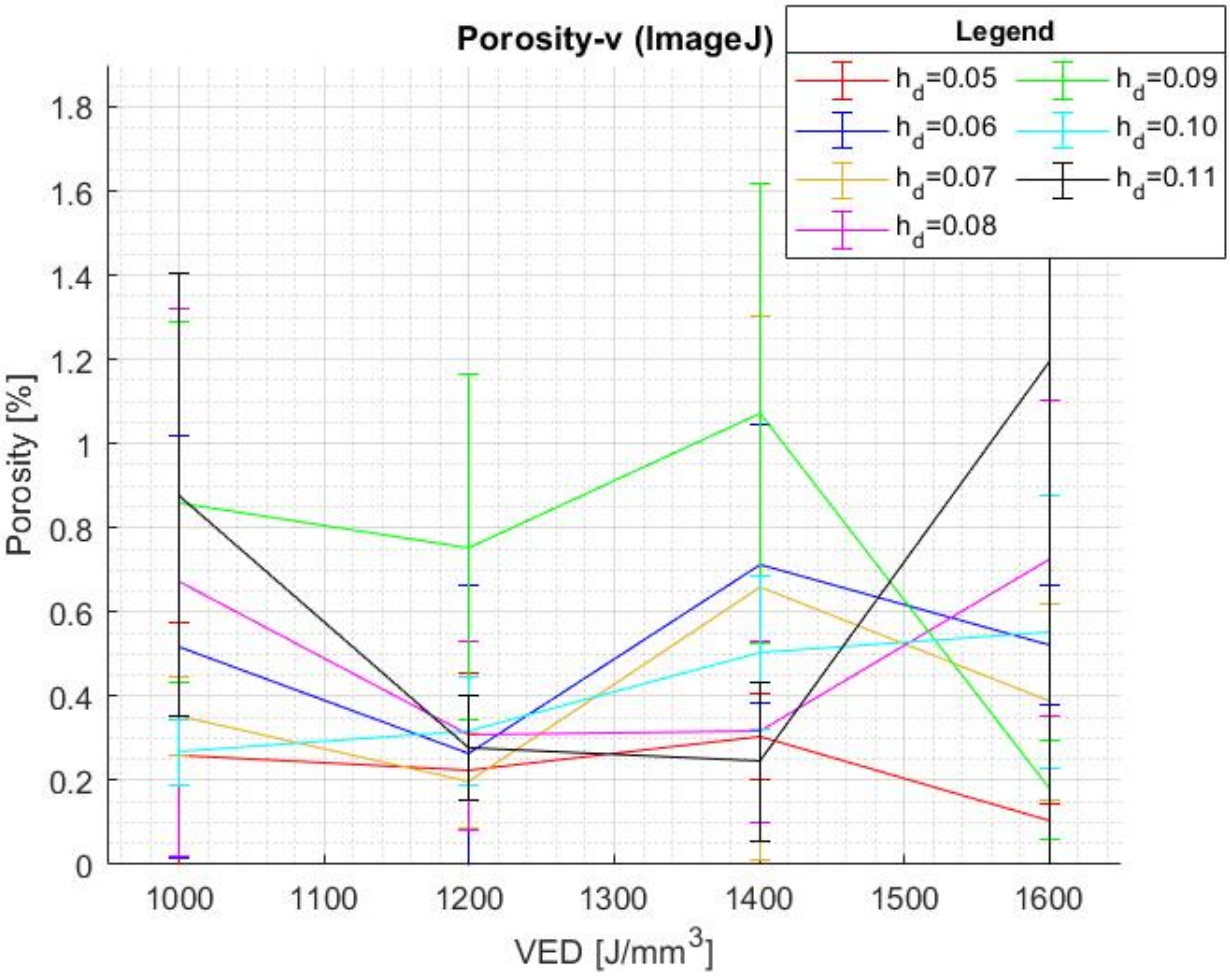

Figure 4.2: Trend porosity-scanning speed for each hatching distance, Archimedes method (up) and graphical analysis (down).

Once the optimized specimen was identified,that is the number 2, the pore shape of this was investigated to understand the nature of defect formation during the manufacturing process. There are two types of pores: regular, or spherical, and irregular in shape. The spherical pores mainly develop due to the trapping of gas during the atomization process, either present in the atmosphere or mixed with the powder, which does not have time to free itself from the melting pools before the metal solidifies. On the contrary, irregular pores develop due to nonoptimal process parameters, such as a too high scanning speed which causes the formation of irregular and open pores [88, 56]. Through the ImageJ software, it was possible to evaluate the circularity of the pores and their dimensions, through the Feret diameter, the distance between the two parallels tangent to the perimeter of the area projected by the particle. The circularity of the defects was then investigated by analyzing 10 images of the specimen, for a total area of 6.58 cm^2. Accordigly to what has been explained previously, if the circularity of

the pore tends to the unitary value, and therefore the defect is spherical, its formation does not depend on the process parameters which, therefore, are optimized.
The results are shown in Fig. 4.3 and in Fig. 4.4. From the first we can see that most of the defects have small dimensions, between 0 and 20 μm.

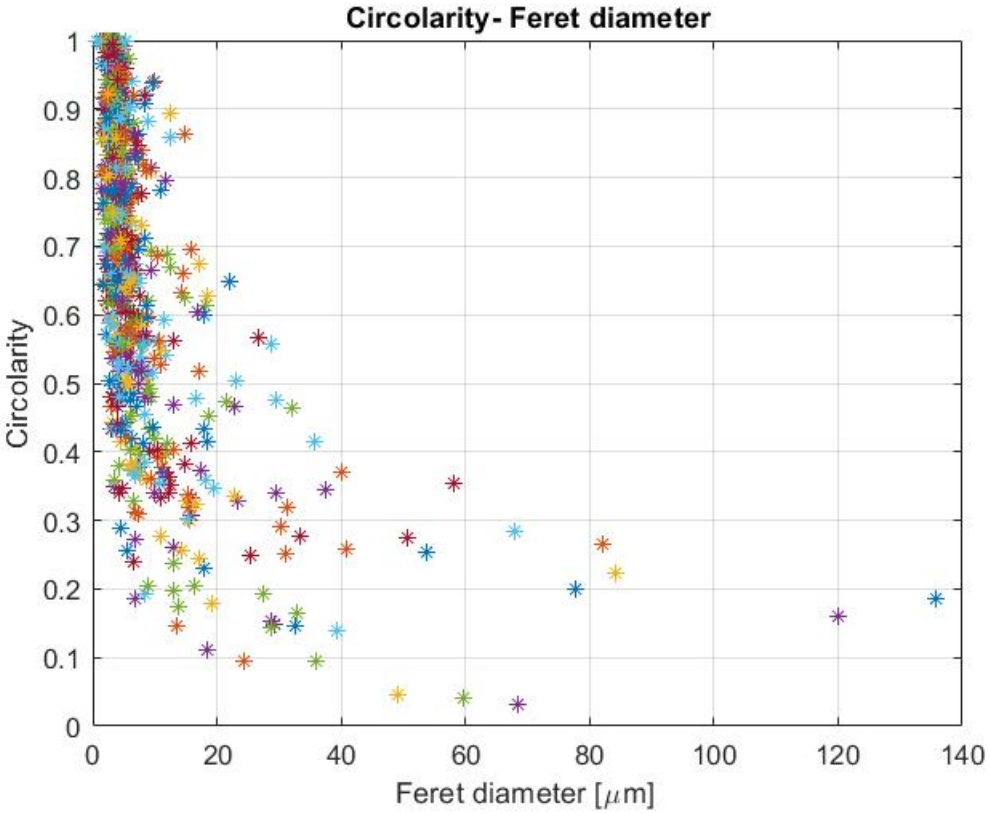

Figure 4.3: Circularity- Feret diameter of pores of specimen 2.

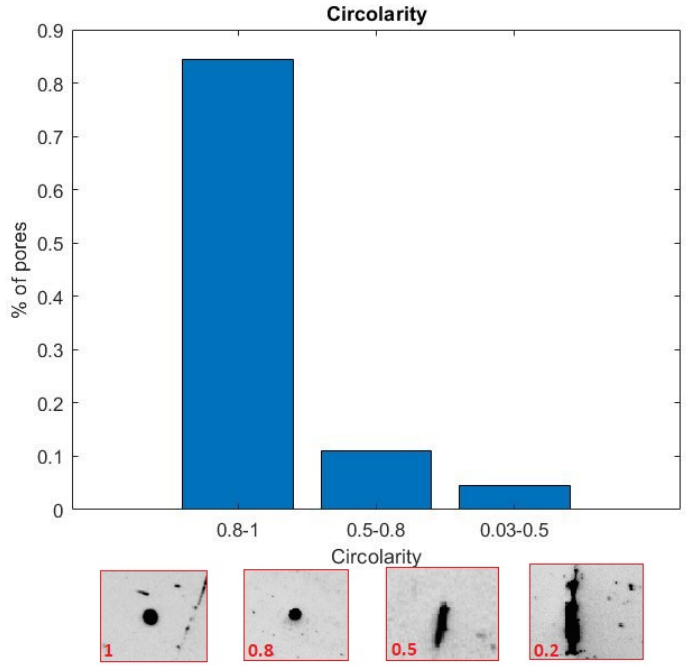

Figure 4.4: Numer of pores of specimen 2 divided according to circularity.

From the study carried out it was possible to identify the optimized process parameters. In particular, the best results are obtained for low hatching distance and scanning speed values, especially for v = 1200 mm/s, h_d = 0.05 mm, P = 395 W, l = 0.04 mm.

4.1 Analysis of As-built microstructure

The AB specimen (along z-plane) (Fig.4.5) presents cracks along the grain boundaries.
The chemical etchant makes visible the melt pool structures and the dendritic structures [89, 90]. Some melt pools, cracks and pores are highlighted in Fig.4.5.
Also xy-plane (Fig. 4.6) presents cracks along the grain boundaries, but since the grains are not columnar, they appear in a random position.
Under the SEM, the Energy Dispersion Spectrometry (EDS) analysis was made (Fig. 4.7). Thanks to the EDS analysis it was possible to qualitatively detect the elements present in the microstructure, and the corresponding wt. %, correspond to the values found in the literature.

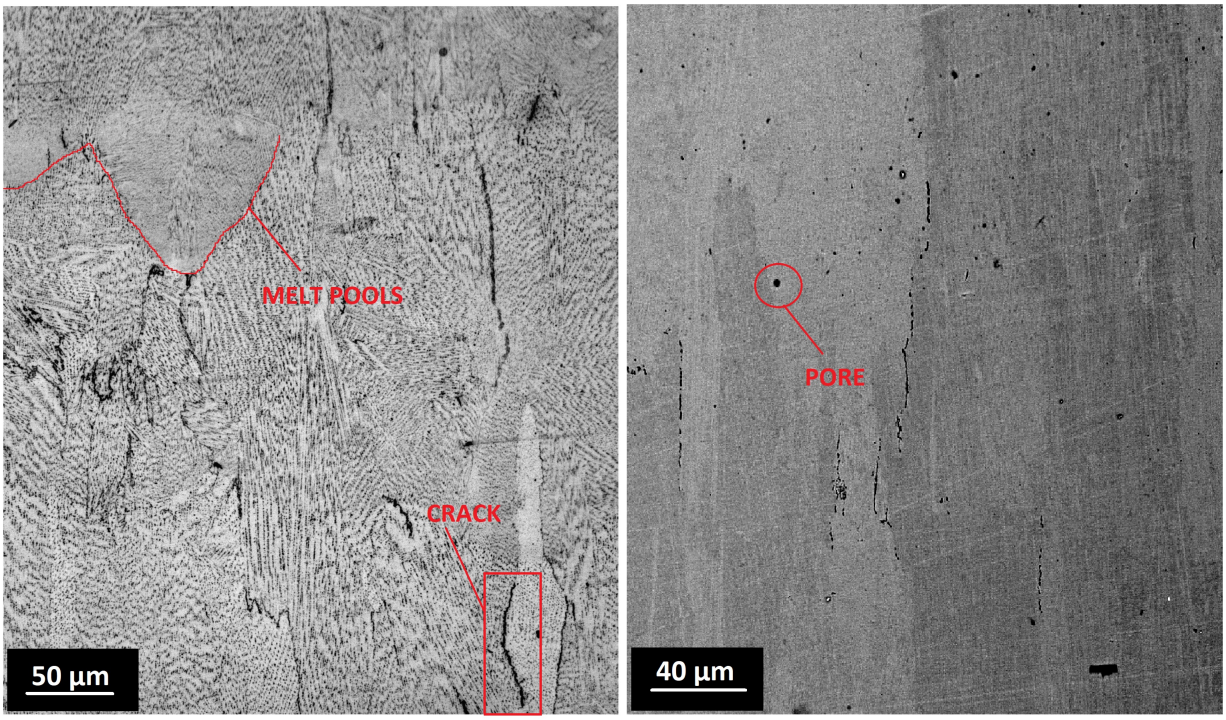

Figure 4.5: As-built specimen on z-plane. 100x(left) and 1000x (right).

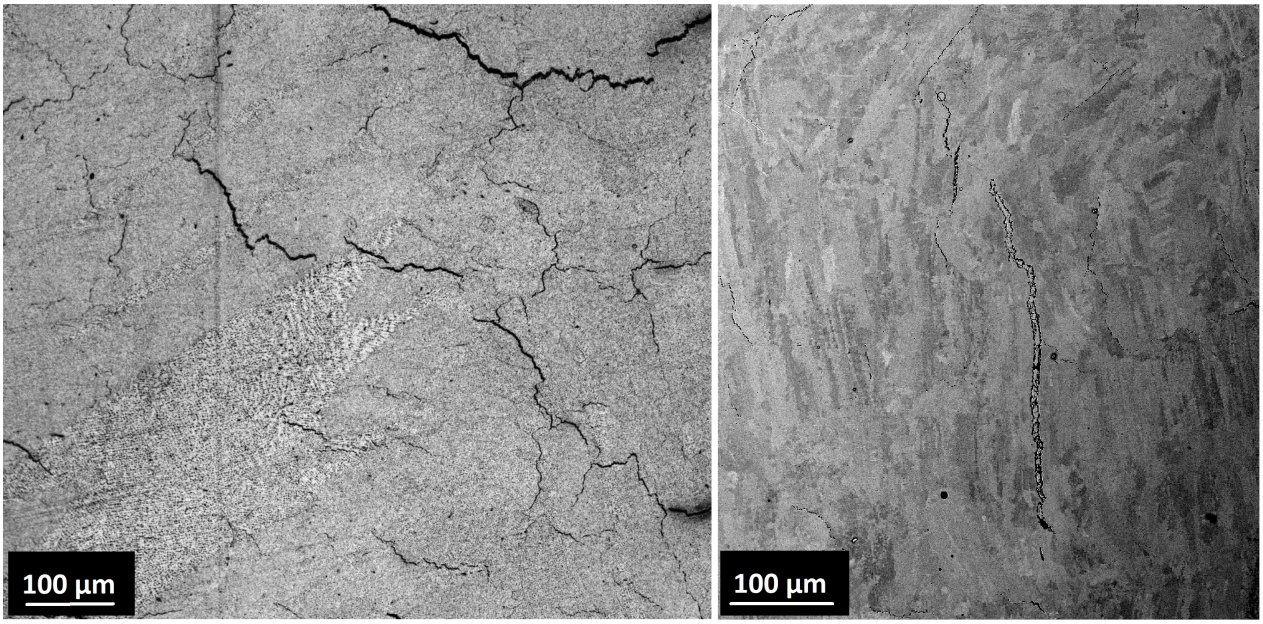

Figure 4.6: As-built specimen on xy-plane. 100x(left) and 500x (right).

Element Symbol	wt. % (EDS)	wt. % (Literature)
Ni	49.9	balance
Cr	21.8	22-23
Co	19.5	18-20
Ti	4.0	3-4.5
Al	2.3	1-3
Si	1.4	0-0.5
Nb	1.2	0.5-1.5

Figure 4.7: Energy Dispersion Spectrometry of as-built specimen.

Chapter 5

Analysis of thermal processes

This section analyzes the effect of the post-processing treatments applied on the IN939 specimens with porosity <0.2% fabricated by a Mlab Cusing R system.
On the samples were performed a HIP treatment followed by solutioning and ageing steps.
Each sample for each condition (HIP, HIP + SOL, HIP + SOL + AG1, HIP + SOL + AG2) was cut and polished and analyzed.
The following paragraphs concerns the analysis of the microstructure and hardness of the heat-treated samples.

5.1 Analysis of specimens microstructure

The evolution of the microstructure is analyzed for the heat-treated conditions.

5.1.1 HIP

After the HIP treatment, a partial recrystallization occurs and the grains tend to be less columnar. The melt pools disappear as well as the dendritic structures (Fig. 5.1). Form the images, the cracks seem consolidate and the fraction porosity is limited with value inferior to 0.1% after the HIP treatment.
From the images , it is also possible to observe black spots due to the formation of carbides generated during the HIP treatment and during the cooling.

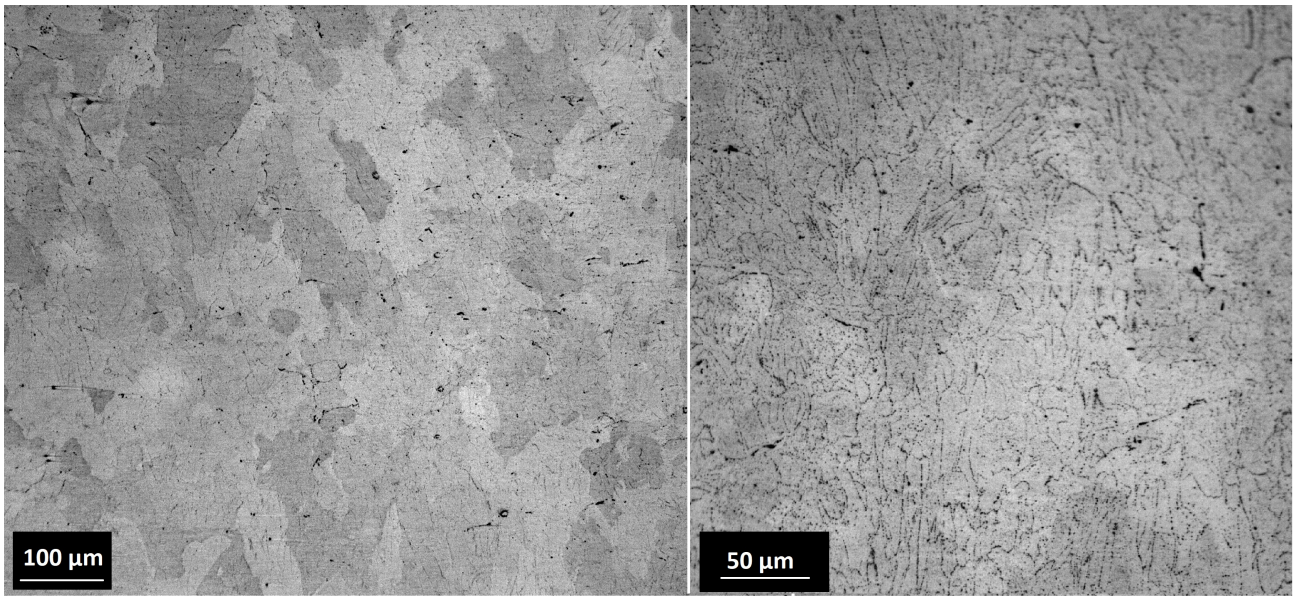

Figure 5.1: HIP specimen on z-plane. 100x(left) and 200x (right) after chemical etching.

At higher magnifications, as shown in Fig. 5.2, it is possible to notice the appearance of precipitated, especially at the grain boundary. Through graphic analysis it was possible to measure the size of some grains and the size of some carbides.
There are grains of average size of 114 μm and carbides of 0.35 μm which cover 0.644% of the total area considered.
The xy plane is not particularly different from the other plane (Fig. 5.3), this indicates that there has been a certain degree of recrystallization of the material. According to the literature, this translates into greater ductility of the material at the expense of yield strength and hardness [91]. However, as will be explained below, the formation of several large carbides results in increasing the hardness.
From the EDS analysis (Fig. 5.4), it can be seen how, it can be seen how, the carbides tend to be enriched in Ti and Nb and impoverished in Ni and Cr.

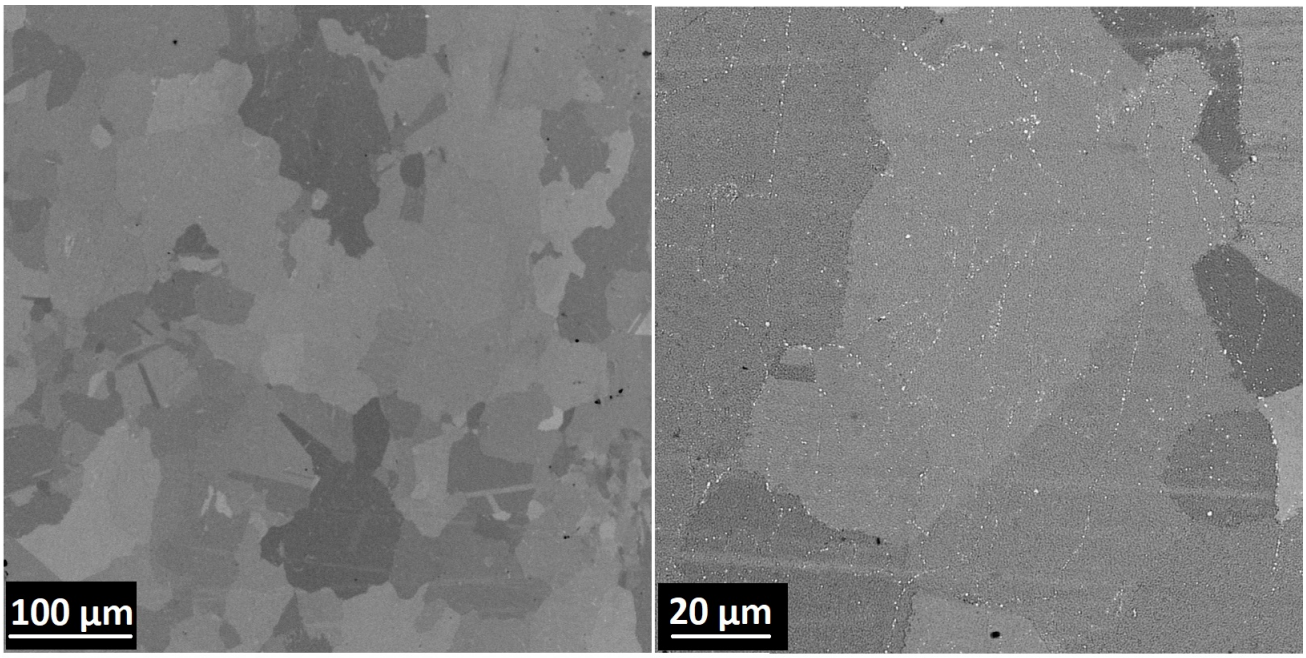

Figure 5.2: HIP specimen on z-plane. 500x(left) and 2000x (right).

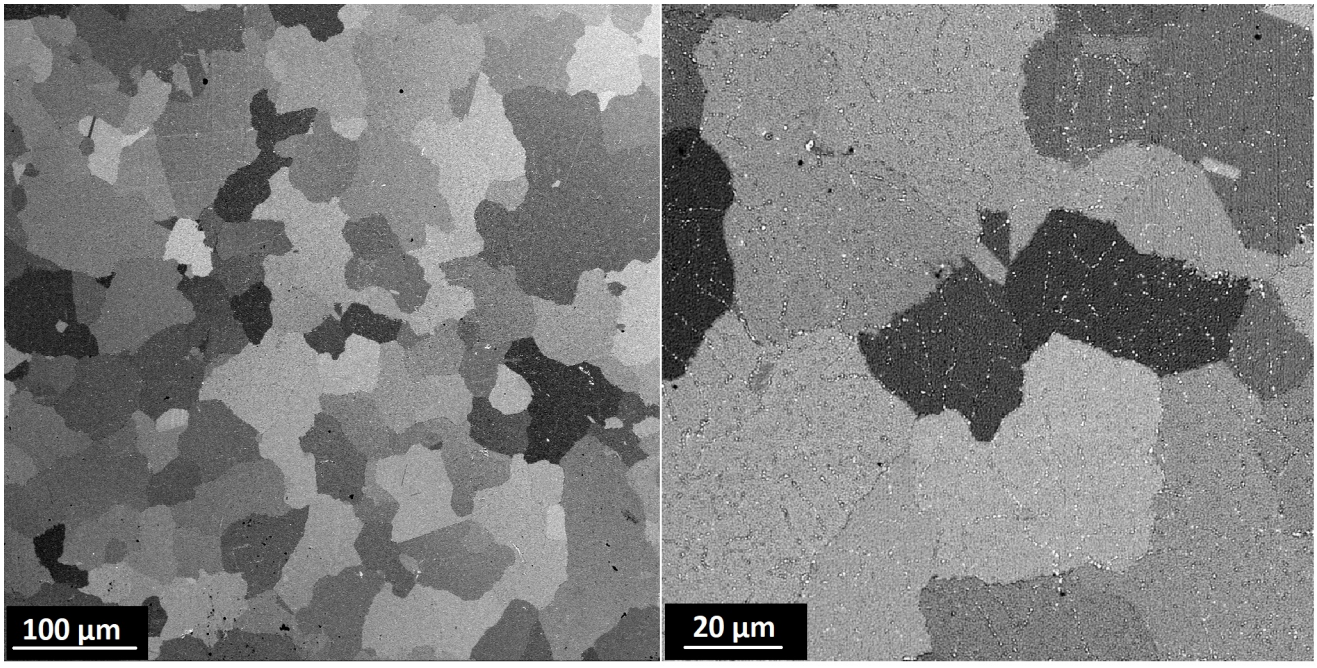

Figure 5.3: HIP specimen on xy-plane. 500x(left) and 2000x (right).

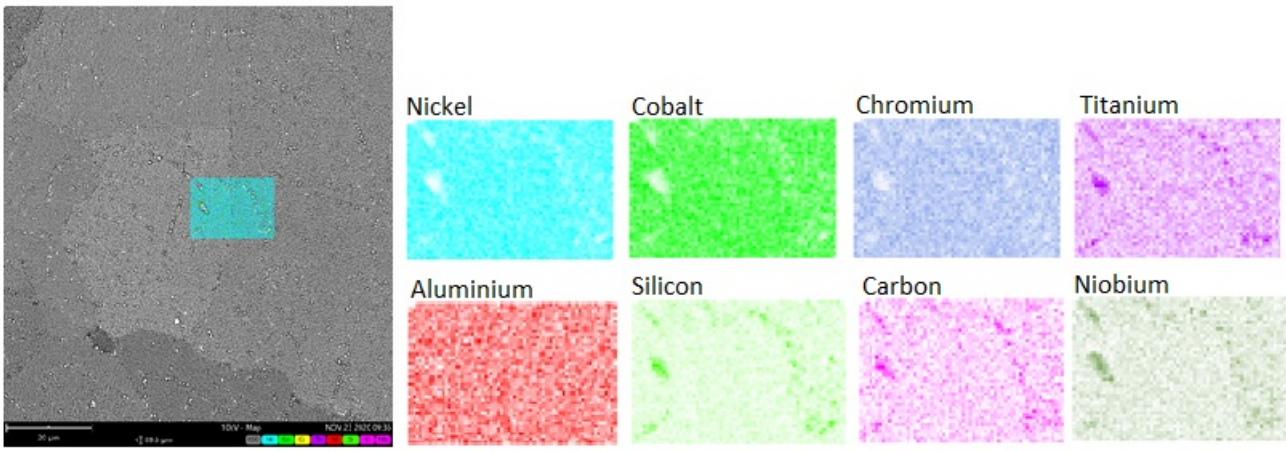

Figure 5.4: Energy Dispersion Spectrometry of specimen after HIP treatment.

Finally, a second HIP treatment was analyzed, which sees temperatures and pressures as the first but rapid cooling. The specimen, like the first HIP condition, sees partial recrystallization and presents precipitates concentrated especially at the grain boundary (Figs. 5.5 5.6). From the analysis conducted, it emerged that the average carbide size remains similar compared to the first condition of HIP, but % of these drops to 0.42%.

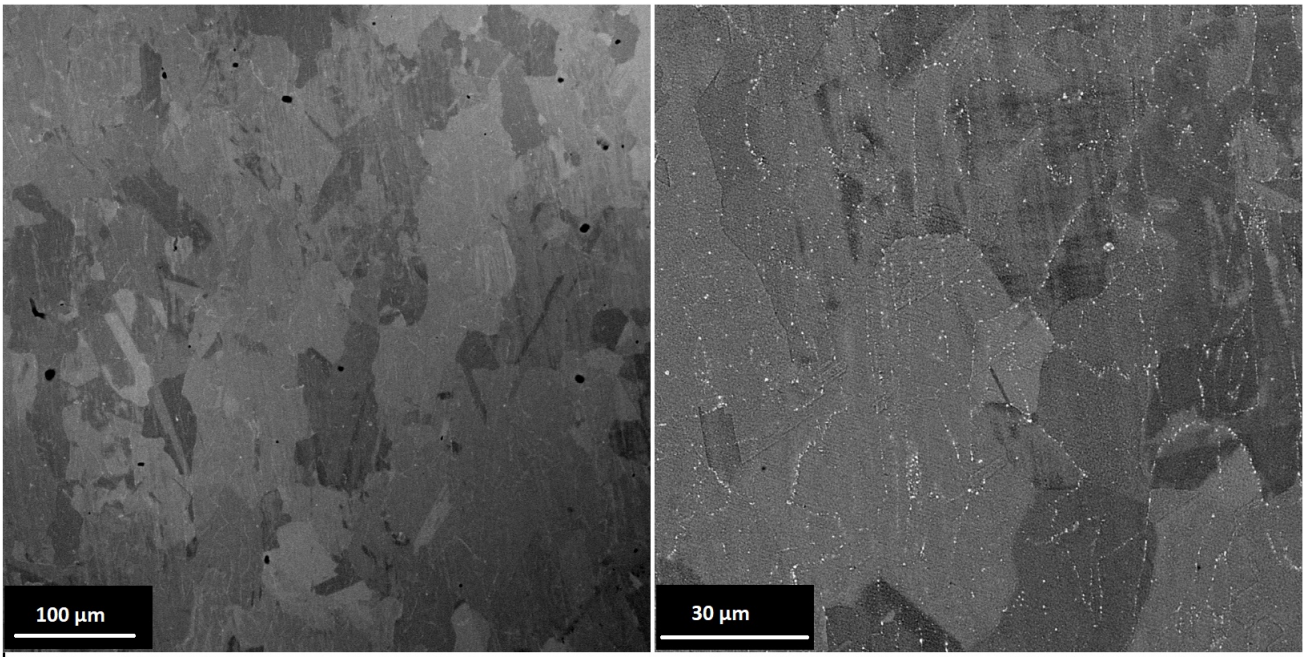

Figure 5.5: Second condition of HIP on z-plane. 500x(left) and 2000x (right).

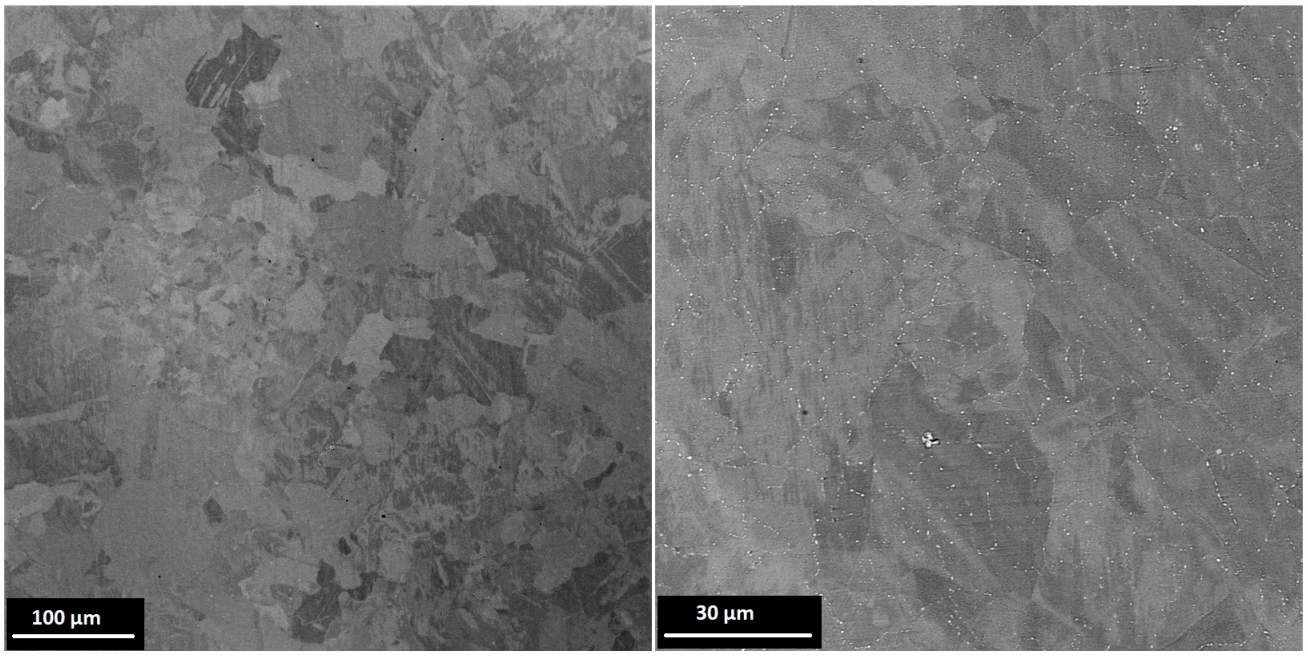

Figure 5.6: Second condition of HIP on xy-plane. 500x(left) and 2000x (right)

5.1.2 SOL

The solutioned sample (Figs. 5.7 and 5.8)shows the disappearance of a large fraction of carbides as, as expected from the literature, they are dissolved within the gamma austenitic matrix.
The solubilization has the purpose of eliminating the carbides. However, a part of carbides remained after the solubilization.
A partial solubilization of the carbides was therefore obtained, as also demonstrated by the EDS analysis (Fig. 5.9). Furthermore, considering that the slow cooling following the HIP has formed, in addition to the carbides, the gamma prime phase, solubilization has made it possible to dissolve this phase, to regain it with controlled shape and size with the two aging treatments.
Following solubilization, the material has grains with dimensions similar to the HIPed condition, and % of carbides reduced to 0.486% with a medium dimensions of around 0.3 μm.

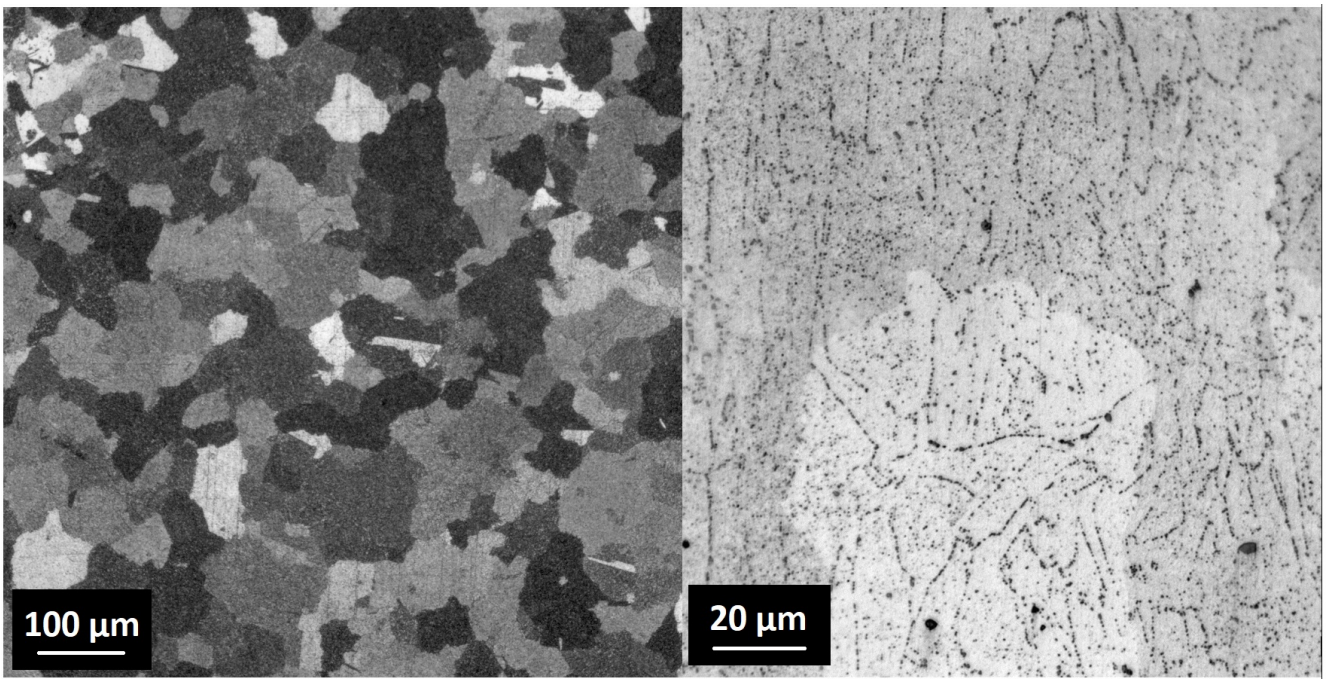

Figure 5.7: SOL specimen on z-plane. 100x (right) and 200x (left).

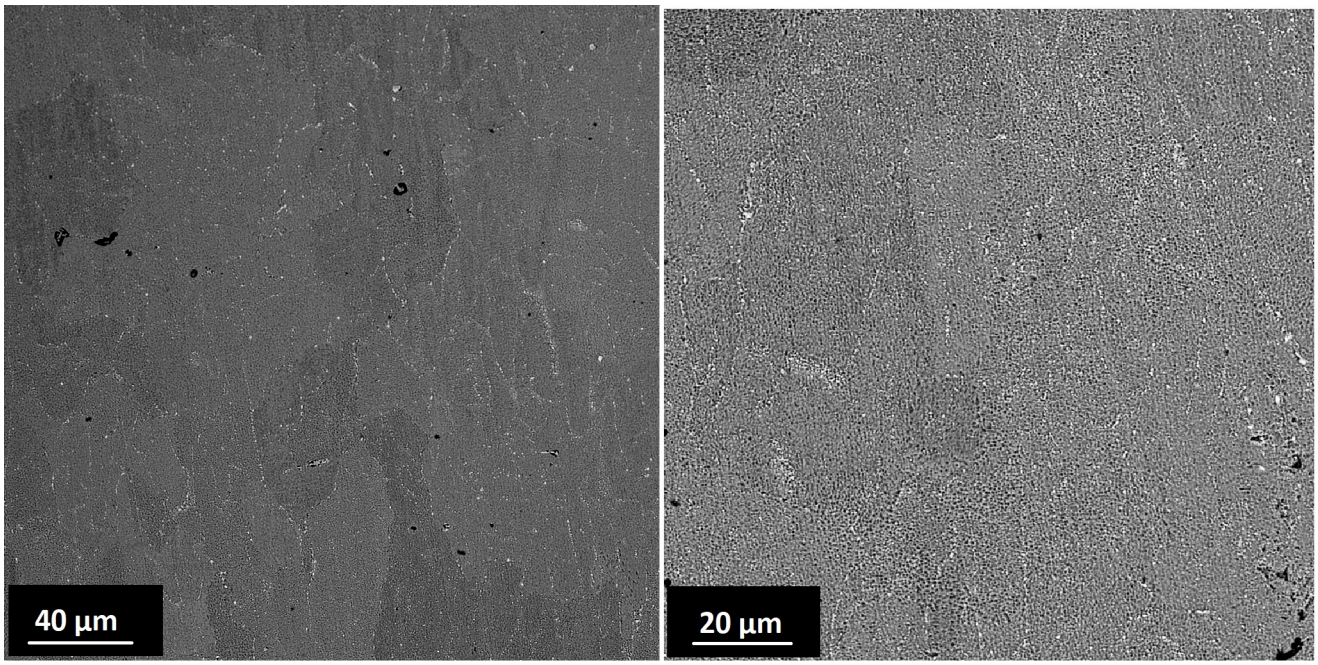

Figure 5.8: SOL specimen on z-plane. 1000x (right) and 2000x (left).

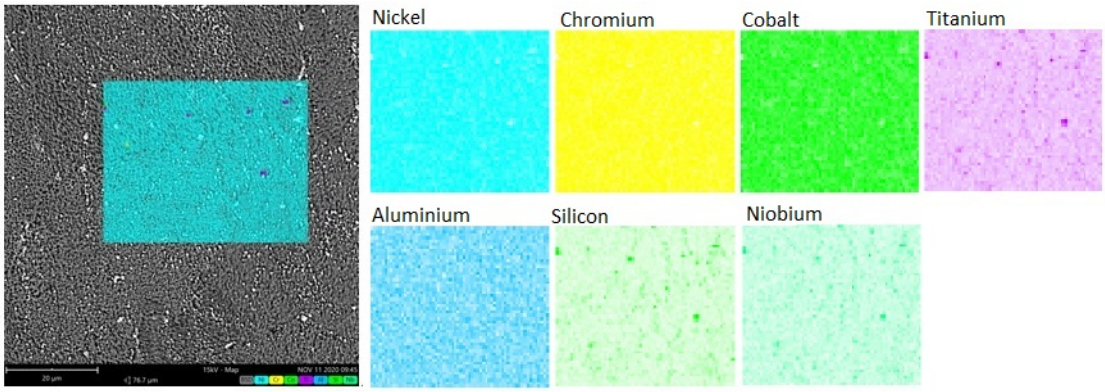

Figure 5.9: Energy Dispersion Spectrometry of specimen after solutioning treatment.

5.1.3 AG1+AG2

The two aging treatments made it possible to reform the gamma prime phase, previously eliminated through solubilization, in a controlled manner. The grain structures did not undergo to particular modifications (Figs. 5.10 and 5.11).
This was expected since the temperatures are inferior with respect to the solutioning condition.
However, the heat treatment promote the formation of gamma prime phases with fine dimensions (Fig. 5.12) .

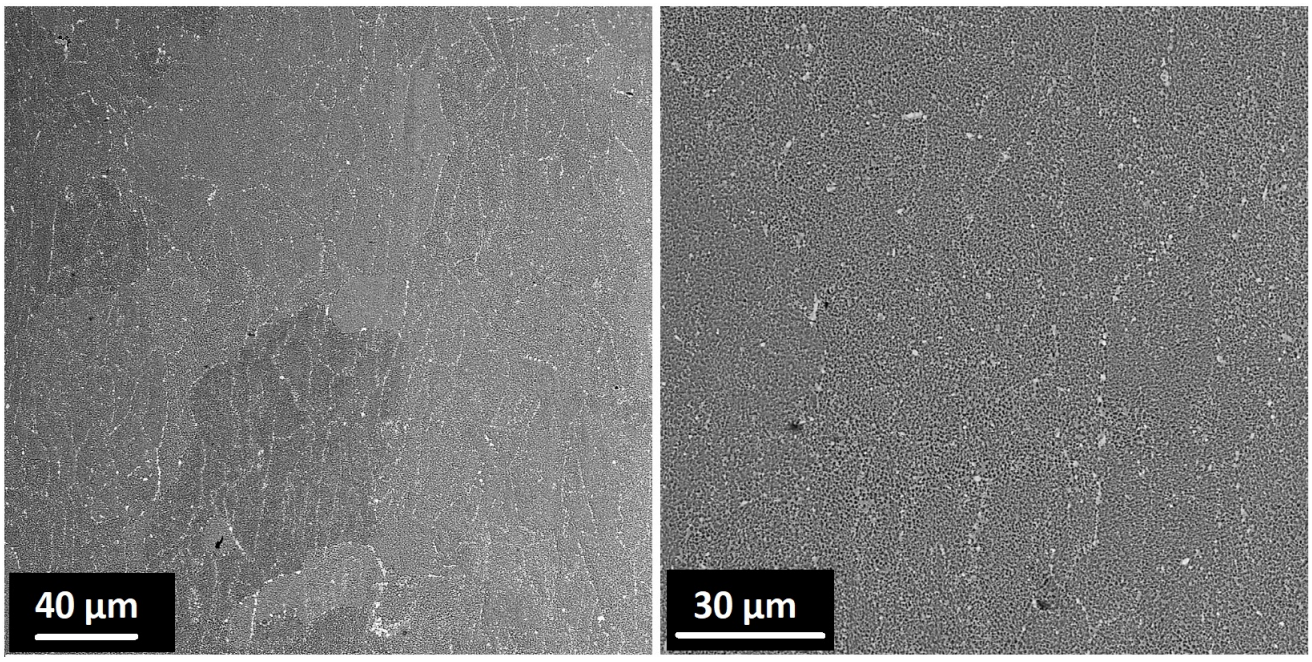

Figure 5.10: Ag1 specimen on z-plane. 1000x (right) and 200x (left).

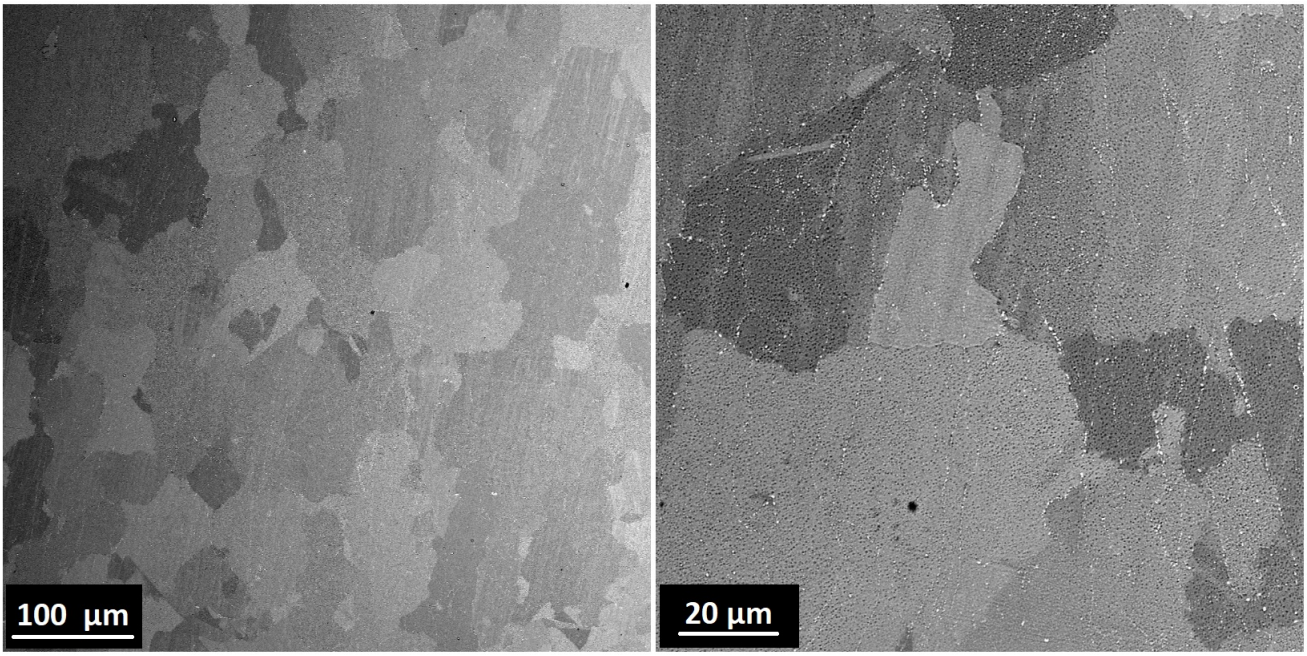

Figure 5.11: AG2 specimen on z-plane. 500x (right) and 2000x (left).

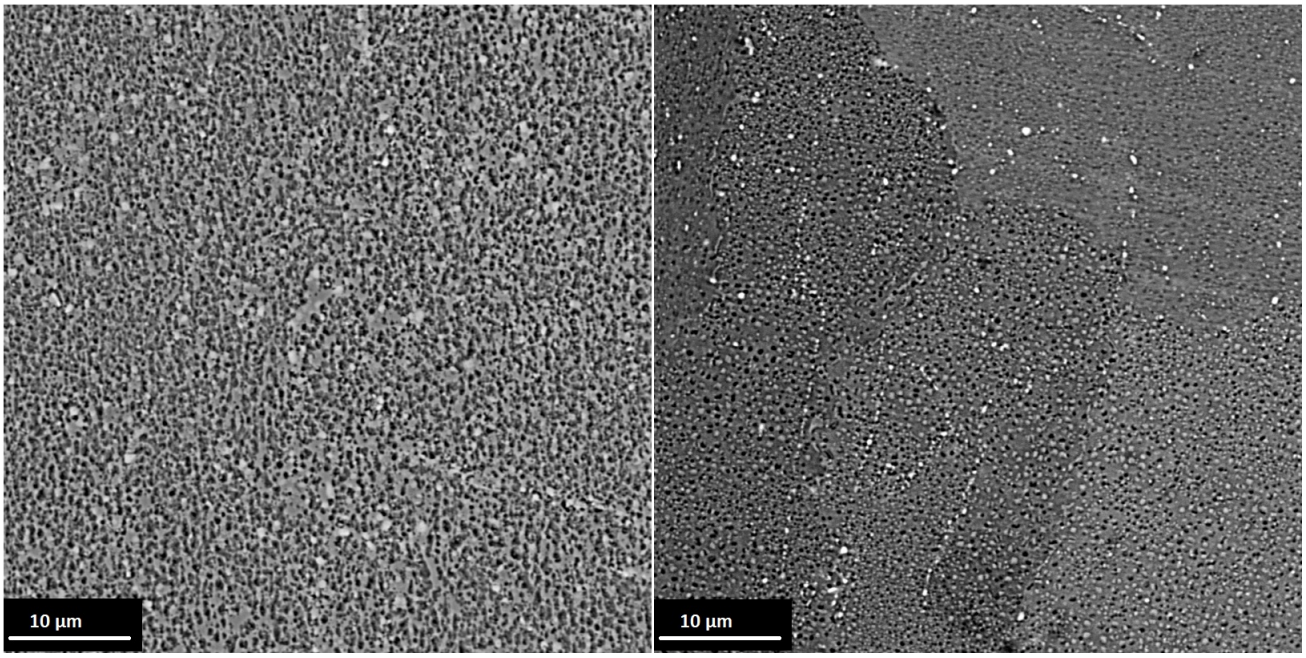

Figure 5.12: Ag1 and Ag2 specimens at 5000x. Ag1 (left) and Ag2 (right).

5.2 Brinell Hardness

The results obtained from Brinell test are shown in Tab. 5.1 and the trend in Fig. 5.13.
The hardness value already in the As-built condition is high, thanks to the dendritic structures that increase the hardness of the material. This value tends to increase after HIP, despite the dendritic structures having been eliminated. However, the formation of the large carbides results in a strong hardening of the specimen.
On the contrary, the solutioning partially dissolves the carbides into a solid solution reducing the hardness. After the two aging treatments, the hardness tends to reach a maximum value due to the formation of gamma prime phases. Finally, it is possible to appreciate how the standard deviation, and therefore the error, is very low, indicating that the specimens are homogeneous.

Table 5.1: Brinell Hardness Test Results

	1	2	3	4	5	Dev.Std.	Medium
AB	268	263	258	269	258	5	263.2
HIP	362	361	362	353	345	8	356.6
HIP+SOL	323	321	325	326	319	3	322.8
HIP+SOL+AG1	327	337	326	329	326	5	329
HIP+AG2	373	377	377	373	380	3	376

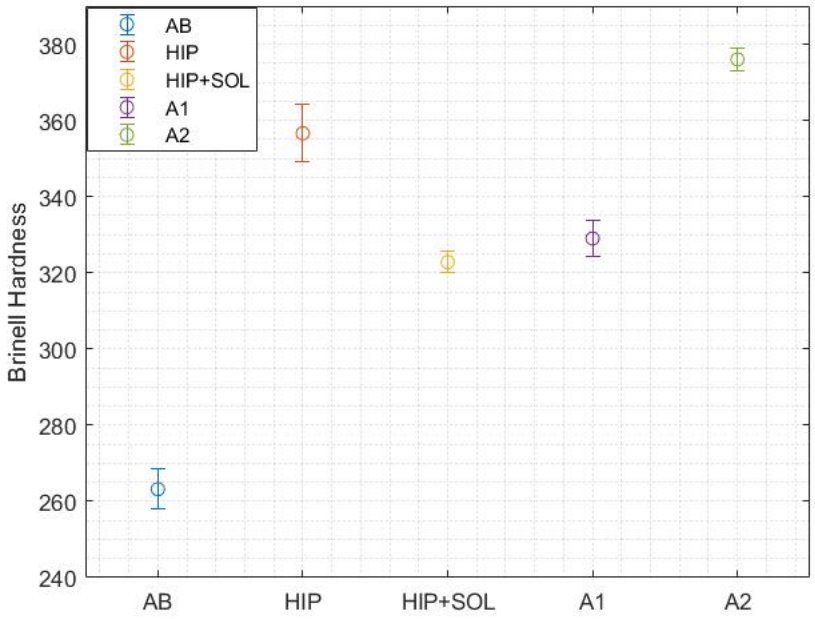

Figure 5.13: Trend of Brinell Hardness test in each step of heat treatments.

5.3 XRD

The XRD (Fig. 5.14) shows the peaks of the austenitic gamma matrix for the different conditions. The peak (111) is around 42-43°, the peak (200) around 51°, the peak (220) around 75° and the peak (311) around 91°.
Typically, for the Ni-based superalloys, the peak (111) should present higher intensity than the peak (200), or they should be close each other. This is consistent with all the heat-treated samples.
On the other hand, the as-built samples present higher intensity for the peak (200) than (111), indicating a strong texture compatible with the application of the LPBF process.
Moreover, the heat-treated samples show a peak around 35° that can be associated with the formation of carbides, as highlighted by the SEM images.

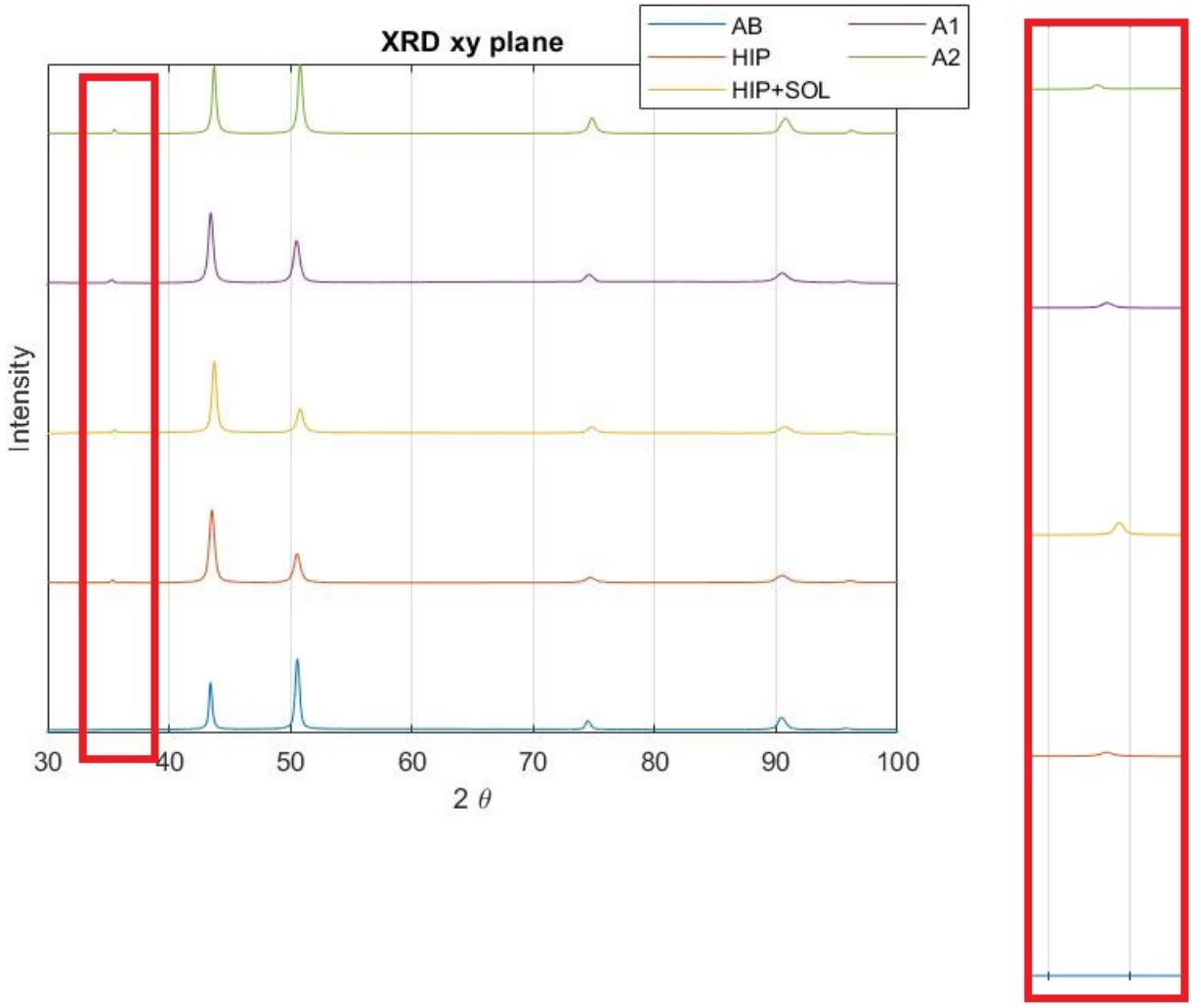

Figure 5.14: X-ray diffraction of LPBF samples of IN939 in the as-built and heat-treated conditions along the xy plane.

Chapter 6

Conclusions

The thesis work is based on the study of the superalloy in Nickel Inconel 939, processed through Laser Powder Bed Fusion.
The first part deals with the optimization of process parameters for the Print Sharp 250 machine, maintaining constant power and layer thickness and varying hatching distance and scanning speed. The analysis conducted showed the trend of the residual porosity as a function of the process parameters, first qualitatively with the VED and subsequently with the scanning speed and the hatching distance. The study showed that for low hatching distance, equal to 0.05 mm, and scanning speed values of 1200 mm/s, reaching porosity below 0.2%. The chemical attack on the as-built samples highlighted the presence of cracks along the grain boundaries.
The second part deals with the study of thermal processes applied on samples made with the Mlab Cusing R system machine, with process parameters optimized by a previous study. The samples were subjected to Hot isostatic pressing, solubilization and two aging treatments. The microstructural analysis shows that the HIP treatment has eliminated cracks, melt pools and dendritic structures, the grains lose their columnar shape thanks to a partial recrystallization and the porosity drops below 0.1%. It can be seen, thanks to EDS analysis, the formation of carbides, large precipitates concentrated above all on the grain boundaries. The solubilization allowed, however, to reduce the concentration of carbides from 0.64 to 0.48% and to eliminate the gamma prime phases, which may be formed during the slow cooling following the HIP. Finally, with the two aging treatments, the gamma prime phase were formed with the correct size.
The Brinell hardness tests have shown that already from the as-built condition the material has a high hardness of 263 HB, due to the presence of the dendritic structures, and reaches a value of HB 376 following the two aging.
Given the excellent performance shown by the material following heat treatments, which are interesting for turbine blades, a future development could analyze the mechanical characteristics of this material following heat treatments, such as fatigue tests at high temperatures, essential for the use of the material for the production of turbine blades.

Bibliography

[1] William E Frazier. Metal additive manufacturing: a review. *Journal of Materials Engineering and performance*, 23(6):1917–1928, 2014.

[2] M Shellabear and O Nyrhilä. Dmls-development history and state of the art. *Laser Assisted Netshape engineering 4, proceedings of the 4th LANE*, pages 21–24, 2004.

[3] Eos- additive manufacturing solutions.

[4] Mohsen Attaran. The rise of 3-d printing: The advantages of additive manufacturing over traditional manufacturing. *Business Horizons*, 60(5):677–688, 2017.

[5] Richard E. Crandall. Where will additive manufacturing take us?

[6] Mary Kathryn Thompson, Giovanni Moroni, Tom Vaneker, Georges Fadel, R Ian Campbell, Ian Gibson, Alain Bernard, Joachim Schulz, Patricia Graf, Bhrigu Ahuja, et al. Design for additive manufacturing: Trends, opportunities, considerations, and constraints. *CIRP annals*, 65(2):737–760, 2016.

[7] PADT. 3d printing glossary.

[8] Ruth Jiang, Robin Kleer, and Frank T Piller. Predicting the future of additive manufacturing: A delphi study on economic and societal implications of 3d printing for 2030. *Technological Forecasting and Social Change*, 117:84–97, 2017.

[9] Wei Gao, Yunbo Zhang, Devarajan Ramanujan, Karthik Ramani, Yong Chen, Christopher B Williams, Charlie CL Wang, Yung C Shin, Song Zhang, and Pablo D Zavattieri. The status, challenges, and future of additive manufacturing in engineering. *Computer-Aided Design*, 69:65–89, 2015.

[10] M Sugavaneswaran and G Arumaikkannu. Modelling for randomly oriented multi material additive manufacturing component and its fabrication. *Materials & Design (1980-2015)*, 54:779–785, 2014.

[11] SmartTech Analysis. Multilaser additive manufacturing – an end user perspective.

[12] Joel C Najmon, Sajjad Raeisi, and Andres Tovar. Review of additive manufacturing technologies and applications in the aerospace industry. pages 7–31, 2019.

[13] Sushant Negi, Suresh Dhiman, and Rajesh Kumar Sharma. Basics, applications and future of additive manufacturing technologies: A review. *Journal of Manufacturing Technology Research*, 5(1/2):75, 2013.

[14] Thomas Duda and L Venkat Raghavan. 3d metal printing technology. *IFAC-PapersOnLine*, 49(29):103–110, 2016.

[15] Direct energy deposition (ded).

[16] Adrita Dass and Atieh Moridi. State of the art in directed energy deposition: From additive manufacturing to materials design. *Coatings*, 9(7):418, 2019.

[17] Paul R Gradl, Christopher S Protz, Kevin Zagorski, Vishal Doshi, and Hannah McCallum. Additive manufacturing and hot-fire testing of bimetallic grcop-84 and c-18150 channel-cooled combustion chambers using powder bed fusion and inconel 625 hybrid directed energy deposition. page 4390, 2019.

[18] Abdollah Saboori, Alberta Aversa, Giulio Marchese, Sara Biamino, Mariangela Lombardi, and Paolo Fino. Application of directed energy deposition-based additive manufacturing in repair. *Applied Sciences*, 9(16):3316, 2019.

[19] Saad A Khairallah, Andrew T Anderson, Alexander Rubenchik, and Wayne E King. Laser powder-bed fusion additive manufacturing: Physics of complex melt flow and formation mechanisms of pores, spatter, and denudation zones. *Acta Materialia*, 108:36–45, 2016.

[20] Alexander Katz-Demyanetz, Vladimir V Popov Jr, Aleksey Kovalevsky, Daniel Safranchik, and Andrei Koptioug. Powder-bed additive manufacturing for aerospace application: Techniques, metallic and metal/ceramic composite materials and trends. *Manufacturing Review*, 6, 2019.

[21] Materiali innovativi nella stampa 3d. *Progetto NANOCOAT*.

[22] LE Murr. Metallurgy of additive manufacturing: Examples from electron beam melting. *Additive Manufacturing*, 5:40–53, 2015.

[23] Lorenzo Dall'Ava, Harry Hothi, Anna Di Laura, Johann Henckel, and Alister Hart. 3d printed acetabular cups for total hip arthroplasty: a review article. *Metals*, 9(7):729, 2019.

[24] Michael Molitch-Hou. Rolls-royce flies largest 3d printed part ever flown.

[25] Chor Yen Yap, Chee Kai Chua, Zhi Li Dong, Zhong Hong Liu, Dan Qing Zhang, Loong Ee Loh, and Swee Leong Sing. Review of selective laser melting: Materials and applications. *Applied physics reviews*, 2(4):041101, 2015.

[26] Xin Liu, Mhamed Boutaous, Shihe Xin, and Dennis Siginer. Numerical simulation of balling phenomenon in metallic laser melting process. 50336:V002T22A003, 2016.

[27] Michael Cloots, Peter J Uggowitzer, and Konrad Wegener. Investigations on the microstructure and crack formation of in738lc samples processed by selective laser melting using gaussian and doughnut profiles. *Materials & Design*, 89:770–784, 2016.

[28] Nesma T Aboulkhair, Nicola M Everitt, Ian Ashcroft, and Chris Tuck. Reducing porosity in alsi10mg parts processed by selective laser melting. *Additive Manufacturing*, 1:77–86, 2014.

[29] Jamasp Jhabvala, Eric Boillat, Thibaud Antignac, and Rémy Glardon. On the effect of scanning strategies in the selective laser melting process. *Virtual and physical prototyping*, 5(2):99–109, 2010.

[30] Luke N Carter, Xiqian Wang, Noriko Read, Raja Khan, M Aristizabal, Khamis Essa, and Moataz M Attallah. Process optimisation of selective laser melting using energy density model for nickel based superalloys. *Materials Science and Technology*, 32(7):657–661, 2016.

[31] Jean-Pierre Kruth, Mohsen Badrossamay, Evren Yasa, Jan Deckers, Lore Thijs, and Jan Van Humbeeck. Part and material properties in selective laser melting of metals. pages 3–14, 2010.

[32] Özgür Poyraz and Melih Cemal Kuşhan. Residual stress-induced distortions in laser powder bed additive manufacturing of nickel-based superalloys. *Strojniski Vestnik/Journal of Mechanical Engineering*, 65(6), 2019.

[33] Jiri Hajnys, Marek Pagáč, Jakub Měsíček, Jana Petru, and Mariusz Król. Influence of scanning strategy parameters on residual stress in the slm process according to the bridge curvature method for aisi 316l stainless steel. *Materials*, 13(7):1659, 2020.

[34] Massimo Lorusso. Tribological and wear behavior of metal alloys produced by laser powder bed fusion (lpbf).

[35] Jinliang Zhang, Bo Song, Qingsong Wei, Dave Bourell, and Yusheng Shi. A review of selective laser melting of aluminum alloys: Processing, microstructure, property and developing trends. *Journal of Materials Science & Technology*, 35(2):270–284, 2019.

[36] Lai-Chang Zhang and Hooyar Attar. Selective laser melting of titanium alloys and titanium matrix composites for biomedical applications: a review. *Advanced engineering materials*, 18(4):463–475, 2016.

[37] Kamran Saeidi. Stainless steels fabricated by laser melting: Scaled-down structural hierarchies and microstructural heterogeneities. 2016.

[38] Nima Haghdadi, Majid Laleh, Maxwell Moyle, and Sophie Primig. Additive manufacturing of steels: a review of achievements and challenges. *Journal of Materials Science*, pages 1–44, 2020.

[39] Jose Alberto Muñiz-Lerma, Yuan Tian, Xianglong Wang, Raynald Gauvin, and Mathieu Brochu. Microstructure evolution of inconel 738 fabricated by pulsed laser powder bed fusion. *Progress in Additive Manufacturing*, 4(2):97–107, 2019.

[40] SLM solutions. Material datasheet:ni-alloy in939.

[41] BeamIt. Datasheet inconel 939.

[42] Yanjin Lu, Songquan Wu, Yiliang Gan, Tingting Huang, Chuanguang Yang, Lin Junjie, and Jinxin Lin. Study on the microstructure, mechanical property and residual stress of slm inconel-718 alloy manufactured by differing island scanning strategy. *Optics & Laser Technology*, 75:197–206, 2015.

[43] Shelby Rogers. Siemens turbine blades.

[44] Matthew J Donachie and Stephen J Donachie. Superalloys: a technical guide. 2002.

[45] prof.ssa Biamino Sara. I materiali metallici per i propulsori aeronautici e spaziali:le superleghe base nichel e cobalto e le problematiche relative agli organi di movimento nelle turbine. 2018.

[46] A Lisiecki and A Klimpel. Diode laser surface modification of ti6al4v alloy to improve erosion wear resistance. *Archives of Materials Science and Engineering*, 32(1):5–12, 2008.

[47] Dileep Kumar Ganji and G Rajyalakshmi. Influence of alloying compositions on the properties of nickel-based superalloys: A review. pages 537–555, 2020.

[48] John C Lippold, Samuel D Kiser, and John N DuPont. Welding metallurgy and weldability of nickel-base alloys. 2011.

[49] Tresa M Pollock and Sammy Tin. Nickel-based superalloys for advanced turbine engines: chemistry, microstructure and properties. *Journal of propulsion and power*, 22(2):361–374, 2006.

[50] Åsa Martinsson. Ageing influence on nickel-based superalloys at intermediate temperatures (400-600 c). 2006.

[51] Zhirong Liao, Dragos Axinte, Maxime Mieszala, Rachid M'Saoubi, Johann Michler, and Mark Hardy. On the influence of gamma prime upon machining of advanced nickel based superalloy. *CIRP Annals*, 67(1):109–112, 2018.

[52] Abdul Shaafi Shaikh. Development of γ'precipitation hardening ni-base superalloy for additive manufacturing. 2018.

[53] MR Jahangiri and M Abedini. Effect of long time service exposure on microstructure and mechanical properties of gas turbine vanes made of in939 alloy. *Materials & Design*, 64:588–600, 2014.

[54] Göran Sjöberg, Dzevad Imamovic, Johannes Gabel, Oscar Caballero, Jeffery W Brooks, Jean-Pierre Ferté, and Ariane Lugan. Evaluation of the in 939 alloy for large aircraft engine structures. *Superalloys [Internet]*, pages 441–50, 2004.

[55] P Kanagarajah, F Brenne, T Niendorf, and HJ Maier. Inconel 939 processed by selective laser melting: Effect of microstructure and temperature on the mechanical properties under static and cyclic loading. *Materials Science and Engineering: A*, 588:188–195, 2013.

[56] Giulio Marchese, Simone Parizia, Abdollah Saboori, Diego Manfredi, Mariangela Lombardi, Paolo Fino, Daniele Ugues, and Sara Biamino. The influence of the process parameters on the densification and microstructure development of laser powder bed fused inconel 939. *Metals*, 10(7):882, 2020.

[57] Fan Zhang, Lyle E Levine, Andrew J Allen, Mark R Stoudt, Greta Lindwall, Eric A Lass, Maureen E Williams, Yaakov Idell, and Carelyn E Campbell. Effect of heat treatment on the microstructural evolution of a nickel-based superalloy additive-manufactured by laser powder bed fusion. *Acta materialia*, 152:200–214, 2018.

[58] M Shiomi, K Osakada, K Nakamura, T Yamashita, and F Abe. Residual stress within metallic model made by selective laser melting process. *CIRP Annals*, 53(1):195–198, 2004.

[59] Trattamenti termici leghe di nichel.

[60] Thomas Vilaro, Christophe Colin, Jean-Dominique Bartout, Loic Nazé, and Mohamed Sennour. Microstructural and mechanical approaches of the selective laser melting process applied to a nickel-base superalloy. *Materials Science and Engineering: A*, 534:446–451, 2012.

[61] Xiaomeng Wang, Yu Zhou, Zihua Zhao, and Zheng Zhang. Effects of solutioning on the dissolution and coarsening of γ' precipitates in a nickel-based superalloy. *Journal of Materials Engineering and Performance*, 24(4):1492–1504, 2015.

[62] Solubilizzazione e invecchiamento: Leghe di nichel.

[63] Mahboobeh Azadi, Armin Marbout, Sama Safarloo, Mohammad Azadi, Mehdi Shariat, and Mohammad Hassan Rizi. Effects of solutioning and ageing treatments on properties of inconel-713c nickel-based superalloy under creep loading. *Materials Science and Engineering: A*, 711:195–204, 2018.

[64] HV Atkinson and S Davies. Fundamental aspects of hot isostatic pressing: an overview. *Metallurgical and Materials Transactions A*, 31(12):2981–3000, 2000.

[65] Ahmad Mostafa, Ignacio Picazo Rubio, Vladimir Brailovski, Mohammad Jahazi, and Mamoun Medraj. Structure, texture and phases in 3d printed in718 alloy subjected to homogenization and hip treatments. *Metals*, 7(6):196, 2017.

[66] Wolfgang Tillmann, Christopher Schaak, Jens Nellesen, Mirko Schaper, ME Aydinöz, and K-P Hoyer. Hot isostatic pressing of in718 components manufactured by selective laser melting. *Additive Manufacturing*, 13:93–102, 2017.

[67] Alena Kreitcberg, Vladimir Brailovski, Sylvain Turenne, Cyrille Chanal, and Victor Urlea. Influence of thermo-and hip treatments on the microstructure and mechanical properties of in625 alloy parts produced by selective laser melting: a comparative study. 879:1008–1013, 2017.

[68] MT Kim, DS Kim, and OY Oh. Effect of γ' precipitation during hot isostatic pressing on the mechanical property of a nickel-based superalloy. *Materials Science and Engineering: A*, 480(1-2):218–225, 2008.

[69] Keng-Tu Hsu, Huei-Sen Wang, Hou-Guang Chen, and Po-Chun Chen. Effects of the hot isostatic pressing process on crack healing of the laser repair-welded cm247lc superalloy. *Metals*, 6(10):238, 2016.

[70] Huei-Sen Wang, Yen-Ling Kuo, Chen-Ming Kuo, and Chao-Nan Wei. Microstructural evolution and mechanical properties of hot isostatic pressure bonded cm 247lc superalloy cast. *Materials & Design*, 91:104–110, 2016.

[71] Shih-Hsien Chang. In situ tem observation of γ', γ' and δ precipitations on inconel 718 superalloy through hip treatment. *Journal of alloys and compounds*, 486(1-2):716–721, 2009.

[72] G Appa Rao, Mahendra Kumar, M Srinivas, and DS Sarma. Effect of standard heat treatment on the microstructure and mechanical properties of hot isostatically pressed superalloy inconel 718. *Materials Science and Engineering: A*, 355(1-2):114–125, 2003.

[73] TB Gibbons and R Stickler. In939: Metallurgy, properties and performance. pages 369–393, 1982.

[74] KM Delargy, SWK Shaw, and GDW Smith. Effects of heat treatment on mechanical properties of high-chromium nickel-base superalloy in 939. *Materials science and technology*, 2(10):1031–1037, 1986.

[75] Prima print sharp 250.

[76] Dr. G. Visco Dr.sa M.P. Sammartino, Dr. G. Favero. La produzione di sezioni metallografiche. *Universita' Degli Studi Di Roma "La Sapienza"*, 2003.

[77] Macchina lucidatrice per metalli mecatech 234.

[78] Inverted research microscope for materials testing leica dmi5000 m.

[79] University of Wyoming Susan Swapp. Scanning electron microscopy (sem).

[80] Imagej.

[81] Imade Koutiri, Etienne Pessard, Patrice Peyre, Ouafae Amlou, and Thibaut De Terris. Influence of slm process parameters on the surface finish, porosity rate and fatigue behavior of as-built inconel 625 parts. *Journal of Materials Processing Technology*, 255:536–546, 2018.

[82] Principio di archimede.

[83] Esteban Broitman. Indentation hardness measurements at macro-, micro-, and nanoscale: a critical overview. *Tribology Letters*, 65(1):23, 2017.

[84] Brinell test procedure.

[85] Malven Panalytical. The use of xrd for additive manufacturing of metals.

[86] K Moussaoui, Walter Rubio, Michel Mousseigne, T Sultan, and F Rezai. Effects of selective laser melting additive manufacturing parameters of inconel 718 on porosity, microstructure and mechanical properties. *Materials Science and Engineering: A*, 735:182–190, 2018.

[87] Zhichao Dong, Yabo Liu, Weibin Wen, Jingran Ge, and Jun Liang. Effect of hatch spacing on melt pool and as-built quality during selective laser melting of stainless steel: Modeling and experimental approaches. *Materials*, 12(1):50, 2019.

[88] Mathieu Terner, Jiwon Lee, Giulio Marchese, Sara Biamino, and Hyun-Uk Hong. Electron backscattered diffraction to estimate residual stress levels of a superalloy produced by laser powder bed fusion and subsequent heat treatments. *Materials*, 13(20):4643, 2020.

[89] H. K. D. H. Bhadeshia. Dendritic solidification.

[90] S-C HUANG and ME Glicksman. Fundamentals of dendritic solidification—i. steady-state tip growth. pages 247–261, 1988.

[91] Erica Liverani, Adrian HA Lutey, Alessandro Ascari, and Alessandro Fortunato. The effects of hot isostatic pressing (hip) and solubilization heat treatment on the density, mechanical properties, and microstructure of austenitic stainless steel parts produced by selective laser melting (slm). *The International Journal of Advanced Manufacturing Technology*, 107(1):109–122, 2020.